



Universidade do Minho
Escola de Engenharia

Vânia Catarina da Silva Costa

Preclinical testing of theranostic graphene-based magnetic nanocarriers in 2D and 3D hepatocellular carcinoma models





Universidade do Minho
Escola de Engenharia

Vânia Catarina da Silva Costa

Preclinical testing of theranostic graphene-based magnetic nanocarriers in 2D and 3D hepatocellular carcinoma models

Master Thesis

Master in Biomedical Engineering

Biomaterials, Rehabilitation e Biomechanics Branch

Work developed under the supervision of

Professor Rui Alberto M. M. Lima

and

Doctor Manuel Bañobre-López

January 2021

DIREITOS DE AUTOR E CONDIÇÕES DE UTILIZAÇÃO DO TRABALHO POR TERCEIROS

Este é um trabalho académico que pode ser utilizado por terceiros desde que respeitadas as regras e boas práticas internacionalmente aceites, no que concerne aos direitos de autor e direitos conexos.

Assim, o presente trabalho pode ser utilizado nos termos previstos na licença abaixo indicada. Caso o utilizador necessite de permissão para poder fazer um uso do trabalho em condições não previstas no licenciamento indicado, deverá contactar o autor, através do RepositóriUM da Universidade do Minho.



Atribuição CC BY

<https://creativecommons.org/licenses/by/4.0/>

This work results partially of the project NORTE-01-0145-FEDER-029394, RTChip4Theranostics, supported by Programa Operacional Regional do Norte - Norte Portugal Regional Operational Programme (NORTE 2020), under the PORTUGAL 2020 Partnership Agreement, through the European Regional Development Fund (ERDF) and by Fundação para a Ciência e Tecnologia (FCT), IP, project reference PTDC/EMD-EMD/29394/2017.

NORTE-01-0145-FEDER-029394



PTDC/EMD-EMD/29394/2017



ACKNOWLEDGMENTS

The conclusion of this dissertation was only possible with the support of several people and for this reason I want to express my gratitude for the unconditional support of everyone involved.

First of all, to Professor Graça Minas, for granting me the privilege of developing this dissertation since she was the point of contact with the people involved in the project.

To my advisors, Professor Rui Lima for agreeing to guide this dissertation and for his constant availability and guidance along the journey that led me to finish this dissertation.

To Dr. Manuel Bañobre-López, I am extremely grateful for the opportunity to develop my dissertation at INL, particularly in its research team, AmTheNa group, and for all the constant support, guidance, availability, constructive suggestions throughout the whole process. It was a huge privilege to have worked with him and to be part of his group, where I was able to enhance my skills.

To Victor Gonçalves, for all the monitoring, guidance, support and constant availability to clarify any doubt. Thank you for all the teaching throughout this year. To Dr. Raquel Rodrigues, for the presentation and explanation of the project and for all the availability and monitoring on the first laboratory assays.

To my family, specially to my parents and my brother, without them none of my academic accomplishments would be possible. For all the unconditional support throughout my life, for always being so comprehensive and for the daily encouragement. I'd like to express my gratitude to my boyfriend, Pedro, for always being with me, calming and supporting me, unconditionally, for all the help and patience. A special word of thanks to my closest friends for all the support, motivation, friendship and for always being with me since the beginning of my university journey.

Last but not least, I would like to express my sincere acknowledgment to everyone involved throughout the whole process, including UMinho and INL colleagues that accepted me and made all this journey possible.

STATEMENT OF INTEGRITY

I hereby declare having conducted this academic work with integrity. I confirm that I have not used plagiarism or any form of undue use of information or falsification of results along the process leading to its elaboration.

I further declare that I have fully acknowledged the Code of Ethical Conduct of the University of Minho.

RESUMO

Apesar da evolução clínica no tratamento do cancro, os métodos convencionais não são suficientes para superar as barreiras impostas pela doença. A elevada taxa de incidência e mortalidade é um indicador evidente da urgência clínica para o desenvolvimento de novas estratégias eficientes. Uma potencial solução incide nas nanopartículas magnéticas multifuncionais com revestimentos biocompatíveis e maior capacidade de encapsular fármacos e os libertar no microambiente tumoral ácido, sem danificar os tecidos saudáveis.

Neste trabalho foram usadas nanopartículas magnéticas à base de grafeno revestidas com um polímero (GbMNP@PF127) devido à sua excelente combinação de nanopartículas de óxido de ferro de elevado desempenho magnético (magnetite) e as propriedades únicas de nanocamadas à base de grafeno, como alta estabilidade química e térmica, transporte de elevada carga, biocompatibilidade e elevada área de superfície. Este nanotransportador magnético pode ser usado em aplicações teranósticas, combinando funções de diagnóstico e terapia, como o aumento do contraste de imagem por ressonância magnética (MRI), hipertermia magnética (MH) e entrega controlada de fármaco induzida por pH. Para a validação pré-clínica, o trabalho desenvolvido envolveu: (1) caracterização físico-química das GbMNPs (tamanho, forma, composição química, carga superficial); (2) carga e libertação de fármaco com aplicação de um campo magnético alternado - MH; (3) validação funcional das propriedades teranósticas em linhas celulares tumorais (HepG2): efeito quimioterapêutico combinado com MH e aumento de contraste de MRI; (4) desenvolvimento de organoides hepáticos 3D; e (5) validação funcional do desempenho teranóstico no organoide hepático.

Em suma, os resultados mostram o efeito termoquimioterapêutico das GbMNP@PF127 carregados com doxorrubicina sob MH e a capacidade em aumentar o contraste T_2 -MRI in vitro, confirmando essas nanopartículas como nanosistemas promissores para teranósticos de cancro hepático. Além disso, um modelo organoide 3D de cancro hepático capaz de imitar melhor a complexidade de um tumor sólido foi desenvolvido para validação teranóstica e integração adicional em plataformas de *organ-on-a-chip*.

Palavras-chave: Grafeno, Hipertermia magnética, Imagem por ressonância magnética, Nanopartículas magnéticas, Teranóstico.

ABSTRACT

Despite clinical developments in cancer treatments, conventional methods are not enough to overcome the barriers imposed by the disease. The high rate of incidence and mortality is an evident indicator of a clinical urgency to develop new and efficient strategies. A potential solution lies in multifunctional magnetic nanoparticles with biocompatible surface coatings and enhanced drug loading capacity for drug release triggered by the acidic tumor microenvironment, without damaging the healthy tissues.

In this work, previously developed graphene-based magnetic nanoparticles coated with a polymeric shell (GbMNP@PF127) were used due to their excellent combination of high-magnetic performance, due to the iron oxide (magnetite) cores, and the unique properties of graphene-based nanolayers, such as high chemical and thermal stability, high charge carrier mobility, enhanced biocompatibility and large surface area. This multifunctional magnetic nanocarrier has the ability to be applied in theranostic applications, combining diagnosis and therapy functionalities, such as magnetic resonance imaging (MRI) contrast enhancement, magnetic hyperthermia (MH) and pH induced-controlled drug delivery. In order to preclinically validate its theranostic functionality *in vitro*, the developed involved: (1) physicochemical characterization of GbMNPs (size, shape, chemical composition, surface charge); (2) loading and delivery of a chemotherapeutic drug under the application of an alternating magnetic field - magnetic hyperthermia; (3) functional validation of their theranostic properties in standard tumor cell lines (HepG2), namely combined chemotherapeutic effect through magnetic hyperthermia and MRI contrast enhancement; (4) development of a 3D liver organoid; and (5) functional validation of the theranostic properties in the developed liver-tumor organoid.

Overall, results showed the thermochemotherapeutic effect of doxorubicin-loaded GbMNPs@PF127 under MH in combination with T₂-MRI contrast enhancement capability *in vitro*, confirming these nanoparticles as promising nanosystems for liver cancer theranostics. Furthermore, a functional liver organoid able to better mimic the complexity of a solid tumor was developed for theranostic validation and further integration in organ-on-a-chip platforms.

Keywords: Graphene, Magnetic hyperthermia, Magnetic nanoparticles, Magnetic resonance imaging, Theranostic.

CONTENTS

ACKNOWLEDGMENTS.....	iv
STATEMENT OF INTEGRITY.....	v
RESUMO.....	vi
ABSTRACT.....	vii
LIST OF FIGURES.....	xi
LIST OF TABLES.....	xiv
LIST OF ABBREVIATIONS AND ACRONYMS.....	xv
1. INTRODUCTION.....	1
1.1 MOTIVATION.....	1
1.2 GOALS.....	4
1.3 ORGANIZATION OF THE DISSERTATION STRUCTURE.....	5
2. FUNDAMENTALS.....	7
2.1. LIVER CANCER.....	7
2.2. DOXORUBICIN.....	10
2.3. NANOTECHNOLOGY AND NANOPARTICLES.....	14
2.3.1. Organic and inorganic nanoparticles.....	17
2.3.2. Carbon nanostructures.....	18
2.4. MAGNETISM.....	20
2.5. MAGNETIC NANOPARTICLES (MNPs).....	26
2.5.1. Composition.....	27
2.5.2. Synthesis methodologies.....	29
2.5.3. Surface modification strategies.....	32
2.6. GRAPHENE-BASED MAGNETIC NANOPARTICLES (GbMNPs).....	32
2.6.1. Biomedical applications of GbMNPs.....	33
2.6.1.1. Magnetic Resonance Imaging (MRI) contrast agents.....	34
2.6.1.2. Drug delivery.....	35
2.6.1.3. Magnetic Hyperthermia.....	36
2.7. 3D <i>IN VITRO</i> MODELS.....	38
2.7.1. Spheroids.....	39
2.7.2. Organoids.....	42
3. MATERIALS AND METHODS.....	44
3.1. CHEMICALS.....	44
3.2. SYNTHESIS OF GbMNPS.....	44

3.2.1.	Hydrophilization of GbMNPs	45
3.2.2.	Purification procedure	46
3.3.	PHYSICOCHEMICAL CHARACTERIZATION OF GbMNPs	46
3.3.1.	Inductively coupled plasma-optical emission spectroscopy	46
3.3.2.	Dynamic light scattering	48
3.3.2.1.	Hydrodynamic diameter	49
3.3.2.2.	Zeta potential	50
3.3.3.	Magnetic hyperthermia	51
3.3.4.	MRI	53
3.3.5.	High performance liquid chromatography	55
3.3.6.	Drug loading / capacity studies.....	56
3.3.7.	DOX release and kinetics analysis.....	57
3.4.	PREPARATION OF 3D LIVER-TUMOR ORGANIDS.....	61
3.4.1.	Cell cultures	61
3.4.2.	Preparation of HepG2-derived organoids.....	62
3.5.	BIOLOGICAL CHARACTERIZATION.....	64
3.5.1.	Confocal microscopy.....	65
3.5.2.	Cellular function of liver-tumor organoids	66
3.5.3.	Cytotoxicity and anticancer effect assessment.....	69
3.5.3.1.	AquaBluer	70
3.5.3.2.	Live/Dead.....	71
3.5.3.3.	Lactate dehydrogenase (LDH).....	71
3.5.4.	<i>In vitro</i> functional validation.....	73
3.5.4.1.	Thermochemotherapy.....	74
3.5.4.2.	MRI	75
4.	RESULTS AND DISCUSSION	77
4.1.	PHYSICOCHEMICAL CHARACTERIZATION OF GbMNPs	77
4.1.1.	Fe concentration	77
4.1.2.	Hydrodynamic particle size.....	78
4.1.3.	Zeta potential	78
4.1.4.	DOX loading efficiency / capacity:	79
4.1.5.	DOX release	80
4.2.	<i>IN VITRO</i> PRECLINICAL VALIDATION	82
4.2.1.	2D models: HepG2 cells.....	82
4.2.1.1.	Biocompatibility studies	82
4.2.1.2.	Cytotoxicity and anticancer effect	83

4.2.1.3.	MRI studies	85
4.2.2.	3D models: liver-tumor organoids.....	88
4.2.2.1.	Preparation of HepG2-derived organoids.....	88
4.2.2.2.	Cell viability	88
4.2.2.3.	Cellular function	90
4.2.2.4.	Cytotoxicity and anticancer effect	91
5.	CONCLUSION AND FUTURE WORK	94
6.	BIBLIOGRAPHY.....	97
	ANNEX 1 - PHYSICOCHEMICAL CHARACTERIZATION OF GbMNPs	109

LIST OF FIGURES

Figure 1: Incidence of the most common cancers and incidence of cancers that cause the highest number of deaths worldwide in 2018 [2].	1
Figure 2: Illustration of hepatic tumor microenvironment and primary tumor to be metastasized to other sites in the body (secondary cancer). Adapted and edited from [6].	8
Figure 3: Chemical structure of doxorubicin [31].	11
Figure 4: DOX intercalation into DNA. A) TOP2 relaxes DNA supercoil to facilitate replication and DNA synthesis; B) DOX forms a complex by DNA through G bases in both of DNA strands and prevents TOP2 activity and DNA synthesis. TOP2: Topoisomerase II, G: guanine, C: cytosine [34].	13
Figure 5: Length scale that compares the size of various biological components and some more familiar materials and objects [55].	14
Figure 6: Different nanocarriers for liver cancer targeted drug delivery applications [61].	16
Figure 7: Schematic chemical structures of graphene-based nanostructures: (A) graphene; (B) GO and; (C) rGO [74].	19
Figure 8: Schematic representation of magnetic moments. (A) Spin magnetic moment; (B) Orbital magnetic moment. Drawn in Biorender.	21
Figure 9: Types of magnetism under an externally applied magnetic field. (a) Paramagnetism; (b) Ferromagnetism; (c) Diamagnetism; (d) Antiferromagnetism; (e) Ferrimagnetism [77].	22
Figure 10: Schematic illustration of typical hysteresis loops of: (a) ferromagnetic; (b) superparamagnetic materials. Drawn in Biorender inspired by refs. [77,83,86].	24
Figure 11: Heat generation mechanisms in superparamagnetic nanoparticles in response to an AMF. The short straight arrows represent the magnetic moment direction, the curved arrows represent the movement or change in direction. Based in [88].	25
Figure 12: Crystal structure of (A) hematite ($\alpha\text{-Fe}_2\text{O}_3$); (B) magnetite (Fe_3O_4); (C) maghemite ($\gamma\text{-Fe}_2\text{O}_3$) [96].	29
Figure 13: Schematic overview of the physiological similarities between in vivo solid tumors and in vitro tumor spheroids [142].	42
Figure 14: Comparison between organoids and standard 2D and 3D in vitro models [146].	43
Figure 15: Schematic representation of the GbMNPs synthesis route.	45
Figure 16: (A) Diagram of a typical ICP-OES instrument with radial configuration of the detection system [150] and (B) picture of the ICPE-9000 Multitype ICP Emission Spectrometer used in this work.	47
Figure 17: Optical configuration of a typical experimental setup for dynamic light scattering measurement [154].	48

Figure 18: Picture of the Nano Particle Analyzer Z-100 equipment used to measure the hydrodynamic diameter and zeta potential of the samples.....	49
Figure 19: Scheme of the electrical double layer that surrounds a particle in an aqueous medium. The zeta potential is the electrical potential at the slipping plane [164].	51
Figure 20: Schematic representation of a MH setup. (A) Inside the coil a magnetic nanoparticle is represented drawn in SolidWorks software; (B) commercial alternating current field applicator from nanoTherics, NAN201003 Magnetherm; and (C) NAN201007 Live Cell Exposure accessory from nanoTherics.....	53
Figure 21: (A) Schematic representation of a MRI scanner (Adapted from [168]) and (B) a 3T-MRI Solutions Benchtop Scanner (Guildford, UK) used in this work.	54
Figure 22: (A) HPLC system configuration [173]; (B) Picture of the UHPLC Agilent 1290 Infinity II LC System used in this work.	56
Figure 23: Picture of the drug release multi-point set up.	58
Figure 24: Optical microscope image of the HepG2 cells in culture.	62
Figure 25: (A) Image of a polydimethylsiloxane (PDMS) multi-microwells mold (1,156 wells); (B) a magnification of the same mold where the well size is better appreciated (300 μm).	63
Figure 26: Optical image of growth spheroids in a PDMS mold.	63
Figure 27: Image of the photo-polymerized GelMA containing the developed HepG2 spheroids in a multi-well plate.	64
Figure 28: (A) Simplified scheme of a confocal microscope and (B) image of the confocal microscope LSM780 used in this work.	66
Figure 29: (A) dilution series for albumin assay; (B) dilution series for transferrin assay.....	69
Figure 30: Schema of the CyQuant LDH cytotoxicity assay mechanism. Adapted from [192]......	72
Figure 31: Schematic procedure of the in vitro experiment with HepG2 cells using petri dishes divided into four different groups.....	74
Figure 32: Picture of a petri dish containing one organoid in each compartment.	75
Figure 33: DOX release at different pHs (5, 6.5, 7.4) with and without magnetic hyperthermia. An AMF of 20 mT and 285.4 KHz was applied for 4 h. Values represent mean \pm SEM.....	80
Figure 34: Metabolic viability of HepG2 cells when incubated with GbMNP@PF127 at different time points (24, 48 and 72h) and different iron concentrations (0, 1, 5, 10, 20, 30, 50 and 100 $\mu\text{g Fe mL}^{-1}$). Values represent mean \pm SEM. Statistically significant differences were determined using Two-way ANOVA with Bonferroni test. Significant difference is relation to NT. ****P \leq 0.0001.	83
Figure 35: Percentage of viable HepG2 cells at 48h for different groups (NT- no treatment, NPs – GbMNP@PF127 nanoparticles, NPs@DOX – GbMNP@PF127 nanoparticles with encapsulated DOX and DOX- free doxorubicin) with and without hyperthermia induction. NT represents 100% of cell	

viability under no magnetic hyperthermia treatment. Values represent mean \pm SEM. Statistically significant differences were determined using Two-way ANOVA with Bonferroni test. Significant difference is relation to NT without hyperthermia. * $P \leq 0.05$; *** $P \leq 0.001$; **** $P \leq 0.0001$84

Figure 36: (A) Linear fitting of the relaxation rates at 3T for GbMNP@PF127. The slope indicates the transverse relaxivity r_2 and (B) T_2 -MRI map for GbMNP@PF127 dispersions at different Fe concentrations at a magnetic field of 3T.86

Figure 37: (A) Relaxation rates at 3T as a function of the Fe concentration of the GbMNP@PF127 dispersions used in the incubation with cells and (B) T_2 -MRI map of GbMNP@PF127-labeled HepG2 cells. $[Fe]_{in} = [Fe]_{incubation}$87

Figure 38: (A) image of the organoid-like gel structure removed from the wells; (B),(C) Light-microscopic images of HepG2 organoids embedded in the GelMA hydrogel.88

Figure 39: Confocal microscopy images of an HepG2 Organoid after a) 24h and b) 72h of his formation. The live cells were stained with green fluorescent dye (live cells) and red fluorescent dye (dead cells).89

Figure 40: Cell viability in HepG2 organoids after 1, 2, 3, 7, 10, and 14 days by LDH assay. Values represent mean \pm SEM. Statistically significant differences were determined using One-way ANOVA with Bonferroni test. Significant difference is relation to 1 day of culture. * $P \leq 0.05$; **** $P \leq 0.0001$90

Figure 41: Quantification of secreted transferrin (A) and albumin (B) for 2D culture and organoids by ELISA at 24, 48 and 72h of incubation. Values represent mean \pm SEM. Statistically significant differences were determined using Two-way ANOVA with Bonferroni test. **** $P \leq 0.0001$91

Figure 42: Percentage of viable HepG2 organoids at 48h for different groups (NT- no treatment, NPs – GbMNP@PF127 nanoparticles, NPs@DOX – GbMNP@PF127 nanoparticles with encapsulated DOX and DOX- free doxorubicin) with and without hyperthermia induction. NT represents 100% of cell viability under no magnetic hyperthermia treatment. Values represent mean \pm SEM. Statistically significant differences were determined using Two-way ANOVA with Bonferroni test. Significant difference is relation to NT without hyperthermia.; ns: not significant; **** $P \leq 0.0001$92

LIST OF TABLES

Table 1: Major classes of chemotherapeutic agents for liver cancer treatment [20].	10
Table 2: Physicochemical properties of DOX.	11
Table 3: Physical and chemical properties of magnetite, maghemite, and hematite [77,87].	28
Table 4: Summary comparison of the synthetic methods [77,96].	31
Table 5: Comparison of 2D monolayer and 3D spheroid cultures regarding its performance to mimic the TME.	39
Table 6: Interpretation of release mechanisms from cylinder polymeric matrices [120,175,178].	60
Table 7: Summary of mathematical models used to describe drug release profiles.	61
Table 8: Materials supplied from human albumin ELISA kit.	67
Table 9: Materials supplied from human transferrin ELISA kit.	68
Table 10: Contents and storage from LDH cytotoxicity assay kit.	72
Table 11: Parameter of acquisition of T ₂ maps.	76
Table 12: Fe concentration in GbMNP@PF127 dispersions determine by ICP-OES.	77
Table 13: Colloidal and dimensional properties of GbMNP@PF127: hydrodynamic diameter, polydispersion and zeta potential.	78
Table 14: Drug release kinetic analysis of GbMNP@PF127@DOX at different pHs. The * symbol refers to the samples that were subjected to an AMF.	81

LIST OF ABBREVIATIONS AND ACRONYMS

T	Absolute temperature
AIC	Akaike information criterion
Q_t	Amount of drug dissolved
W_{GbmNPs}	Amount of nanoparticles in solution
K_A	Anisotropy constant
AMF	Alternating magnetic field
k_B	Boltzmann constant
BSA	Bovine serum albumin
τ_B	Brownian relaxation time
CO ₂	Carbon dioxide
H _c	Coercivity
K_{HC}	Constant of the surface-volume relation
CA	Contrast agents
T _c	Curie temperature
DNA	Deoxyribonucleic acid
ε	Dielectric permittivity
D	Diffusion coefficient
DOX	Doxorubicin
$W_{initial}$	DOX initial
W_{loaded}	DOX loaded into the nanoparticles
DLC	Drug loading capacity
DLE	Drug loading efficiency
DLS	Dynamic light scattering
H	Dynamic viscosity
T _E	Echo time
U _e	Electrophoretic mobility
ELISA	Enzyme-linked immunosorbent assay
K_1	First-order rate constant
$W_{free\ dox}$	free DOX
f	Frequency
C	Heat capacity
$f(ka)$	Henry's function
HPLC	High performance liquid chromatography
K_H	Higuchi dissolution constant
HepG2	Human liver hepatocellular carcinoma cell line
d _H	Hydrodynamic diameter
V _H	Hydrodynamic volume
ECM	Extracellular matrix

FSE	Fast spin echo
FBS	Fetal bovine serum
FOV	Field of view
FDA	Food and drug administration
Gd ³⁺	Gadolinium
GbMNPs	Graphene-based magnetic nanoparticles
GbMNP@PF127	GbMNPs functionalized with PF127
GO	Graphene oxide
Q_0	Initial amount of drug in the solution
INL	International Iberian nanotechnology laboratory
ICC	Intrahepatic cholangiocarcinoma
α -Fe ₂ O ₃	Hematite
HBV	Hepatitis B virus
HCV	Hepatitis C virus
HTME	Hepatic tumor microenvironment
ICP-OES	Inductively coupled plasma optical emission spectrometry
LDH	Lactate dehydrogenase
T ₁	Longitudinal relaxation
r ₁	Longitudinal relaxivity
γ -Fe ₂ O ₃	Maghemite
H	Magnetic field strength
MH	Magnetic hyperthermia
B	Magnetic induction
MIONs	Magnetic Iron Oxide Nanoparticles
M	Magnetic moment per volume
MNPs	Magnetic Nanoparticles
MRI	Magnetic resonance imaging
Fe ₃ O ₄	Magnetite
m _{MNP}	Mass of magnetic material
MSCs	Mesenchymal stem cells
mRNA	Messenger RNA
MEMS	Multi-echo-multi-slice
NPs	Nanoparticles
NPs@DOX	Nanoparticles with encapsulated DOX
τ_N	Néel relaxation time
NT	No treatment
Ns	Not significant
NMR	Nuclear magnetic resonance
NA	Number of averages
N	Number of experimental data points
P	Number of parameters

μ_0	Permeability in vacuum
PBS	Phosphate Buffer Solution
PF127	Pluronic F127
PDMS	polydimethylsiloxane
PEO	Poly (ethylene oxide)
PPO	Poly (propylene oxide)
PI	Propidium iodide
rGO	Reduced Graphene oxide
n	Release exponent
K_m	release rate constant
Mr	Remanence magnetization
T_R	Repetition time
RNA	Ribonucleic acid
RT	Room temperature
RPMI	Roswell Park Memorial Institute
Ms	Saturation magnetization
SEM	Scanning electron microscopy
SSR	Sum of the square residuals
SAR	Specific absorption rate
SPIONs	Superparamagnetic Iron Oxide Nanoparticles
INT	Tetrazolium salt
T	Time
τ_0	Time constant
TOP2	Topoisomerase II
AT	Total acquisition time
r_2	Transversal relaxivity
T_2	Transverse relaxation
TME	Tumor Microenvironment
2D	Two dimensional
3D	Three dimensional
V	Volume
K_0	Zero-order release constant
Z	Zeta-potential

1. INTRODUCTION

1.1 MOTIVATION

Cancer is currently one of the most approached and studied diseases since it is one of the main threats to human health globally. Cancer is the second leading cause of death worldwide and in 2018 it was estimated that 9.6 million deaths were caused by cancer. In particular, liver cancer showed an incidence of 841.080 cases with a mortality of 781.631 deaths in 2018 (Figure 1) [1,2].

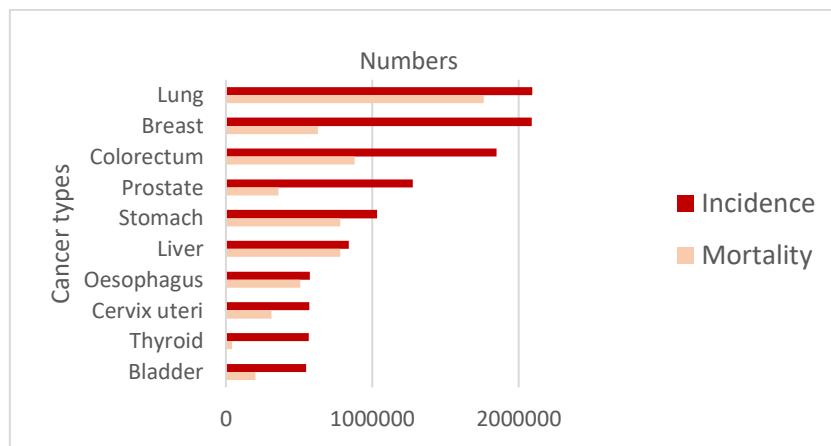


Figure 1: Incidence of the most common cancers and incidence of cancers that cause the highest number of deaths worldwide in 2018 [2].

Conventional approaches currently established to cancer treatment include chemotherapy, radiotherapy and resection surgery, where chemotherapy is the most used method. These clinical approaches allow some progress in the fight against the disease. However, in some cases, these therapies may be ineffective and not enough to fight the versatility of different tumors, since the percentage of deaths from this disease has been increasing every year [3,4].

Despite clinical developments in cancer treatments, conventional methods are not sufficient to overcome the obstacles imposed by the disease. This high rate of incidence and

mortality is an evident indicator of the clinical urgency to develop new and efficient methods of diagnosis, screening, treatment, and palliative care. In addition, the improvement of the existing treatments is also required to achieve great effectiveness in the healing of this disease, reducing the side effects and mortality rate [1,3,5].

Recently, the role of the tumor microenvironment has been the focus of attention to combat this deadly disease, as it has become evident that it acts as a fertile soil to grow the cancerous seeds [6]. The cellular environment influences multiple stages of cancer such as development, growth, metastatic spread, anti-tumor immunity and cancer therapeutic responses [7].

The hepatic tumor microenvironment presents some of the most common particularities of solid tumors in general, including the low oxygen concentrations (hypoxia), drastic changes in cellular metabolism (which lead to the production and accumulation of suppressive metabolites, such as adenosine and lactate), low pH (acidosis), poor nutrient loads, collection of immunosuppressive cytokines and growth factors [8][9].

Despite all efforts to overcome the challenges imposed by cancer, there are many risks associated with the current conventional therapies. Thus, many barriers need to be overcome to ensure the effective treatment without harmful damage, such as:

- (i) High doses of the chemotherapeutic drug are generally required to ensure that it reaches the tumor tissue [10].
- (ii) Lack of cell specificity in the delivery of the drug, which leads to toxicity in healthy tissues, resulting in several side effects [10].
- (iii) Poor tolerance to chemotherapeutic drugs by liver cancer patients due to liver dysfunction, resulting in an urgent need for liver targeting drugs [11].
- (iv) Presence of drug resistance mechanisms that may limit its clinical outcome [12].

In order to achieve the desired results with great efficiency and safety, new methodologies for cancer treatment have been developed, mainly in the nanotechnology field. These novel methodologies have shown great promise in biomedicine, offering unique properties and many opportunities for innovation, namely in the improvement of treatment and diagnosis against cancer and other diseases [13]. As an example, this improvement can

be achieved with magnetic nanoparticles, specifically superparamagnetic nanoparticles. They have small size (<20 nm), high magnetic susceptibility, high saturation magnetization and low toxicity, showing the ability to reduce the relaxation time of water protons' nuclei and also heat up under an alternating magnetic field. Considering this unique characteristics, these multifunctional superparamagnetic nanoparticles have been widely explored for theranostics, where both therapy (i.e. magnetic hyperthermia, drug delivery) and diagnosis (imaging) modalities are integrated in single material platforms [13–15].

Hyperthermia is continuously evolving as an adjuvant in cancer treatment because of its capability to further increase the vulnerability of cancer cells when subjected to the conventional therapies (i.e. radiotherapy and chemotherapy), thus improving the effectiveness of the treatments applied. However, the resulting toxicity between cancer cells and healthy cells remains similar, which makes hyperthermia a cancer treatment that still presents several obstacles to overcome. Consequently, magnetic hyperthermia has emerged as a promising therapy when combined with superparamagnetic nanoparticles. When subjected to an alternating magnetic field (AMF) of suitable amplitude and frequency, superparamagnetic nanoparticles are able to transform the electromagnetic energy into heat which allows to increase the temperature in the localized regions where the nanoparticles are accumulated in the tumor cells. Moreover, superparamagnetic nanoparticles with suitable biocompatible coatings can be used as components in the design of nanocarrier systems to encapsulate and deliver chemotherapeutic drugs to the tumor site. Providing them with suitable functionalities to target specific locations inside the body and offer a controllable drug release, they are able to reduce the amount of administered drug needed to attain a particular concentration on the tumor sites, while protecting healthy tissues and minimizing severe side effects [14,16–18]. Regarding diagnostic applications, magnetic nanoparticles have been extensively studied to be applied as magnetic resonance imaging contrast agents for the non-invasive detection/progression of tumors. Overall, nanotechnology has the potential to greatly impact cancer medicine through the development of nanosystems able to offer a series of diagnosis and therapy functions which, altogether, contribute to minimize the main drawbacks of conventional therapies and allow for a better management of disease [14,19].

This work constitutes a follow up of a previous study where the creation of a new graphene-based magnetic nanocarrier, followed by its physicochemical and functional

characterization were performed. Thus, this study focuses on the functional performance and *in vitro* preclinical validation of previously developed theranostic graphene-based magnetic nanocarriers as magnetic resonance imaging contrast agents, magnetic hyperthermia effectors and controlled drug delivery systems. These new generation of advanced theranostic nanocarriers can be a crucial tool in nanomedicine to improve cancer diagnosis and treatment.

1.2 GOALS

This work is incorporated in a larger project funded by Fundação para a Ciência e Tecnologia (FCT), RTChip4Theranostics, in which the objective is to fabricate a microfluidic-based liver-tumor-organ-on-a-chip for the *in vitro* testing of pH-responsive and theranostic drug-loaded graphene-based magnetic formulations. This advanced *in vitro* model of disease intends to better recapitulate the complex functions of a human liver tumor at the microscale that allows for a faster, cost-efficient and meaningful formulation testing and development.

Previous research to this work has been carried out on the synthesis, characterization and functional validation of graphene-based magnetic nanoparticles. The balance between the different functionalities integrated in these nanoparticulated structure has been also optimized for them to offer multifunctional theranostic properties (pH-induced controlled release, magnetic hyperthermia and MRI contrast enhancement). The next step in the characterization workflow towards future clinical studies involves the *in vitro* preclinical functional validation of the developed multifunctional carriers in both 2D and 3D biological models of disease. Therefore, the main focus of this work was the static *in vitro* preclinical validation of the developed graphene-based magnetic nanocarriers as theranostic agents for liver cancer management, which can be split in three different goals depending of the complexity of the biological models used in the study:

- Functional performance validation in 2D cultured tumor cells;
- Development of an advanced 3D organoid model of liver cancer;
- Functional performance validation in the developed liver-tumor organoid.

Further studies following this work will involve the integration of the liver-tumor organoid developed in this work in a microfluidic platform for the animal-free and dynamic in vitro validation of the developed pharmaceutical formulations.

1.3 ORGANIZATION OF THE DISSERTATION STRUCTURE

The structure of this dissertation is divided into five chapters: Introduction, Fundamentals, Materials and Methods, Results and Discussion, Conclusion and Future work.

In the first chapter, *Introduction*, an overview presenting the health problem is presented, highlighting the need of developing new methodologies to address it. Therefore, a brief contextualization of the topic is presented, followed by the description of our proposed approach and the main goals that this thesis pursues.

In the second chapter, *Fundamentals*, theoretical concepts and existing background closely related to the topic of this thesis are provided in more detail to support the experimental work and help the reader understand the developed methodology and the interpretation of the results obtained. Initially, information about liver cancer and the relevance of the tumor microenvironment, as well as current clinical treatments are given. Then, the chemotherapeutic drug doxorubicin, which is the drug of choice of this experimental work, and its mechanism of action are described. After, the importance of nanotechnology and nanocarriers in cancer management is referred. Magnetism and the different types of magnetism are also presented, as it is a key element in the approach proposed in this work. Next, magnetic nanoparticles are introduced, describing the main principles regarding their composition, synthesis and surface modification strategies. Then, information about graphene-based magnetic nanoparticles and their biomedical applications is particularly provided. Finally, the relevance of advanced biological models such as spheroids and organoids is highlighted as more suitable models for preclinical validation as they better recapitulate the complexity of the human scenario.

In the third chapter, *Materials and Methods*, all the reagents, precursors, materials, equipment and methodologies used during the development of the experimental work are properly described.

The fourth chapter, *Results and Discussion*, presents and discusses all the results derived from the experimental work under the perspective of the envisioned application.

Finally, the last chapter, *Conclusion and Future work*, offers a summary of the main conclusions supported by the results obtained and proposes a series of guidelines and suggestions to move this work a step forward.

2. FUNDAMENTALS

2.1. LIVER CANCER

The liver has multiple functions in the body, among them it synthesizes albumin that is responsible for the transport of fatty acids, various metabolites and metabolization of drugs. The energy storage is another important function of the liver as it stores glucose in the form of glycogen, sent to the blood flow when necessary. The liver is essentially known for carrying out the body's metabolism or detoxification [8,14,20].

Liver cancer is one of the most common cancer worldwide and it can be classified as primary or secondary. Hepatocellular carcinoma is the most common primary liver tumor and the intrahepatic cholangiocarcinoma (ICC) is the second most common [21]. Secondary liver cancer appears when the cancer spreads from somewhere else in the body. The number of cases detected with this disease is similar to the number of deaths that it causes, being the mortality rate approximately 93%, in 2018 [2,22,23]. Liver cancer is strongly associated with chronic viral hepatitis (hepatitis B virus (HBV) and hepatitis C virus (HCV)), HBV and HCV co-infection, alcoholic cirrhosis, metabolic disorders, tobacco and metastases from cancers elsewhere in the body [11,22–26].

When a normal cell turns into a carcinogenic cell it begins to invade and change the surrounding matrix to support the cancer development. This modified environment around malignant cells is termed tumor microenvironment (TME) [6]. The TME has been the focus of attention since it has become evident that its cellular environment influences multiple stages of cancer such as development, growth, metastatic spread, anti-tumor immunity and cancer therapeutic responses [7]. The TME is an important subject since it has the ability to induce differentiation of regulatory immune cells, inhibit immune cell activation and provoke death or halt the proliferation of immune cells [8]. The hepatic tumor microenvironment (HTME) is mainly composed of immune cells (like lymphocytes and myeloid cells), stromal cells (such as endothelial cells, pericytes, and fibroblasts) and the extracellular matrix (ECM), as seen in Figure 2 [8,11].

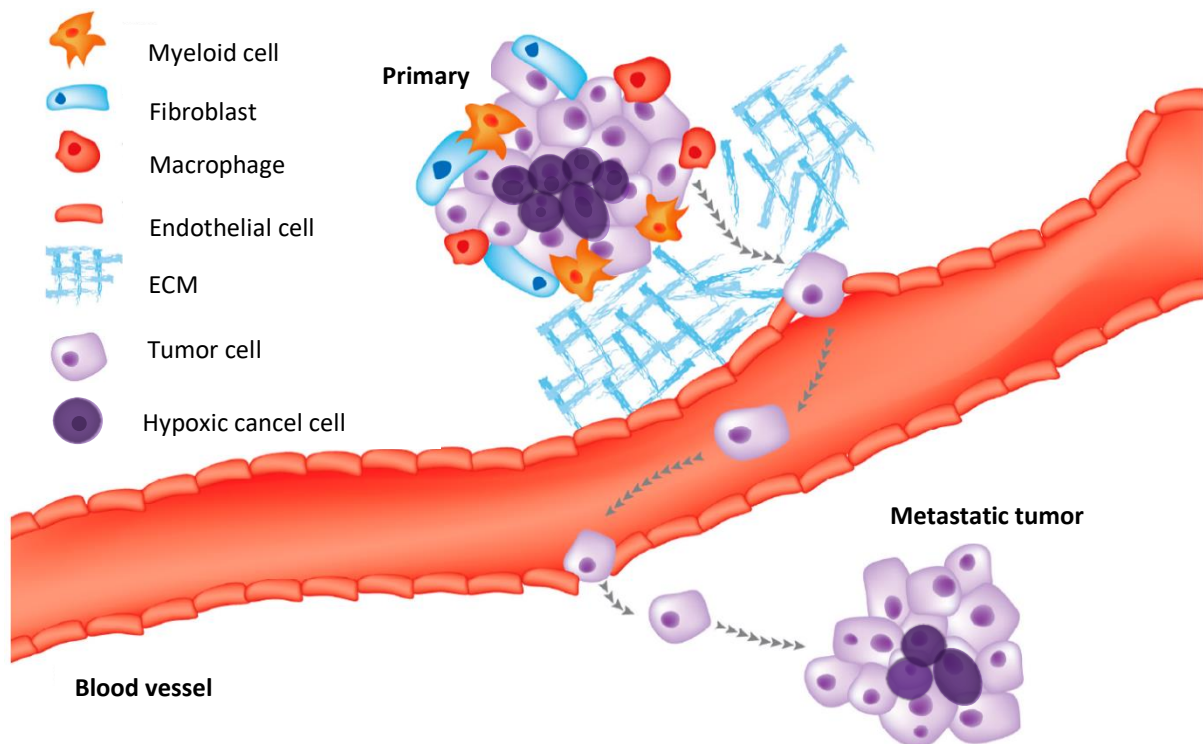


Figure 2: Illustration of hepatic tumor microenvironment and primary tumor to be metastasized to other sites in the body (secondary cancer). Adapted and edited from [6].

Some of the most common features of HTME includes [8,9]:

- (i) Low oxygen concentrations (hypoxia);
- (ii) Drastic changes in cellular metabolism which lead to the production of suppressive metabolites, such as adenosine and lactate;
- (iii) Low pH (acidosis);
- (iv) Poor nutrient loads;
- (v) Collection of immunosuppressive cytokines and growth factors;
- (vi) Accumulated metabolic by-products, such as lactate.

Due to metabolic changes, tumor cells consume and break down large amounts of glucose through aerobic and anaerobic processes. Carbon dioxide (CO_2) and lactate are obtained from the decomposition of glucose, where CO_2 is subsequently converted into bicarbonate and protons, causing an acidification of the microenvironment. Posteriorly, lactate further acidifies the microenvironment when hydrogens are removed by ion transporters. The increase of these metabolites can induce a decrease in the extracellular pH

to 6.6 making more difficult the infiltration of immune cells [8]. Healthy cells have more difficulty adapting to environmental changes than tumor cells, reason why it is possible to sustain growth, invasion and metastasis of cancer cells. The interactions between tumor cells and the associated stroma represent a dangerous relationship that reciprocally influences the disease initiation and progression [27].

In order to combat this disease, there are already a variety of treatments available, such as:

- (i) **Surgically extract** part of the organ that contains the tumor is an effective method to heal patients with liver cancer. However, when cancer is diagnosed, a large proportion of patients are already in advanced stages of the disease, therefore surgical resection is not possible [21,23]. Furthermore, only 10-20% of liver tumors can be removed surgically [11].
- (ii) **Liver transplantation** is the only truly effective treatment for end-stage liver diseases like advanced liver cancer. Nonetheless, it exhibits severe limitations such as the scarce of donors, surgical complications, high costs and needs immunosuppression throughout life [24,28,29].
- (iii) **Hepatocyte transplantation** and **Mesenchymal stem cells (MSCs) transplantation** are less effective solution for the treatment of these diseases. Although hepatocyte transplantation treatment is less invasive and less expensive, there are many negative points, such as the scarcity of primary hepatocyte donors, rejection, weak *in vitro* hepatic functions and only a very small percentage of primary hepatocytes migrate to the host liver tissue. MSCs can be isolated from several tissues, restore liver function after hepatogenic differentiation and have immunomodulatory, anti-inflammatory, antifibrotic, antioxidative stress and antiapoptotic effects on liver cells. Some restrictions are faced in this transplant, such as malignant transformation, cross-contamination, poor engraftment, limited *in vivo* differentiation, the possibility of these cells promoting tumor initiation and growth by performing immunosuppressive and angiogenic effects in hepatocellular carcinoma [24,28].

In addition to these methodologies, conventional therapies such as chemotherapy, are also used. Since the liver is the main organ responsible for drug clearance and for the synthetic function of many biochemical pathways, it is worth noting that many chemotherapy drugs demand suitable liver function to be metabolized, and some drugs can induce significant liver damage. There are several chemotherapeutic agents, as seen in the Table 1, that act and affect the liver in different ways¹ [20].

Table 1: Major classes of chemotherapeutic agents for liver cancer treatment [20].

Class	Mechanism	Examples
Alkylating agents	DNA damage, not phase specific	Platinums (cisplatin, carboplatin, oxaliplatin), nitrogen mustard derivatives (cytoxan, chlorambucil), alkyl sulfonates, nitrosourea (carmustine, lomustine), triazines
Anti-metabolites	DNA/RNA replication in S phase of cell division	Pyrimidine analogues (gemcitabine, 5-fluorouracil, capecitabine), methotrexate, gemcitabine-gemzar, 6 mercaptopurine, cytarabine
Anti-tumor antibiotics	Interfere with enzymes needed for DNA replication	Doxorubicin-adriamycin, danorubicin, mytomycin C, bleomycin
Isomerase inhibitors	Interfere with enzymes needed for DNA replication	Topotecan, irinotecan
Mitotic inhibitors	Plant alkaloids that inhibit mitosis in tumor cells	Taxanes-TAXOL, taxotere, vinca alkaloids (vincristine, vinblastine), etramustine – emcyt

Doxorubicin (DOX) is an example of common anti-tumor antibiotics that injure the cell by interfering with DNA or RNA synthesis [20], as it will be explained in more detail below.

2.2. DOXORUBICIN

Anthracyclines represent an essential class of anti-tumor chemotherapy drugs with great pharmacological interest such as strong antibiotics [30,31]. DOX, also known as Adriamycin, is one of the most used anthracyclines for the treatment of several malignancies

¹ For further information on this subject can be check in Sharma's work [20].

[31–33]. This drug is isolated from cultures of *Streptomyces peucetius* var. *caesius*. [34,35]. DOX consists of a daunomycinone linked through a glycosidic bond to an amino sugar, Daunosamine, as seen in Figure 3, and their main physicochemical properties are represented in Table 2 [36,37].

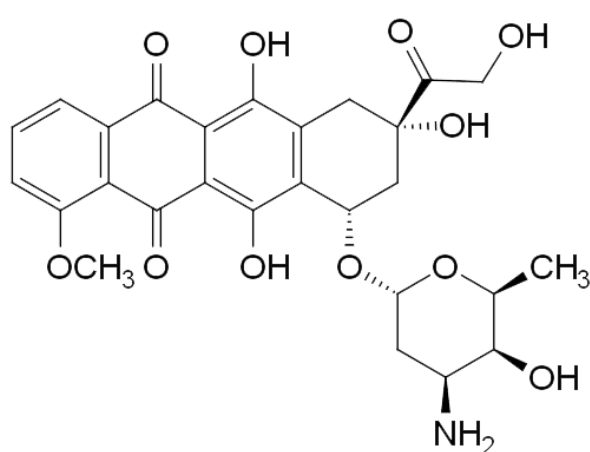


Table 2: Physicochemical properties of DOX.

Properties of Doxorubicin		
Molecular formula	C ₂₇ H ₂₉ NO ₁₁	[38]
Molar mass	543.52 g mol ⁻¹	[38]
Metabolism	Liver	[39]
Soluble	Water, methanol, aqueous alcohol solution	[38]
Not soluble	Non-polar organic solvents	[38]

Figure 3: Chemical structure of doxorubicin [31].

DOX was the drug of choice for this work due to its intrinsic fluorescence, which offers added value for research and imaging purposes, allowing the tracking of the drug in vitro cells. Moreover, DOX was the drug chosen to study the drug delivery capabilities of the nanoparticles used in this work, which has shown a potential to carry high payload cationic drugs due to its physical and chemical properties such as high negative surface charge, optimal size range, large surface area, mesoporous nature and hollow cavity [33,36].

The experiments with DOX started in 1969 and due to the excellent trials results, the drug was approved for clinical usage, despite the amount of detected side effects [31,33,36]. Currently, DOX is employed to treat a wide range of human tumors, like breast, ovarian, thyroid, esophageal, gastric and liver carcinomas. Acute leukemia, osteosarcoma and Wilms tumor are also known diseases where the DOX is used as a treatment [30–33,36,40]. On the other hand, the drug success in cancer treatment is limited due to the side effects observable on the human body, including myelosuppression, dry heaving, diarrhea, risk of developing secondary leukemias, spillage of blood vessels, which can induce tissue ulceration, necrosis and, cardiotoxicity. Cardiotoxicity is the main side effect, leading to heart failure in the most

severe cases [31,40–42]. DOX-induced cardiotoxicity is cumulative and dose dependent, however, it may appear even at lower doses due to variations between individuals [34,43–45]. Cardiotoxicity includes both short- and long-term toxic effects in the heart, these can appear at any treatment stage and can be classified as acute or chronic. Additionally, cardiotoxicity can also lead to alterations in myocardial structure and function, severe cardiomyopathy as well as heart failure, that may result in the need for a transplantation or, in the worst-case scenario, it can lead to the patient's death [34,44,45]. Long-term anticancer treatment is another serious limitation. Continuous and prolonged administration of doxorubicin causes drug resistance in tumor cells, while increasing the cytotoxicity in healthy cells [46,47]. Due to the continued use of the drug, the cells start to express the P-glycoprotein, which transports the drug to the exterior of the cells, decreasing the amount of drug inside the cells and consequently making the drug not enough to inhibit cell growth [38,47].

There are some mechanisms proposed to explain how DOX causes cell death, including inhibition of topoisomerase II (DOX acts as a DNA intercalator), oxidative stress, DNA adduct formation and overproduction of ceramide. However, these mechanisms are not fully known [48,49]. The primary anti-tumor mechanism of DOX appears to be the intercalation in DNA that prevents DNA and RNA synthesis [36]. Structural explanations of DOX as a DNA intercalator have been proposed based on several techniques such as NMR analyses, high-resolution X-ray, molecular dynamic simulation, among others [49–51].

Several studies have been performed to understand this mechanism and it has been concluded that the amine group of doxorubicin is interleaved between base pairs of DNA double helix and they have a binding preference for G-C (Guanine-Cytosine) base pair. This intercalation will inhibit topoisomerase II (TOP2), which is an enzyme involved in the relaxation of coiled-coil DNA structures [34,47,49,50,52]. Inhibiting TOP2 functions will change the DNA topology, preventing the recombination of the DNA double strand, which leads to the production of double-strand DNA breaks, resulting in inhibition of DNA replication and transcription to mRNA, leading to the death of cells, as illustrated in Figure 4 [34,46,47,49,50].

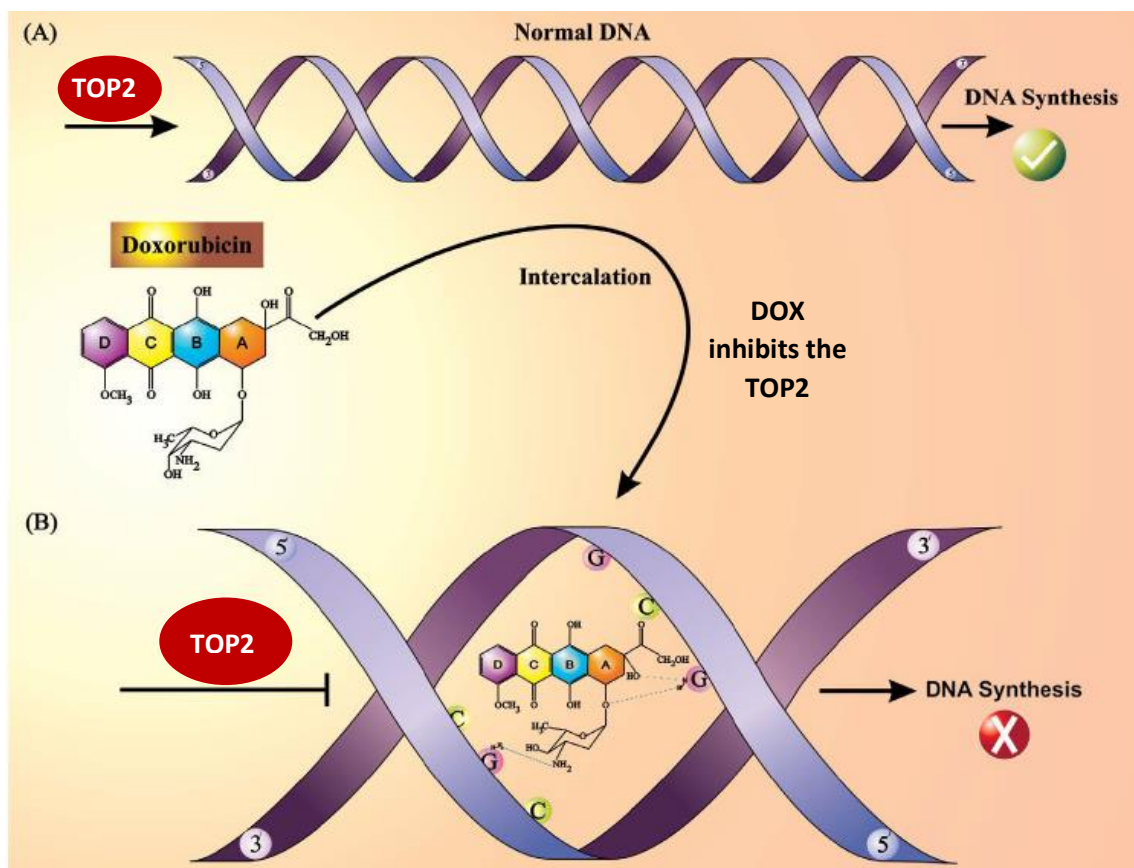


Figure 4: DOX intercalation into DNA. A) TOP2 relaxes DNA supercoil to facilitate replication and DNA synthesis; B) DOX forms a complex by DNA through G bases in both of DNA strands and prevents TOP2 activity and DNA synthesis. TOP2: Topoisomerase II, G: guanine, C: cytosine [34].

Due to the low absorption by the digestive system, DOX is not administered orally. In contrast, intravenous administration allows a better and quickly distribution to the human body. However, this route of administration does not make the treatment sufficiently effective and, beyond this point, the problem of toxicity still exists. Therefore, there is an urgent need to reduce its toxicity without compromising the therapeutic effectiveness. In order to overcome these side effects, researchers have investigated and developed new administration strategies for targeted drug delivery [40,41].

A new strategy, currently under development, is the use of nanosystems capable of transporting the drug to the tumor site, facilitating cell uptake and intracellular drug delivery. Thus far, there are several drug delivery nanosystems designed for this purpose and some of them, specific for DOX, were approved by Food and Drug Administration (FDA), including Doxil[®] (Johnson & Johnson, USA), Caelyx[®] (Janssen-Cilag, Belgium), Evacet[®] (Liposome

Company Inc., Princeton, NJ) and Lipodox[®] (Sun Pharma, Mumbai, India), Myocet[®] (Sopherion Therapeutics, USA) and ThermoDox[®] (Celsion Corporation, USA) [14,53]. In order to creating an ideal nanocarrier for drug delivery, it is necessary to adjust its different characteristics according to the path it must take, namely the composition, size, surface chemistry, shape and mechanical flexibility [14].

In order for nanosystems to be successfully used as drug carriers, such as DOX-loaded nanocarrier, some essential properties must be met: (i) they must have the ability to prevent drug leakage during transport; (ii) consequently must have the ability to do the controlled and targeted drug delivery, reducing systemic levels of the drug; (iii) ensure non-toxicity; and (iv) it must be stable in the complex biological environment with a prolonged lifetime in the bloodstream. When these basic conditions are met, it is possible to effectively improve the therapeutic effect while reducing the overall toxicity [14,36,41].

2.3. NANOTECHNOLOGY AND NANOPARTICLES

Nanotechnology plays an important role in many fields due to the possibility of developing new products with potential properties and functions. Nanoscience explores the phenomena, properties, and responses of materials at atomic, molecular, and macromolecular scales and involves nanostructured materials with dimensions between 1 and 100nm, as illustrated in Figure 5 [14,54].

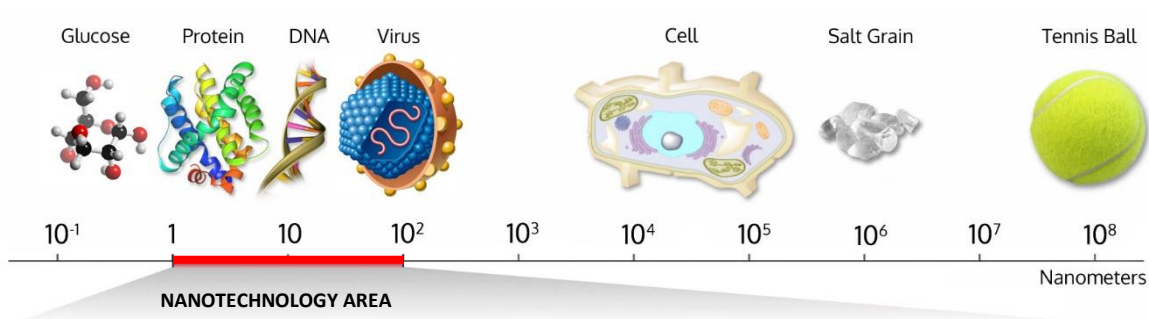


Figure 5: Length scale that compares the size of various biological components and some more familiar materials and objects [55].

Due to the unique properties achieved with nanotechnology, there are already many commercial products available including metals, ceramics, polymers, smart textiles, cosmetics, sunscreens, electronics, paints, and varnishes [54]. In addition to these products, there are many applications currently under development in the most diverse fields including biomedicine, tissue engineering, catalysis, sensors, energy storage, among others [56].

Nanotechnology has shown promise in the field of biomedicine, specially by improving dual diagnosis and individualized treatment against cancer and other diseases [13,41]. Nanocarriers systems used for drug delivery have received attention in recent years due to the advantages they provide over conventional drug delivery systems. Some advantages are increased stability and efficacy, improved bioavailability by enhancing the aqueous solubility of medicines, prolong the circulation time of chemotherapeutic drugs and protect them from degradation. Other key advantages include high surface area to load multiple drugs, enhanced interaction with cell membranes and proteins as nanosystems are similar in size, drug targeting, high concentration of drug delivering, decrease in the frequency of administration, reduced side effects and lower therapy costs [14,18,57].

Reducing toxicity and consequently, the side effects of drugs during treatments, is an important obstacle of nanomedicine that can be overcome with nanocarriers able to prevent drug leakage and deliver the drug to the specific site preventing the release in healthy tissues [18,41].

Besides the advantages of using nanotechnology to treat diseases, this field is also strongly valuable for diagnosis, helping to detect cancer in early stages. Furthermore, the online monitoring is also beneficial to assist treatment since it allows monitoring of drug release, in order to optimize the drug dosage to achieve an effective treatment [58].

The physicochemical properties of nanocarriers can be manipulated considering the knowledge of the different physiological conditions between healthy and diseased tissues and the route of administration. Thus, stimuli-sensitive nanocarriers can enhance the efficacy of therapeutic drugs through different physicochemical changes or stimuli such as temperature, redox potential, ionic strength, electrical field, and the biological fluid pH [18]. The pH-sensitive nanoparticles are the most used responsive drug delivery systems. The purpose of using this type of nanoparticles is to enhance *in vivo* stability, inhibit premature drug release,

prolong drug circulation time, and improve drug accumulation inside target tumors [18]. This is possible because while blood and most tissues have a neutral pH of 7.4 in healthy conditions, TME and intracellular endosome/lysosome microenvironments have a slightly acidic value of approximately 6.6 and 5-5.5, respectively, due to the atypical metabolic activity and subsequent high amounts of lactate and CO₂ as explained in section 2.1 [8,59,60].

Different types of nanocarriers have been employed for liver cancer therapeutics and diagnostic agents including carbon nanotubes, micelles, dendrimers, lipid nanocarriers, nanofibers, polymeric nanoparticles, graphene oxide, nano-shells, liposomes and superparamagnetic iron oxide nanoparticles (SPIONs), as seen in Figure 6. The nanostructured nanocarrier proposed in this work will be composed of several of them: a superparamagnetic iron oxide core will be coated with a graphene-based nano-shell which will be loaded with a chemotherapeutic drug (DOX).

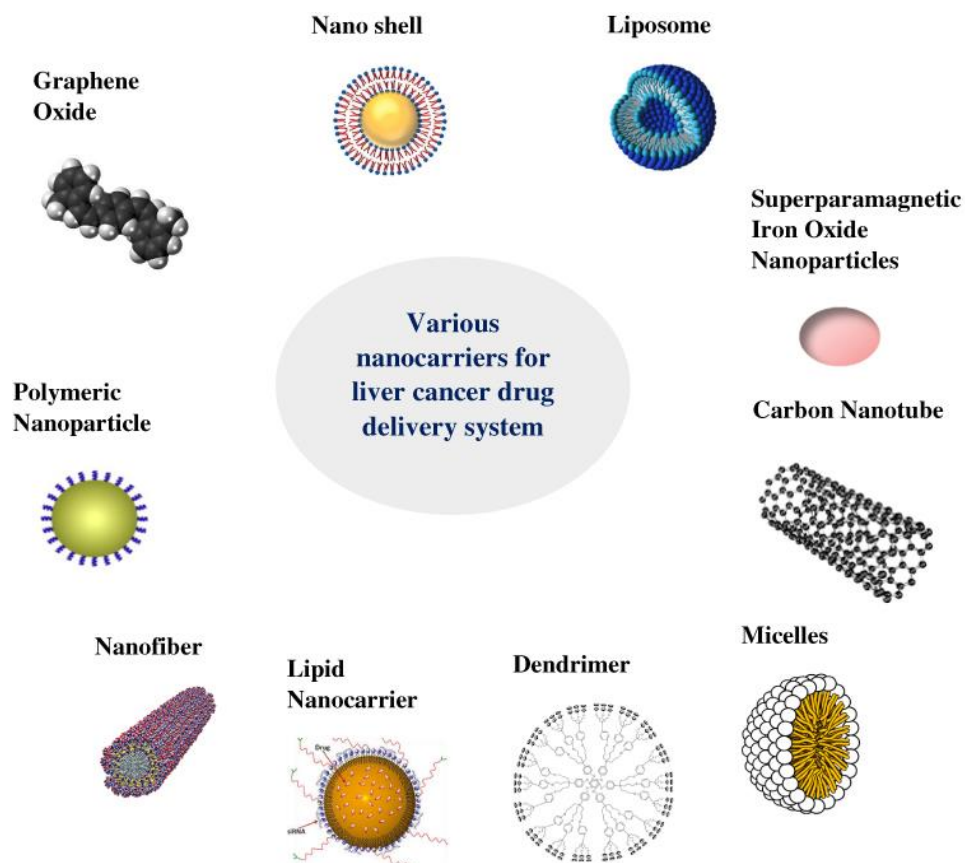


Figure 6: Different nanocarriers for liver cancer targeted drug delivery applications [61].

In order to contextualize the topic of this thesis and support the discussion of the results achieved some of these nanocarriers will be further described, in particular magnetic nanoparticles and carbon nanomaterials and their derivatives, which will be covered in the following sections.

2.3.1. Organic and inorganic nanoparticles

Nanoparticles can be divided into organic or inorganic. Within these sections there is a wide variety of sizes, shapes, and materials with vast chemical and surface properties [14,18].

Organic nanoparticles are prepared with organic molecules, for this reason they can be biodegradable, which makes them attractive for the administration of medicines and other diverse biomedical applications. They provide relatively simple routes for the encapsulation of materials and their association with biological entities, such as DNA and antibodies, allow the study of the behavior of some molecules, molecular recognition, signal transduction and protein-mediated membrane fusion processes [14,18]. Organic nanoparticles have emerged mainly for the performance of immunoassays and as a more effective alternative for the administration of drugs in order to reduce the chronic toxicity caused by non-degradable polymers. This type of nanoparticles allows easier manufacturing from biodegradable polymers, they have a high stability in biological fluids and during storage. There is a wide range of organic nanoparticles such as micelles, vesicles, and liposomes, polymersomes, polymer conjugates, dendrimers, nano shells and polymeric nanoparticles [14,18,61].

On the other hand, **inorganic nanoparticles** have gained attention in recent years due to their physicochemical properties dependent on material composition and size, such as optical, magnetic properties, among others, which are not possible with traditional organic nanoparticles based on lipids or polymers. In addition to these characteristics that make these nanoparticles attractive for a variety of applications, they have other advantages like being more stable and providing ease of functionalization [14,18,61]. The most commonly used inorganic nanoparticles are **magnetic nanoparticles (MNPs)**, gold nanoparticles, quantum dots and carbon nanotubes [14,62]. MNPs have been widely used in biomedical applications

such as biosensing, drug delivery, hyperthermia, magnetic resonance imaging and cellular capture. Magnetic nanoparticles are a key element for many biomedical applications and will constitute the cornerstone of the proposed work.

These two types of nanoparticles differ in terms of manufacturing principles. The inorganic ones are usually produced via precipitation of inorganic salts, which are linked in a matrix. Diversely, the organic nanoparticles are formed by several organic molecules that associate due to self-organization or chemical bonding [14,18,63].

2.3.2. Carbon nanostructures

Carbon is one of the primary elements for the formation of all organic matter. A carbon atom has ability to bind with itself and other atoms in different ways to form a varied combination of chains and rings, and consequently, giving rise to many distinct structural forms [64,65]. Examples of carbon-based nanostructures includes graphite, fullerenes, carbon nanotubes, diamond, graphene, among others [66,67]. A carbon atom has six electrons occupying $1s^2$, $2s^2$, and $2p^2$ atomic orbitals [65,68]. As $2p$ atomic orbital has the capacity to six electrons, where there are only 2 electrons occupied, carbon is able to form up to four bonds [68]. The energy difference between the upper $2p$ orbital and the lower $2s$ orbital is small when compared to chemical bonds. Thus, when bonding with other atoms, the electronic structure of the carbon atom can be hybridized² to adjust to different structural arrangements [65]. Particularly, graphene and its derivatives have attracted much attention in nanomedicine and biomedical applications due to their unique properties, such as high chemical and thermal stability, high charge carrier mobility, enhanced biocompatibility and large surface area, which are ideal for biofunctionalizations [69–71]. Graphene is a two-dimensional form of carbon, consisting of a planar sheet with carbon atoms arranged in a hexagonal lattice, in which atoms are linked by sp^2 hybridization, as seen in Figure 7A [65,72]. Graphene-based family is classified according to its number of layers and chemical modification. The most widely used graphene-based nanomaterials include monolayer graphene, bilayer graphene, multilayer

² Hybridization is a process that happens when the electrons of the upper $2p$ orbital and the lower $2s$ orbital can mix easily with each other to enhance the binding energy of the carbon atom with neighboring atoms [14].

graphene, graphene oxide (GO) and reduced graphene oxide (rGO). The different types of graphene-based nanomaterials differ from each other in terms of layers, surface chemistry, purity, lateral dimensions, defect density and composition [71].

Since graphene nanostructures have difficulty obtaining well-dispersed liquid suspensions without chemical additions, other graphene-based materials have emerged as an alternative for use in medical applications [70].

Graphene oxide, a common derived from graphene, is a highly oxidized version of chemically modified graphene consisting in a single monolayer with the attachment of different functional groups such as epoxy, carbonyl, hydroxyl, and carboxyl, as seen in Figure 7B [1,71,73]. These oxygen functionalities provide a hydrophilic nature and enable the nanostructure to disperse in water and other organic solvents without any additive [69,70]. Moreover, the peripheral carboxylate group provides pH-dependent negative surface charge and colloidal stability, while epoxide and hydroxyl groups allow weak interactions, hydrogen bonding and other surface reactions [71].

The reduction in the oxygen content either by thermal, chemical, or any other methods, produces rGO. This reduction of oxygen content forms defects in the carbon lattice, as show in Figure 7C, increasing the hydrophobicity and consequently the tendency to create aggregates [69].

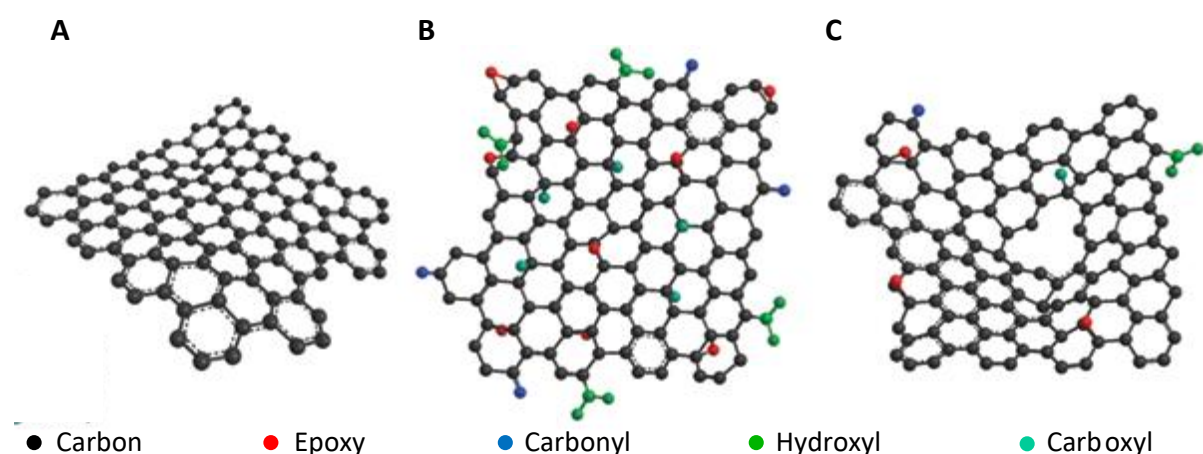


Figure 7: Schematic chemical structures of graphene-based nanostructures: (A) graphene; (B) GO and; (C) rGO [74].

GO and rGO can be improved through an additional functionalization. Since the presence of oxygen groups is bigger in GO, its reactivity is higher compared with rGO. In this way, GO can be chemically functionalized through covalent interactions easier than rGO [64,70]. This makes this material an ideal candidate to improve specific properties of magnetic nanostructures (e.g. MNPs), namely increasing colloidal stability and reducing toxicity. Also, because of their large surface area, GO nanosheets have attracted considerable interest for imaging diagnostic applications and drug delivery [64,70].

Despite all its applications, MNPs also have some limitations, in particular, they tend to aggregate and precipitate into biological vessels, reducing their colloidal stability and biocompatibility. In this regard, the combination of graphene-based nanostructures with MNPs, resulting in graphene-based magnetic nanoparticles (GbMNPs), has attracted huge interest in biomedicine because the resulting blend allows to overcome the limitations of MNPs and exploit the properties of both materials [75].

2.4. MAGNETISM

Magnetism is a basic property of any material, arising from the presence of atoms with nucleus (protons and neutrons) and the orbiting electrons in motion. Since all materials have electrons, they all have the ability to interact with a magnetic field, which is dependent on the ordered or disordered movement of the electrons, as explained below [76,77].

The concept of magnetism in solids is closely related to the orbital movement of electrons around the nucleus and to the rotation movement of electrons.

Thus, the movement of the unpaired valence electrons is responsible for the production of a **spin magnetic moment** and an **orbital magnetic moment**, as shown in Figure 8A and 8B, respectively [77–79].

Following this concept, when an external magnetic field is applied to a solid, the magnetic dipoles inside the material are aligned with the direction of the applied magnetic field and consequently, the magnetic dipoles are magnetized.

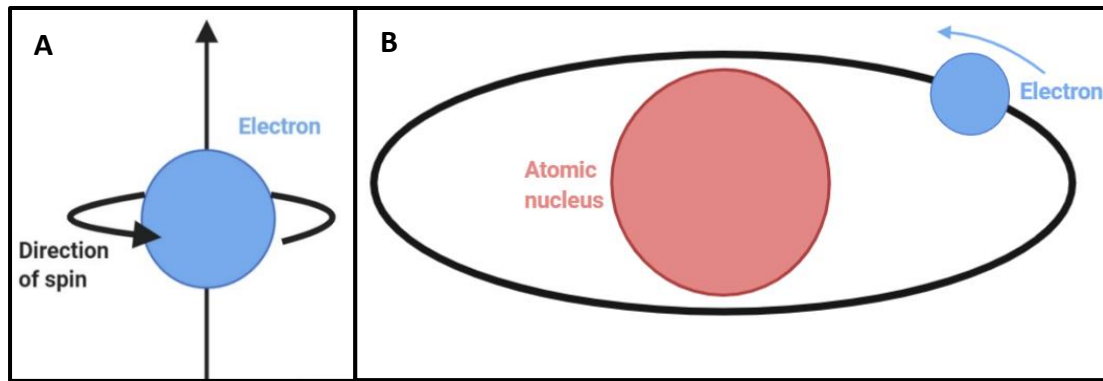


Figure 8: Schematic representation of magnetic moments. (A) Spin magnetic moment; (B) Orbital magnetic moment. Drawn in Biorender.

The response of a material when an external magnetic field with force H is applied to it is called **magnetic induction** or magnetic flux density, represented by B (in Tesla or T), that describes the number of field lines per unit area. Magnetic induction can be expressed by **Equation 1** [79,80]:

$$B = \mu_0 (H + M) \quad \text{Equation (1)}$$

Where μ_0 is the permeability in vacuum, H is the magnetic field strength and M is the magnetic moment per volume.

Materials can be classified according to their magnetic behavior and can be mainly differentiated by **paramagnetic**, **ferromagnetic**, and **diamagnetic**, which correspond to the different types of magnetism: paramagnetism, ferromagnetism, and diamagnetism, respectively.

- Oxygen, platinum, aluminum, and manganese are examples of **paramagnetic** materials, in this case, their magnetic moments when subjected to an external magnetic field will have a weak alignment parallel to the direction of the field, because the spins are randomly oriented (Figure 9a). In other words, only a few electrons of the material align with the electrons in the external magnetic field. Hence, the magnetic susceptibility of these materials is moderately strong and positive [76,77,81].

- Examples of **ferromagnetic** materials are iron, cobalt, and nickel. These materials have a strong attraction for magnetic fields due to the parallel alignment of their magnetic

moments (Figure 9b). The forces will be added, and the resulting magnetic field value will be strongly positive. Thus, its magnetic susceptibility is very strong and positive [76,80,82].

- Copper, gold, water, and silver are examples of **diamagnetic** materials. These materials behave in the opposite way to the previous ones. When subjected to external magnetic fields, the magnetic moments will have a weak alignment in the opposite direction (Figure 9c), and consequently, will be slightly repelled from the magnetic field. The magnetic susceptibility of these materials is weak and negative [76,77].

In addition to these three types of materials, the antiferromagnetic and ferrimagnetic materials are considered subclasses of ferromagnetic materials.

Nickel oxide and manganese (II) oxide are examples of antiferromagnetic materials. When an external magnetic field is applied to these materials, the spins are aligned antiparallel, i.e., the unpaired electrons line up opposite to one another (Figure 9d), resulting in a small magnetization [77].

Magnetite (Fe_3O_4) and maghemite (Fe_2O_3) are the most common examples of ferrimagnetic materials, commonly used for biomedical applications, such as magnetic hyperthermia. These materials are generally referred as magnetic iron oxide nanoparticles (MIONs). The behavior of these materials is similar to antiferromagnetic materials because the magnetic moments are aligned antiparallel, but with an unequal (unbalanced) and greater magnitude value (Figure 9e) [17,76,77].

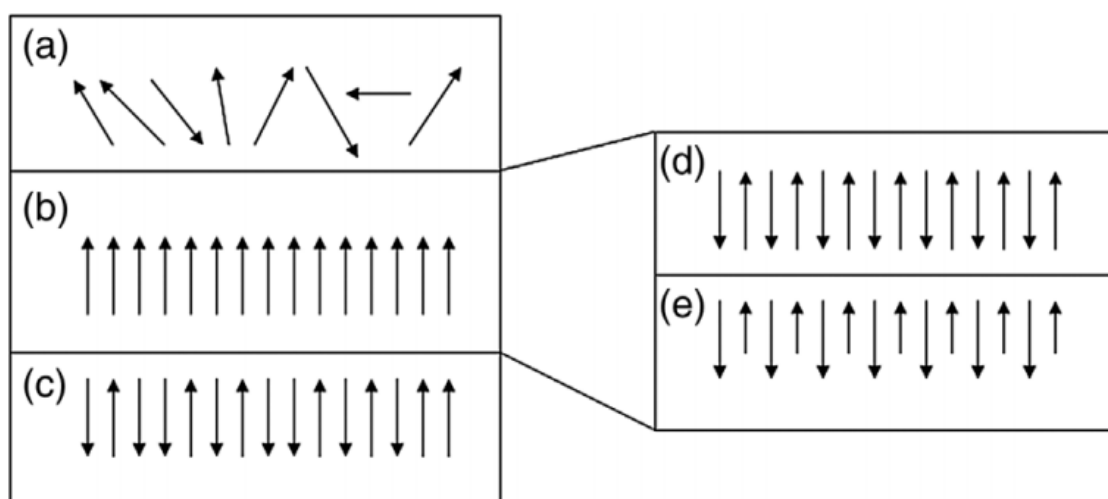


Figure 9: Types of magnetism under an externally applied magnetic field. (a) Paramagnetism; (b) Ferromagnetism; (c) Diamagnetism; (d) Antiferromagnetism; (e) Ferrimagnetism [77].

The magnetization of paramagnetic and diamagnetic materials quickly disappears when the magnetic field is removed. However, the ferri- and ferromagnetic materials have an outstanding feature: the magnetic moment is maintained towards the inductive field even after it is removed [5]. This behavior is called remanence or hysteresis, that results from the blockage of the magnetic domains, remaining a memory of the removed field [76]. This theme will be addressed later to explain the importance of these behaviors.

Hysteresis can be evaluated through the **hysteresis loop**, a magnetization curve that represents the variation of magnetization (M) versus the magnetic field strength (H), as shown in Figure 10. There are three parameters that can be found in the hysteresis loop [77]:

- (i) **Saturation magnetization (M_s)**: when a ferri- or ferromagnetic material is subjected to an external magnetic field, all magnetic domains tend to align in the direction of the applied field, reaching its M_s , which corresponds to the maximum magnetization value that can be achieved by material [77].
- (ii) **Remanence magnetization (M_r)**: after the external magnetic field is removed, the magnetization does not return to zero. This behavior occurs in materials that have magnetic memory and that have the ability to maintain magnetization even after removing the applied external field, resulting in a state of magnetic remnant [77].
- (iii) **Coercivity (H_c)**: represents the intensity that needs to be applied to reduce the magnetization back to zero. This parameter is related to the minimum energy required to reverse the magnetization [77].

These parameters can be measured from the hysteresis loops (M-H) of the material. On the other hand, the hysteresis losses can be measured by integrating the area of the hysteresis loop (shaded area in Figure 10a). when the applied magnetic field is alternating, this area directly represents the power loss during one cycle of the loop, this means that the heat generation rate is proportional to the frequency of the alternating magnetic field (AMF) [19].

In addition to the types of magnetism mentioned above, there is another case, the superparamagnetism, that occurs in small size ferromagnetic or ferrimagnetic nanoparticles, usually less than 20 nm. They are **not** able to retain the magnetic memory when the external magnetic field is removed. Thus, when the magnetic field is removed, the magnetic moment

of the material is quickly reoriented, leading to a loss of energy that heats the surrounding environment (when an AFM is applied) [63,77,80,83].

The smaller the size of the nanoparticles, the lower the number of magnetic domains (small regions of the material that are spontaneously magnetized). In more extreme cases, they have a single domain, since below a critical size, the formation of multiple domains is not favorable in terms of energy. When the size of the nanoparticle is very small, thermal energy is enough to overcome the energy barrier and force the magnetic moments to reorient. In this case, the M-H curve does not show hysteresis, and the magnetization curves overlap, exhibiting zero magnetic remanence, as can be seen in Figure 10b). [79,83–85].

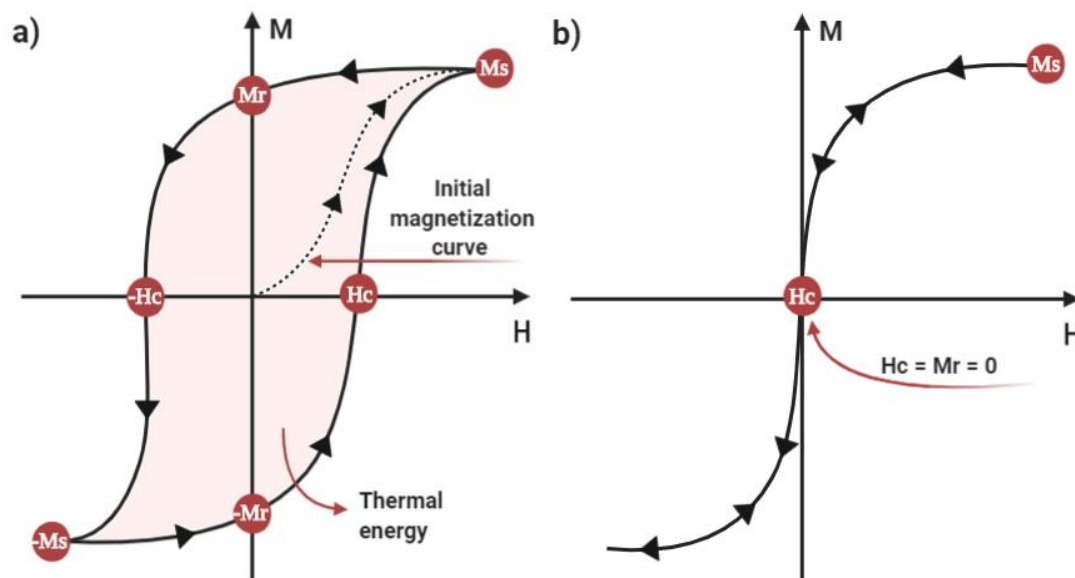


Figure 10: Schematic illustration of typical hysteresis loops of: (a) ferromagnetic; (b) superparamagnetic materials. Drawn in Biorender inspired by refs. [77,83,86].

Magnetic nanoparticles with magnetic remanence are not popular for biomedical applications because they tend to interact magnetically after removal of the magnetic field, forming clusters and aggregates of nanoparticles. Thus, if these nanoparticles are injected intravenously, there is a high risk of aggregation, which can result in the formation of clots and embolisms. On the other hand, superparamagnetic iron oxide nanoparticles are highly desirable for biomedical applications, because it minimizes the agglomeration of the particles is minimized after removal of an applied magnetic field [87]. Thus, single-domain

superparamagnetic nanoparticles with their special peculiarities (zero remanence magnetization), find application in several areas of nanomedicine, such as enhancement magnetic resonance imaging (MRI) contrast enhancement, drug delivery, cell and tissue targeting, and magnetic hyperthermia [77,79].

The magnetic nanomaterials when exposed to an AMF, can produce heat by two main mechanisms: i) hysteresis losses coming from their ferromagnetic-like behavior, as mentioned above; and ii) when using superparamagnetic nanoparticles, the heat is generated from relaxation processes. In this case, the heat is produced due to the delay in the relaxation of the magnetic moment through either the Néel relaxation and Brownian relaxation, as depicts in Figure 11 [17,19,88].

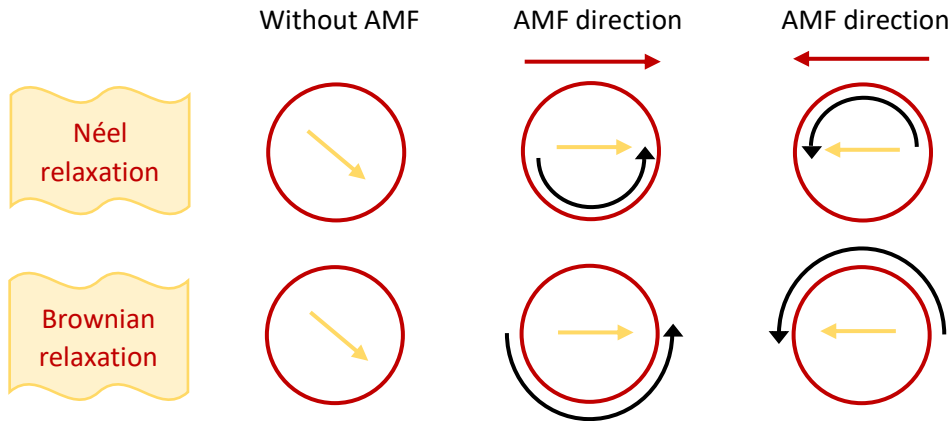


Figure 11: Heat generation mechanisms in superparamagnetic nanoparticles in response to an AMF. The short straight arrows represent the magnetic moment direction, the curved arrows represent the movement or change in direction. Based in [88].

Néel relaxation refers to the heating due to the energy loss generated by the rotation within the particle, while Brownian relaxation refers to the heating by rotation of the particle itself and the friction with the solvent, due to the alignment of magnetic moments with the external AMF [88,89].

The Néel relaxation time (τ_N) and the Brownian relaxation time (τ_B) are given by the following equations [88,89]:

$$\tau_N = \tau_0 e^{\frac{KAV}{k_B T}} \tag{Equation (2)}$$

$$\tau_B = \frac{3\eta V_H}{K_B T} \quad \text{Equation (3)}$$

Where τ_0 is the time constant ($\tau_0 = 10^{-9}s$), K_A is the anisotropy constant V is the volume of the MNP, K_B is the Boltzmann constant, T is the absolute temperature, η is the dynamic viscosity of the liquid carrier and V_H is the hydrodynamic volume of the particle [88,89]. Since heat dissipation by Brownian relaxation is strongly dependent on the local environment such as the viscosity of the medium, the use of MNPs that dissipates heat by Néel relaxation (which is not viscosity-dependent) is preferred for magnetic hyperthermia applications, because the MNPs can reduce their rotation at high viscosities and consequently the heat dissipated by these particles will decrease [88,89].

The quantification of the power dissipation of MNPs can be formulated in term of specific absorption rate (SAR), expressed as $W\ g^{-1}$, which is given by **Equation 4** [17,90]:

$$SAR = \frac{C}{m_{MNP}} \frac{\Delta T}{\Delta t} \quad \text{Equation (4)}$$

Where C is the heat capacity of the medium, m_{MNP} is the mass of magnetic material, and ΔT is the temperature rise during the time interval (Δt) [90]. The SAR is a parameter used to quantify the heat produced via magnetic induction of MNPs that must be maximized under an AMF [17,91].

2.5. MAGNETIC NANOPARTICLES (MNPs)

Magnetic nanoparticles have been an important nanomaterial for science and technology in recent years. They can have different unique properties such as superparamagnetic behavior, high coercivity, low Curie temperatures³ (T_c), high magnetic susceptibility, large surface-to-volume ratio, and high saturation magnetizations when

³ Curie temperature is a transition temperature from an ordered magnetic state to a disordered magnetic state. As magnetic hyperthermia and the application of an AMF is concerned, the MNPs lose their magnetic properties (which causes the current flow) and the heat production is suppressed above T_c . [16]

compared to their bulk materials. Superparamagnetic behavior rises from the large magnetic moment they achieve in the presence of an external magnetic field, which is blocked when the field is removed [92].

Currently, magnetic nanoparticles are a promising tool in many fields. Due to their features, magnetic nanoparticles have a large impact on medical applications, commonly known as nanomedicine, including drug delivery systems, magnetic resonance imaging (MRI) contrast enhancement, magnetic hyperthermia, computed tomography, tissue engineering, and other applications. The use of magnetic materials in medical health area enables several medical technologies and allows for the diagnosis and treatment of many diseases, especially cancer [14,16,93]. Thus, MNPs can be used as heat effectors through magnetic hyperthermia under an AMF and consequently, the heat can be applied for the direct ablation of tumors. Furthermore, MNPs contribute significantly to the real-time visualization of other biological behaviors such as trafficking, cancer metastasis, cellular signaling, and interactions at the molecular and cellular levels [14].

2.5.1. Composition

Typically, MNPs are composed of a magnetic core, usually pure metals (Fe, Co, and Ni), alloys (FeCo, alnico, and permalloy), and iron oxides (magnetite (Fe_3O_4) or maghemite ($\gamma\text{-Fe}_2\text{O}_3$)). Although pure metals can produce higher saturation magnetization, they are not suitable for clinical use due to their high toxicity or low biocompatibility and they tend to be susceptible to oxidation. The use of **magnetic iron oxide nanoparticles** (MIONs) has the additional advantages of the body processing the excess of iron, since iron is an essential component of the human body, which is explained in more detail in Palmer et al. [14]. Their high chemical and colloidal stability, high biocompatibility, existence of natural routes for its biodegradation, and low cost are also advantages of using MIONs [14,92,94].

Among iron oxides, magnetite (Fe_3O_4), maghemite ($\gamma\text{-Fe}_2\text{O}_3$) are the most popular materials employed for biomedical applications due to their biocompatibility and low toxicity in the human body, and notable magnetic properties. Another common form of iron oxide is

hematite ($\alpha\text{-Fe}_2\text{O}_3$) which is less used for these areas due to its weak magnetic properties at room temperature (RT), as shown in Table 3 [87,94].

Table 3: Physical and chemical properties of magnetite, maghemite, and hematite [77,87].

Properties	Magnetite	Maghemite	Hematite
Molecular formula	Fe_3O_4	$\gamma\text{-Fe}_2\text{O}_3$	$\alpha\text{-Fe}_2\text{O}_3$
Crystal structure	Cubic	cubic or tetrahedral	rhombohedral
Density (g cm^{-3})	5.18	4.87	5.26
Melting point ($^\circ\text{C}$)	1583-1597	-	1350
Color	Black	reddish-brown	red
Hardness	5.5	5	6.5
Magnetism	ferrimagnetism	ferrimagnetism	ferrimagnetism
Curie temperature (K)	850	820–986	956
M_s , at 300 K ($\text{Am}^2 \text{kg}^{-1}$)	92-100	60-80	0.3

Magnetite (Fe_3O_4) has the most interesting properties because of the presence of iron cations in two valence states, Fe^{2+} and Fe^{3+} , with trivalent ions occupying both tetrahedral and octahedral sites in the inverse spinel oxide structure, as seen in Figure 12b) [77]. Magnetite has an oxygen cubic close-packed structure, where Fe^{2+} ions occupy half of the octahedral sites and Fe^{3+} are split evenly across the remaining octahedral sites and tetrahedral sites. Fe_3O_4 has acquired great importance because of its characteristic magnetic properties such as high M_s [63,77,95,96]. In the presence of oxygen, Fe (II) cations are oxidized to Fe (III) at the surface generating maghemite ($\gamma\text{-Fe}_2\text{O}_3$). This exhibits a highly crystallinity with variable sizes and has a cubic or tetrahedral spinel structure with some cation deficiency (Figure 12c)) [63,77,97]. Conversely, hematite ($\alpha\text{-Fe}_2\text{O}_3$) crystallizes in the rhombohedral structure and is thermodynamically the most stable crystallographic phase of Fe_2O_3 (Figure 12a)). It can be used as a starting material for the synthesis of magnetite and maghemite, which have been strongly studied for technological applications in the last few decades [63,77,96,98,99].

Therefore, for biomedical applications, magnetite and maghemite are the most promising materials due to their biocompatibility and great magnetic properties when properly synthesized with high crystallinity at the nanoscale, since they are easily oxidized in air (especially magnetite), generally resulting in loss of magnetism and dispersibility [62]. Thus,

in an attempt to keep the stability of MIONs it is essential to provide proper surface coating and develop some effective protection strategies [100].

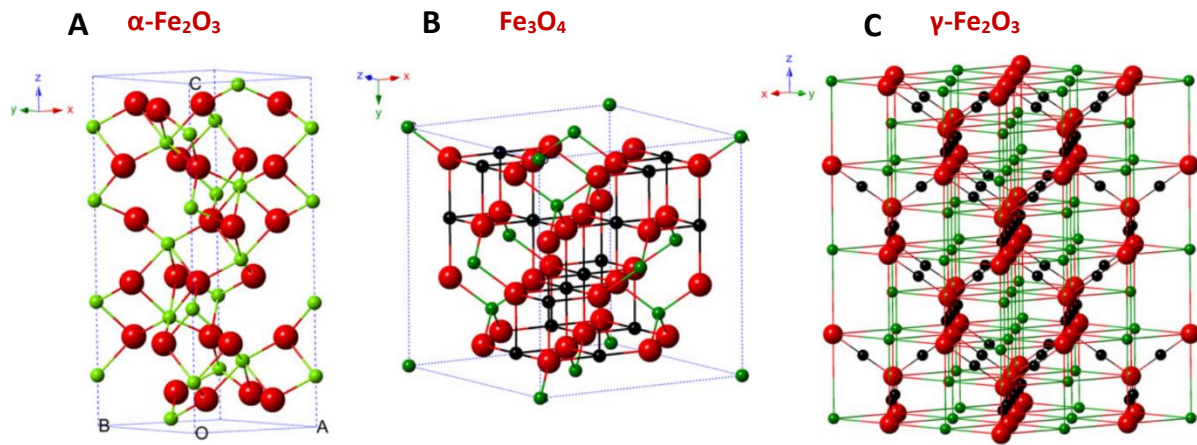


Figure 12: Crystal structure of (A) hematite ($\alpha\text{-Fe}_2\text{O}_3$); (B) magnetite (Fe_3O_4); (C) maghemite ($\gamma\text{-Fe}_2\text{O}_3$) [96].

2.5.2. Synthesis methodologies

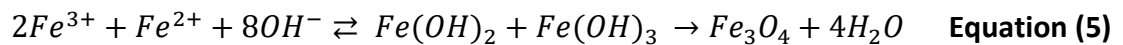
Some properties of MNPs are dependent on the particle size, as previously mentioned. On the other hand, coercivity depends on the size and shape of particle due to anisotropy effects. Therefore, the manipulation of particle structures is essential for the control of intrinsic magnetic properties. Thus, a big variety of magnetic nanoparticle structures can be found that were designed to maximize some aspects of their magnetic performance, for example, spherical core-shell nanoparticles, hexagonal core-shell nanoparticles, multiple small cores coated by a single-shell material, among others [77].

In the recent past, advances in the synthesis of MNPs were focused on improving their biomedical applications, taking into consideration requirements in terms of size, surface chemistry and colloidal stability under physiological conditions which are intrinsic to the targeted application *in vivo* [62,77]. In this section, an overview of the main MNPs synthesis procedures is presented. MNPs can be synthesized via physical, chemical or biological methods, each one with their own advantages and disadvantages. We will focus on colloidal chemical synthesis methods that allow for efficient and precise control of particle size,

composition, and surface chemistry. Typical wet-chemistry methods to synthesize iron oxide MNPs include coprecipitation, thermal decomposition, and hydrothermal synthesis [62,77].

Coprecipitation:

Coprecipitation of iron salts in aqueous alkaline conditions is the simplest and most efficient method to synthesize iron oxide nanoparticles ($Fe_3O_4/\gamma-Fe_2O_3$). This procedure consists of mixing Fe^{2+} e Fe^{3+} in a 1:2 molar ratio in strong base solutions at room or elevated temperature, which leads to instant magnetite precipitation according to the following reaction [62,77,81,87,96]:



The size, shape and crystal structure of the resulting nanoparticle can be strongly influenced by pH, type of base, ionic strength, reaction temperature and Fe^{2+}/Fe^{3+} ratio [62,87].

The coprecipitation has been the most used procedure for the synthesis of iron oxide nanoparticles, since it is simple, fast, cost-effective, and its main advantage is that a large number of nanoparticles can be synthesized. However, it provides poorly crystalline particles and poor control on size distribution, resulting in polydisperse nanoparticles [81,100].

Polymers such as dextran or polyacrylic acid can be added in the reaction media, or the particles can be coated in a subsequent step, in order to act as protecting agent for controlling particle size and stabilizing the colloidal dispersions [62,100].

Thermal decomposition

The thermal decomposition procedure requires a high temperature and long reaction duration under an inert atmosphere (to avoid the possible oxidation in the air). By adding suitable surfactants, it is possible to improve the crystallinity of the iron oxide nanoparticles and obtain precise size and shape-controlled nanoparticles [62,81,96]. Magnetic nanocrystals with small size, high monodispersity, and good crystallinity can

be synthesized through the thermal decomposition of organometallic compounds in high-boiling organic solvents containing stabilizing surfactants. The synthesized nanoparticles have a hydrophobic surface and are dispersible in an organic solvent [62,81,101]. These types of solvent are energy-intensive, employ toxic chemicals, and yield nanoparticles in nonpolar solutions. Besides, to be applied in the medical area, extra steps are needed after synthesis by thermal decomposition, to colloidally stabilize the nanoparticles in an aqueous solvent [62,81,101].

Hydrothermal synthesis

Hydrothermal synthesis allows to obtain hydrophilic nanoparticles in an aqueous solution in one-step synthesis by hydrothermal reduction of Fe (III) salts in an autoclave at high temperature and pressure. Selecting an appropriate mixture of solvents and varying different parameters such as temperature, pressure, and reaction time, it is possible to reach a narrow size distribution [62,87].

The main advantages of using this method include a high degree of product purity, high crystallinity, and uniform morphology. Also, the use of non-specialized equipment and a simple general process make it a commonly used method [62,102].

This highlights the importance of selecting the proper synthesis methodology considering the final application. Thus, it is also necessary to know the advantages and disadvantages of each method. Table 4 shows the differences between the main methods used for the synthesis of iron oxide nanoparticles [77,96].

Table 4: Summary comparison of the synthetic methods [77,96].

Synthetic method	Synthesis	Reaction temperature	Reaction period	Solvent	Size distribution	Shape control
Coprecipitation	Very simple, environment	20-90 °C	minutes	water	Polydisperse	Not good
Thermal decomposition	Complicated, inert atmosphere	100-320 °C	Hours-days	Organic compound	Very narrow	Very good
Hydrothermal synthesis	Simple, High pressure	220 °C	hours	Water-ethanol	Relatively narrow	Very good

2.5.3. Surface modification strategies

Over long periods of time the particles can lose their colloidal stability and tend to agglomerate in order to reduce the energy associated with the high surface area-to-volume ratio, limiting their applications. Therefore, surface functionalization is able to increase biocompatibility and decrease the surface area to volume ratio, consequently reducing aggregation [81].

MNPs are composed of a magnetic core and depending on the applications, it can be modified with a biocompatible material resulting in a core-shell architecture [94]. Besides, it is possible to perform various surface functionalizations according to the desired applications [94]. In biomedical applications, the shell plays an important role, as it acts as a hydrophilic layer to improve colloidal stability and prevent aggregation of nanoparticles under physiological conditions. Additionally, providing better stability, the shell can prevent the oxidation of the core material. Biocompatibility or low toxicity of materials when exposed to cells is the key property to achieve good translational results [14,92].

In order to achieve high biocompatibility and guarantee a safer application of MNPs in nanomedicine, keeping their properties, such as colloidal stability, an organic or inorganic biocompatible coating is highly recommended [14,62]. Moreover, surface functionalization of MNPs, in addition to enhance stabilization and dispersion, can also improve heat generating efficiency [62]. There is a wide amount of substances that can be used as coating materials, among these, the most common are silica [16], carbon [66,67], gold [40,62], polyethylene glycol (PEG) [15,41,57], chitosan [103,104] and dextran [17,105].

2.6. GRAPHENE-BASED MAGNETIC NANOPARTICLES (GbMNPs)

Graphene-based nanostructures are widely researched because of its physicochemical properties, including high surface area ($2630 \text{ m}^2 \text{ g}^{-1}$) compared to any other nanomaterial since all of its atoms are on the surface, excellent electrical conductivity (1738 s m^{-1}), strong

mechanical strength (about 1100 GPa), unparalleled thermal conductivity ($5000 \text{ Wm}^{-1} \text{ K}^{-1}$), high charge carrier mobility and facility for a wide variety of functionalities [71,106,107].

These nanostructures contain a large negative surface area with free surface π electrons from unmodified areas of graphene, making them hydrophobic materials with the ability to adsorb a diversity of aromatic biomolecules and single-stranded DNA through a π - π stacking interactions and/or electrostatic interaction, which make them excellent materials for the design of biosensors, loading drugs and non-covalent functionalization [71,107].

The utilization of graphene-based nanomaterials combined with magnetic nanoparticles offers key benefits in the modern biomedicine. When exposed to air, magnetic nanoparticles rapidly agglomerate, reducing the surface area. Therefore, combining Fe_3O_4 with graphene-based materials, with their unique properties mentioned above, it is possible to increase the dispersion of nanoparticles, resulting in a desired nanosystem [108]. Besides, the large surface area of graphene makes the magnetic nanoparticles efficiency drug nanocarriers, while the magnetic properties provides ideal characteristics to act as nanoheaters with magnetic hyperthermia and as contrast agents for MRI [75]. Due to these outstanding combined properties, GbMNPs have shown high potential in biomedical applications [69,70].

2.6.1. Biomedical applications of GbMNPs

MNPs, in particular graphene-based magnetic nanoparticles, have been widely employed in many biomedical applications due to their excellent biocompatibility, such as tissue engineering, biosensors, gene delivery, cell separation, with special emphasis on theranostic applications. For diagnostic applications, their use as contrast agents for magnetic resonance imaging (MRI) to identify pathologies at early stage has been strongly studied. Simultaneously, their therapeutic applications have been focused on drug delivery and magnetic hyperthermia (MH). These main applications have been used for the treatment and diagnostic of cancers in the brain, breast, lung, liver, and prostate [16,62,71,109]. In this work, GbMNPs will be evaluated as multifunctional responsive drug delivery systems, able to act as heat effectors in magnetic hyperthermia and as contrast agents in MRI in the context of hepatic cancer.

2.6.1.1. Magnetic Resonance Imaging (MRI) contrast agents

Tracking and monitoring are essential tools for diagnosis and treatment assistance of different diseases, including tumors. Several imaging techniques have been employed for this purpose, including positron emission tomography, single photon emission computed tomography, bioluminescence imaging, fluorescence imaging, X-ray based computed tomography, and magnetic resonance imaging [110].

MRI is currently one of the most powerful imaging tools, it is the most efficient available and non-invasive technique to obtain real-time images of soft tissues. For this reason, this method has been extensively applied for clinical diagnosis of many diseases in human soft tissues [4,6]. MRI possesses various advantages over other imaging methods, including high spatial resolution ($\sim 100 \mu\text{m}$), long effective image window, rapid *in vivo* acquisition of images, and absence of exposure to ionizing radiation [110,111]. However, it has low sensitivity, which makes it difficult to visualize slight changes in biological tissues, and consequently prevent detection of tumors in early stage or small anatomical alterations. To overcome this limitation and increase its sensibility, the use of contrast agents (CA) is very attractive, improving the contrast of the acquired MR images. They are introduced into an organism to enhance imaging quality, being able to give anatomical and functional information [111,112].

MRI is based on the nuclear magnetic resonance (NMR) principle, where the nuclear magnetic moment of water protons in biological tissues aligns with an external magnetic field and consequently excited with a radiofrequency wave, producing an electric signal. Human body is composed of $\sim 60\%$ of water, what makes MRI a powerful technology to visualize internal tissues or organs [111,113]. In this regard, the role of contrast agents is to decrease the **relaxation time**⁴ of water protons and consequently, increase the image quality through enhancing the contrast between healthy and disease tissue [103,114]. The CA can be distinguished into two groups, T_1 agents that reduce the proton longitudinal relaxation time, resulting in a positive contrast (bright signal) and T_2 agents that can shorten the proton

⁴ Relaxation is the term used to describe the movement of nuclear spins to their initial low-energy state when the radiofrequency wave is removed [111].

transverse relaxation time, leading to a negative contrast (dark signal) [114,115]. To characterize the ability of T_1 and T_2 CA to decrease relaxation times of water protons, relaxivity r_1 and r_2 , respectively, are the most used parameters [112,116]. The most commonly applied CA are paramagnetic gadolinium (Gd^{3+}) chelates, which act as a positive CA, however, they still have some limitations such as (i) relatively low sensitivity, (ii) can present toxic side effects, and (iii) they show a short circulation time, which prevents high-resolution and/or targeted MRI. These limitations are indicative that better contrast agents, with high efficiency and sensitivity, need to be developed [111,115,116]. Nanostructures have shown promise with advantages over conventional agents. These nanometer-scale materials provide extraordinary magnetic properties and the ability to work at the cellular level [103]. Particularly, SPIONs have become attractive to be used as T_2 MRI CA because of their superior properties such as large magnetic moment and biocompatibility, which are essential for biomedical and clinical applications [115,117]. SPIONs of several formulations have been approved by the FDA and they are commercially available as MRI CA, including, Feridex[®] for liver and spleen imaging, Resovist[®] for liver imaging, Lumiren[®] for bowel imaging and Combidex[®] for lymph node metastases imaging [118,119]. The assembly of SPIONs with graphene oxide has become attractive for efficient magnetic images, with better results compared with single SPIONs. Chen *et al.* synthesized iron oxide nanoparticles conjugated to graphene oxide, loaded with DOX that showed good physiological stability, low cytotoxicity and enhanced r_2 relaxivity.

2.6.1.2. Drug delivery

As previously mentioned (section 2.2), DOX has been used as a chemotherapeutic agent for cancer treatment because of its powerful cell-killing ability [75]. However, the use of this drug is limited due to its toxic effects. Researchers have focused on developing targeted nanoparticles that will effectively deliver the drug to the tumor site without damaging the healthy tissues, while increasing the efficacy and reducing its toxicity [75,109]. Combining superparamagnetic iron oxide nanoparticles with graphene-based nanomaterials can be useful in drug delivery applications [71].

Moreover, GbMNPs possess a high surface area and large sp² hybridized carbon area with π - π stacking and negative surface charge, allowing the adsorption of a diversity of aromatic biomolecules, such as chemotherapeutic drugs [71,107]. After achieving a high drug loading into the nanocarriers, the drug can be released and accumulated specifically in the tumor i) via active targeting, where the nanoparticles are functionalized with antibodies and peptides with high affinity to the specific tumor cells receptors or ii) via enhanced permeability and retention effect (passive targeting), where positively charged nanoparticles are accumulated in the tumors due to the leaky vasculature and low functioning immune system of the area [75,109,120]. In addition, this non-covalent interaction mechanism allows a drug release triggered by changes in physiological conditions, i.e. specific stimuli, such as pH, osmolality or temperature [75,109]. Thus, GbMNPs have the ability to behave as pH stimuli-responsive controlled drug release systems, triggered by the acid pH values (around 5-5.5) characteristic of tumor microenvironments. This remarkable capability is attributed to π - π stacking interactions that allow the adsorption of a diversity of aromatic biomolecules, and to the presence of oxygen and hydrogen-containing surface groups, promoting hydrogen bond interactions [60,121]. Therefore, these properties of GbMNPs make them promise multifunctional nanocarriers for therapeutic applications such as efficient drug delivery and, consequently, represent a huge impact on cancer management.

2.6.1.3. Magnetic Hyperthermia

In the recent years, hyperthermia has been playing an important role in biomedical applications and has been widely employed for cancer treatment.

It has been shown that hyperthermia combined with other conventional methods for cancer treatment, such as radiotherapy and chemotherapy, improves the effectiveness of treatment [17,19]. Hyperthermia is the term used when body tissue is exposed to small temperature changes of 5 to 7° above body temperature, resulting in cancer cell apoptosis whilst healthy cells remain relatively intact [122,123]. Tumor cells are more vulnerable to temperature increases than healthy cells, since the tumor has a hypoxic environment and disorganized and compact vascular structure which results in difficulty of heat dissipation

[124]. Several techniques have been used to successfully apply hyperthermia and induce cell death, including microwaves, laser and ionizing radiation [125]. However, in these techniques most of the energy is dissipated in healthy cells that are in the path of external radiation, which can cause serious side effects [123,126]. Despite all these strategies to achieve a small temperature increase in the human body, the resulting toxicity between cancer cells and healthy cells remains similar. Which makes hyperthermia a cancer treatment that still presents several obstacles to overcome. With these barriers, there is a need for more precise, controlled and localized heating in order to improve efficiency [16,19].

The use of magnetic hyperthermia therapy is a new strategy designed to achieve success in clinical applications, such as cancer treatments [16,17]. Nanotechnological developments have allowed the introduction of magnetic nanoparticles in this ambit, in particular the SPIONs, that are desired since they allow better dispersion of nanoparticles and avoid the formation of particle aggregations [88]. They can accumulate at the tumor site and act as heat-inducing agents by applying an AMF [14,16]. With targeted heating in the tumor, hyperthermia is advantageous for the treatment of small tumors that are spread over a large area, and complicated tumors to perform surgical operations, for example, tumors in liver cancer [19]. Magnetic hyperthermia using MNP is a therapy in clinical phase for the treatment of glioblastoma multiforme, pancreatic, prostate, breast and esophageal cancer, where the MNPs are introduced either directly into the tumor or into the resection cavity wall, and subsequently, the patient is subjected to an AMF and the particles heat up, destroying the cancer cells [127].

Magnetic nanoparticles present another advantage since it is possible to incorporate drugs in these nanosystems to enable targeted delivery, key aspect that makes this technique a good ally of chemotherapy considering that drug targeting with MNPs should significantly improve drug delivery and consequently, it should cause less damage to normal cells. Taking advantage of this feature, MNPs have been combined with a variety of drugs used in chemotherapy, such as DOX [128], 5-Fluorouracil [129], Bleomycin [130] and Cisplatin [131]. To reach the desired result this technique depends on various parameters, including the drug encapsulation and loading efficiency, magnetic field strength, tumor location, blood flow rate, and vascular supply [14,19].

2.7. 3D IN VITRO MODELS

As the liver is a main targeted organ for substances reaching systemic circulation and plays a central role in metabolism during the detoxification of substances it is important to use suitable liver models for the assessment of drug-induced hepatotoxicity. To perform these studies, human liver hepatocellular carcinoma cell line (HepG2) is currently used for *in vitro* assays since they can be cultured in conventional monolayers or three-dimensional cell cultures [19].

Two-dimensional (2D) cell cultures or monolayer cultures are an important method for studying cellular responses, helping in drug discovery, drug development, pre-clinical *in vitro* assays, and cancer research [1, 5, 6]. It consists in the culture of cells into an adherent flat surface, usually, a petri dish or culture flasks (T flasks), made of polystyrene, in order to provide the necessary mechanical support for the cells [132,133].

Due to the firm advantages associated with these conventional 2D models, which are listed in Table 5, this platform is attractive for *in vitro* studies and, therefore, it is the most used method for cell culture. However, it can result in large discrepancies regarding *in vivo* animal models due to their simplicity and because they are unable to reproduce the real complex microenvironment, structure, and drug resistance present in tumors [132–135].

To address this challenge, efforts are focused on developing 3D models that can better reproduce the particularities of *in vivo* tumors. Taking this into consideration, the development of these new platforms comes to fill the gap between *in vitro* and *in vivo* systems, improving the development of new treatments at the pre-clinical stage [132,133].

The three-dimensional (3D) cell cultures have emerged as a suitable biomodel in the field of cancer research. Advanced 3D models constitute a more representative model of human tumors and offer many advantages over 2D cultures, however, each model has its own advantages and limitations, as seen in Table 5 [132,136]. 3D culture methods can be divided into two main classes: (i) scaffold-based 3D cell cultures, which includes the hydrogels and inserts (reviewed in more detail by Elisabete C. Costa [132]) and (ii) non-scaffold based or scaffold-free 3D cell cultures, where the spheroids and organoids are included [137]. In the first one, the 3D cell cultures are obtained by promoting cell growth, adhesion, and migration

on the artificial 3D platforms that mimic the ECM. Recent research shows how cells have been encapsulated in hydrogels such as gelatin, poly (ethylene glycol) diacrylate (PEGDA), and agarose, which mimic the physicochemical characteristics of native ECM. On the other hand, the ECM of non-scaffold based 3D cell cultures or spheroids are formed by proteins produced by cells during the formation of culture [132,134,138].

2.7.1. Spheroids

3D spheroids are micro-sized cellular aggregates that have emerged as a tool for cancer research to assemble models of different cancer types *in vitro*, such as breast, colon, lung, pancreas, liver, among others [29,132]. Due to the ability of these platforms to more accurately reproduce the cellular microenvironment of solid tumors, when compared to the traditional 2D cell culture, they are a more fitting model for drug testing in oncology [132,133].

Table 5: Comparison of 2D monolayer and 3D spheroid cultures regarding its performance to mimic the TME.


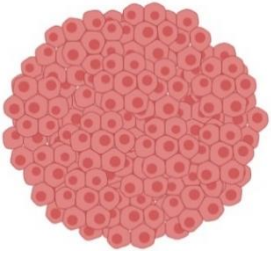
Cell culture types	Advantages	Limitations	ref
2D cell culture <ul style="list-style-type: none"> • Monolayers 	<ul style="list-style-type: none"> • Low cost; • High reproducibility; • Different cell types can be cultured; • Well-stablished; • Simplicity. 	<ul style="list-style-type: none"> • Fails to mimic the 3D structure of tumors; • Unable to reproduce the real complexity of <i>in vivo</i> tumors; • Undetectable expression of ECM proteins; • Poor ECM-cell interactions; • Different gene expression from found in tumors; • Absence of drug penetration barriers and drug resistant. 	[132,134–136]

Table 5: Comparison of 2D monolayer and 3D spheroid cultures regarding its performance to mimic the TME (continuation).

<p>3D cell culture</p> <ul style="list-style-type: none"> • Spheroids 	<ul style="list-style-type: none"> • Low cost for most of the techniques used; • Production of many spheroids under reproducible conditions; • Different cell types can be cultured; • Internal structure with different cell layers like tumors; • Closely mimics the cellular microenvironment: proliferation, heterogeneity, gene expression, growth kinetics, and differentiation; • Deposition of ECM similar with tumor; • Better mimics cell interactions and drug penetration; • Tumor-like conditions such as: hypoxia, nutrition, pH, O₂ and CO₂. 	<ul style="list-style-type: none"> • There are only a few standardized protocols and assays; • Handling care is required to avoid destroying the spheroids during their analysis and manipulation; • Improvements may be needed to create uniform spheroids. • Some techniques to produce spheroids are complex, offer small control over the spheroid diameter, do not yield high number of spheroids and require expensive equipment. <p>[132–136,139,140]</p>
--	---	--

Spheroids can be maintained without vascularization since the tissue architecture permits the penetration of oxygen and nutrients even inside of the spheroid [139]. In particular, spheroids are able to mimic the following particularities (also listed on Table 5):

- (i) **Cellular heterogeneity and cell-cell signaling** since spheroids can be constituted only with cancer cells or with cancer cells cultured with other types of cells, they can better simulate the cellular heterogeneity of real tumors. Besides, as the cells are agglomerated, they can reproduce the physical communication and signaling pathways, promoting an environment resistance against chemotherapy as found in tumors [132].
- (ii) **Internal structure:** as can be seen in Figure 13, both tumors and spheroids have different cell layers. The external layer consists of cells with high rates of proliferation because of its easier access to oxygen and nutrients. The more

internal the cells are located, the more difficult they will be to capture nutrients and oxygen, resulting in hypoxic environments. Under these conditions, cancer cells can convert pyruvate to lactate to get energy. The accumulation of this substance turns the interior of spheroid more acidic (pH 5 -5.5), which also occurs in solid tumor *in vivo* [60,132].

- (iii) **ECM deposition, ECM-cell and cell-cell physical interactions in spheroids:** inside spheroids, cells deposit ECM constituents, such as collagen, laminin, fibronectin, proteoglycans, tenascin, among other components. In addition, the agglomeration of cells in the spheroids provides physical contact between ECM-cell and cell-cell and consequently, form a barrier that makes it difficult for drugs to penetrate and distribute in the tumor mass. On the other hand, the deposition of proteins by cells and their physical interactions increase the density of the spheroid, leading to an increase in the pressure of the interstitial fluid that limits the penetration of drugs by convection [132]. Their spherical shape is also beneficial since it can help in diffusion studies for drugs or toxic chemical penetration [139].
- (iv) **Growth kinetics:** spheroids, as well as solid tumors, have the two main stages of growth. Initially, the volume of the tumor increases exponentially and subsequently, the rate of cell growth begins to decrease until it reaches a constant volume. This growth profile is essential for the layered organization of the spheroids [132].
- (v) **Gene expression profile:** considering that the gene expression is dependent on the 3D cellular organization of the microtissues and that organization is similar to the tumor *in vivo*, the gene expression is also reproducible in the spheroids [132].

There are numerous researches that use HepG2 cell line in different platforms. Elje et al. investigated and compared growth, metabolism, cytotoxicity and genotoxicity between 2D and 3D HepG2 cultures. Elisabeth and co-workers concluded that time and cost-efficient 2D models are usually enough for pre-screening in the field of pharmaceutical drug development and generally have better performance in growth and metabolism. However, in studies that require more complex systems, such as considering drug penetration or cell

interactions/responses, spheroids are more realistic models that significantly better reproduce the *in vivo* microenvironment [141].

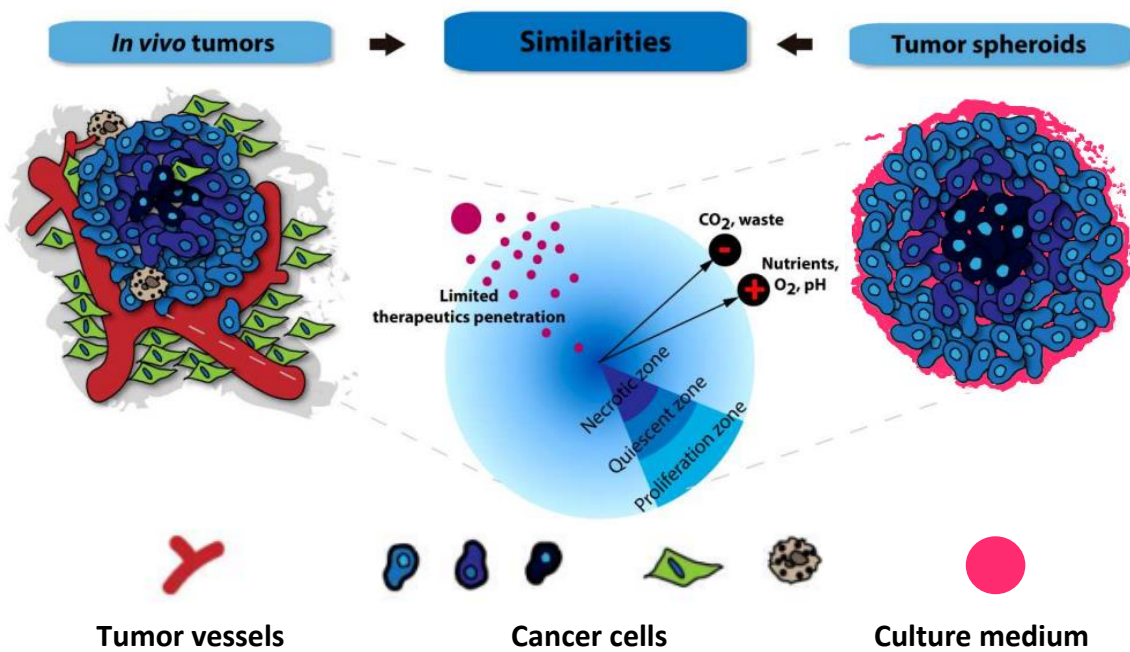


Figure 13: Schematic overview of the physiological similarities between *in vivo* solid tumors and *in vitro* tumor spheroids [142].

2.7.2. Organoids

The overall objective of this work is the *in vitro* preclinical assessment of developed graphene-based magnetic nanoparticles (GbMNPs) as a multifunctional responsive drug delivery system with theranostic performance. With this aim, the use of advanced 3D biological models able to reproduce the complexity of the tumor microenvironment *in vivo* is highly desired in order to obtain relevant information that can be representative of *in vivo* scenarios.

The development of 3D systems enables the creation and growth, *in vitro*, of structures resembling whole organs, termed organoids, able to perform specific organ functions. Organoids have already been developed from mouse and human stem cells to mimic various organs. To date, human pluripotent stem cells have been applied to create intestinal, kidney, pancreas, endometrium, stomach, prostate, ovary, bladder, bone, esophagus, breast, brain,

lung, and retinal organoids, as well as liver [137,143,144]. The term organoid has been applied for a diversity of structures, both *in vitro* and *in vivo*, and simply defined as resembling an organ. However, there are more detailed definitions and an organoid can be defined as a structure derived from pluripotent stem cells or isolated organ progenitors that differentiate to form an organ like tissue exhibiting multiple cell types that are able of self-organize through cell sorting and spatially restricted lineage commitment, similar to the process *in vivo* [143,144]. This technology presents some advantages over the traditional 2D and 3D *in vitro* models, as seen in Figure 14, and provides an effective opportunity to model human organ development in a system similar to development *in vivo*. Organoids present the advantage of better mimicking tumor behavior, which is strongly dependent on environment signals, cell-cell interactions and the extracellular matrix. Regarding this, organoids are embedded in an extracellular matrix gel, such as Matrigel, or different types of collagen, that promotes cell-cell interactions and resemble avascular tumor nodules, or micrometastases, and mimic 3D cell growth kinetics, gradients of nutrient distribution, differentiation, oxygen concentration, and cell proliferation. Furthermore, these advanced 3D models retain the global architecture, morphology, stromal composition, genetic mutations, and heterogeneity of the original tumor [137,144,145].

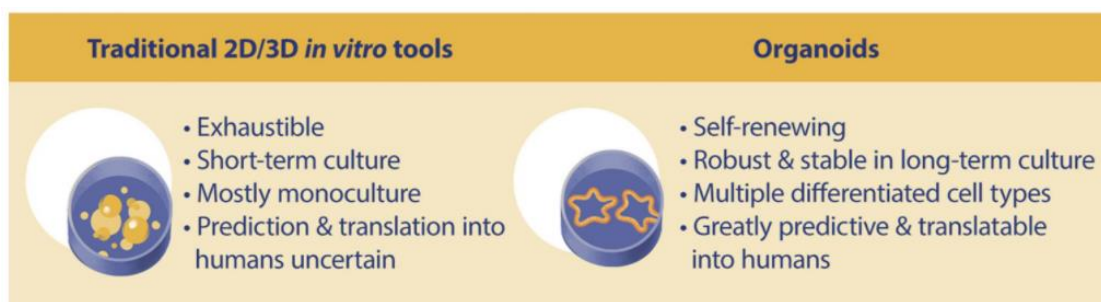


Figure 14: Comparison between organoids and standard 2D and 3D *in vitro* models [146].

Moreover, organoids can be used as an alternative drug testing system with great benefits such as the ability to better recapitulate the effects in human patients and reduce the animal studies. Among the different types of organoids, liver organoids represent a model with high potential, mainly for drug testing because of the unique metabolic profile of the human liver [1,3].

3. MATERIALS AND METHODS

3.1. CHEMICALS

Gelatin methacryloyl (GelMA), dimethyl sulfoxide (99.9%) 2-hydroxy-4'-(2-hydroxyethoxy)-2-methylpropiophenone (PI)(98%), phosphate buffered saline (PBS) pH 7.4, and absolute ethanol were purchased from Sigma-Aldrich. CyQUANT LDH Cytotoxicity Assay Kit was purchased from ThermoFisher Scientific. Dialysis Membrane Standard RC Tubing (molecular weight cut-off 3.5 kDa, nominal flat width 45 mm) was purchased from Spectra/Por®. Human Transferrin ELISA Kit (ab187391) and Human Serum Albumin ELISA kit (ab179887) were purchased from Abcam. AquaBluer Solution (MultiTarget Pharmaceuticals, LLC), Doxorubicin (Adooq Bioscience). RPMI 1640 medium, hank's balanced salt solution (HBSS), fetal bovine serum (FBS), L-glutamine, trypsin-EDTA and penicillin/streptomycin solution were purchased from Gibco Invitrogen Life Technologies (Carlsbad, CA, USA). All aqueous solutions were prepared using ultrapure water (18.2 MΩ.cm at 25 °C), produced in a Milli-Q system (Millipore).

3.2. SYNTHESIS OF GbMNPS

Graphene-based yolk-shell magnetic nanoparticles were synthesized and resuspended in ultrapure water (2 mg mL⁻¹) by the Polytechnic Institute of Bragança and sent to the International Iberian Nanotechnology Laboratory (INL, Braga). The yolk-shell graphene-based MNPs were synthesized through the procedure described by Rodrigues et al. [147]. The main steps of the synthesis of GbMNPs are illustrate in Figure 15.

Briefly, the superparamagnetic magnetite (Fe₃O₄) core was synthesized using a wet chemistry protocol based on the co-precipitation of Fe²⁺ and Fe³⁺ (1:2) under magnetic stirring at 55 °C in a basic solution of ammonium hydroxide. Subsequently, the graphene-based shell was accomplished via a one-pot strategy of hydrolysis and polymerisation of the precursor's resorcinol, formaldehyde and TEOS. Followed by thermal annealing and silica etching, the

colloidal stabilization of the GbMNPs was ensured by chemical functionalization by an acid treatment at mild conditions with the copolymer Pluronic F-127 [147].

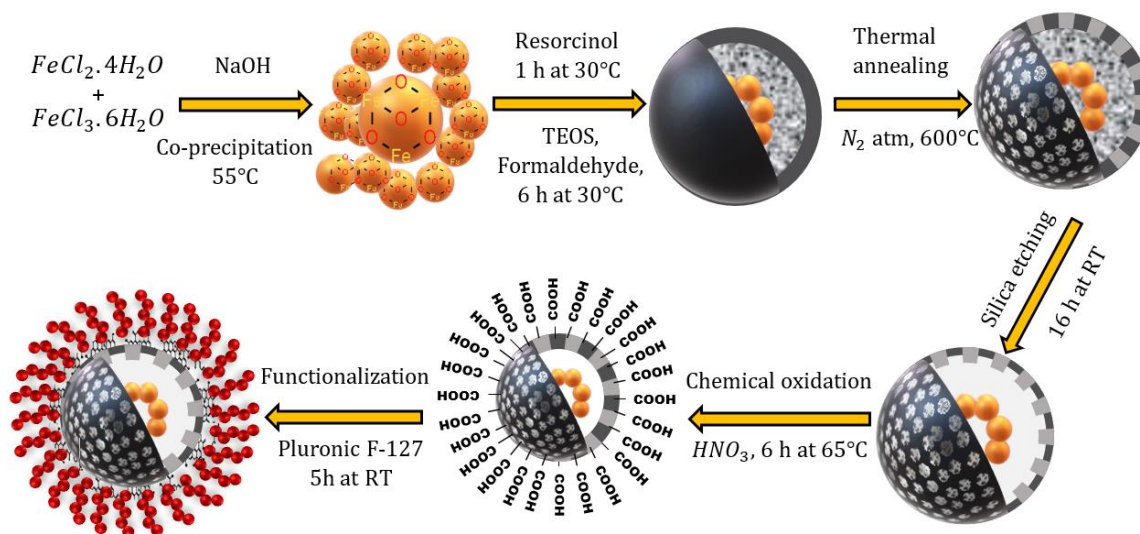


Figure 15: Schematic representation of the GbMNPs synthesis route.

3.2.1. Hydrophilization of GbMNPs

Chemical functionalization of the graphene-based shell was performed in order to assure the colloidal stabilization in aqueous solutions. The nanoparticles were functionalized with the copolymer Pluronic F127 (40 mg mL^{-1}) for 5h in magnetic stirring, at room temperature.

The copolymer Pluronic F-127 (PF127) was used in order to improve colloidal stabilization and biocompatibility of GbMNPs. The resulting solution (GbMNP@PF127) was then washed by centrifugation (13,000 rpm, 20 min) with mili-Q water to remove unbounded copolymer, and the final pellet was resuspended in ultrapure water.

One of the amphiphilic block copolymers extensively studied in drug delivery is PF127. PF127 is water soluble, biocompatible, and consists of an amphiphilic triblock copolymer with hydrophilic poly (ethylene oxide) (PEO) blocks and hydrophobic poly (propylene oxide) (PPO) blocks arranged as PEO-PPO-PEO, and it is approved by the FDA for clinical use [148].

3.2.2. Purification procedure

The synthesized and functionalized nanoparticles are subsequently centrifuged at 4000 rpm for 45 min. After centrifugation the sediment, that contained the largest nanoparticles, was discarded, and the supernatant was stored as ready-to-use purified nanoparticles.

3.3. PHYSICOCHEMICAL CHARACTERIZATION OF GbMNPs

The main physicochemical and functional properties of GbMNP@PF127 were previously optimized in order them to act as multifunctional theranostic nanosystems, namely as drug carrier, heat nanosource in magnetic hyperthermia and MRI contrast agent. Their main characterization results, including TEM and SEM pictures, magnetic heating curves, and room temperature hysteresis loop, are presented in Annex I. Nevertheless, a basic physicochemical workflow was followed in order to confirm the batch-to-batch reproducibility of the samples used in this work. The next step was the *in vitro* preclinical functional validation and the use of both 2D and 3D biological models. In this section, relevant equipment and characterization methodologies used in this work are described in detail, which refer to the physicochemical properties and the *in vitro* preclinical functional (theranostic) validation of the developed agents using both 2D (tumor cell lines) and 3D (liver-tumor organoid) biological models.

3.3.1. Inductively coupled plasma-optical emission spectroscopy

Inductively coupled plasma optical emission spectrometry (ICP-OES) is a powerful analytical technology for the quantification of trace elements in a diversity of different sample matrices (down to 10 ng L⁻¹ for some selected elements) in liquid solutions [149,150]. ICP-OES has a higher atomization temperature in comparison with other ionization/excitation sources, a more inert environment, improved detection limits, high precision, less background signal, and it can provide simultaneous determinations for up to 70 elements [149–151]. This

technique is an atomic emission spectroscopy with an atomization and excitation source that consists of an inductively coupled plasma torch. The plasma has enough energy to promote the excitation of most of the chemical elements, allowing the quantification of a wide range of analytes [149,150].

The fundamental principle of atomic emission spectroscopy is the property of atoms to emit electromagnetic radiation when subjected to specific conditions. Liquid samples are injected into a radiofrequency-induced argon plasma, and the sample solution is converted to an aerosol and directed into the central channel of the plasma, which maintain a high atomization temperature of approximately 10 000K, so the aerosol is quickly vaporized [149]. Free atoms from the analyte elements are released in the gaseous state and enough energy is able to convert the atoms to ions, promoting them to excited states. Both the atomic and ionic excited state species may return to their ground state by the emission of photons. These photons have characteristic energies that are determined by the energy level for each type of atom or ion. Consequently, the specific wavelength of the photons can be used to identify different elements and the total number of photons is directly proportional to the concentration of the element in the sample [149,150].

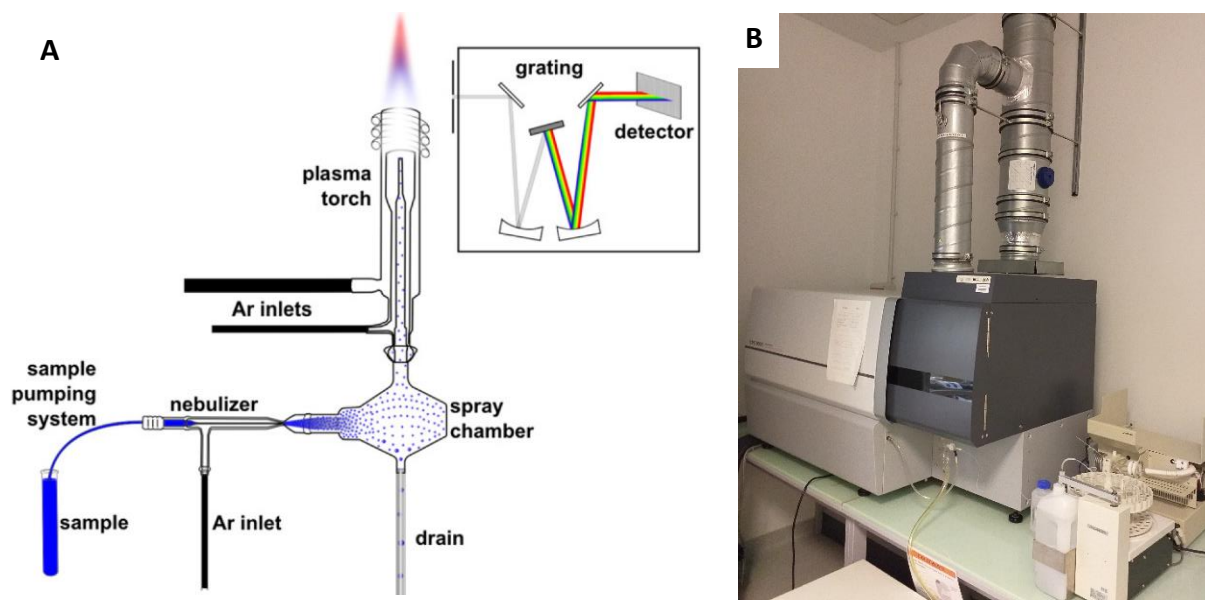


Figure 16: (A) Diagram of a typical ICP-OES instrument with radial configuration of the detection system [150] and (B) picture of the ICPE-9000 Multitype ICP Emission Spectrometer used in this work.

The Fe concentration was used as the concentration indicator of the GbMNP@PF127 nanoparticles in solution. Thus, Fe quantification was performed by ICP-OES in a ICPE-9000

Multitype ICP Emission Spectrometer, Shimadzu (Figure 16). The samples were prepared by digesting 100 μL of the GbMNP@PF127 solution in 1 mL of HCl (37%) overnight in order to remove all organic mass and dissolve all the Fe atoms from the sample. Thereafter, the samples were diluted with mili-Q water up to 10 mL. The Fe wavelength selected for detection was 235.5 nm. The measurements were repeated three times and the results were represented as the mean value with relative standard deviation. The calibration solutions (standard solutions purchased from Sigma-Aldrich) were adjusted to ensure that they covered the whole range of concentrations measured in this study.

3.3.2. Dynamic light scattering

Dynamic light scattering (DLS) is one of the most versatile, simple and useful technique to analyze the hydrodynamic diameter and zeta potential of nanoparticles in aqueous solution. The sample is exposed to a monochromatic wave of light where part of the light will be scattered, and a detector, which is located at a particular angle with respect to the outgoing light beam (usually 90° or 173°), collects the signal for further analysis in terms of its intensity, as illustrated in Figure 17 [152–154].

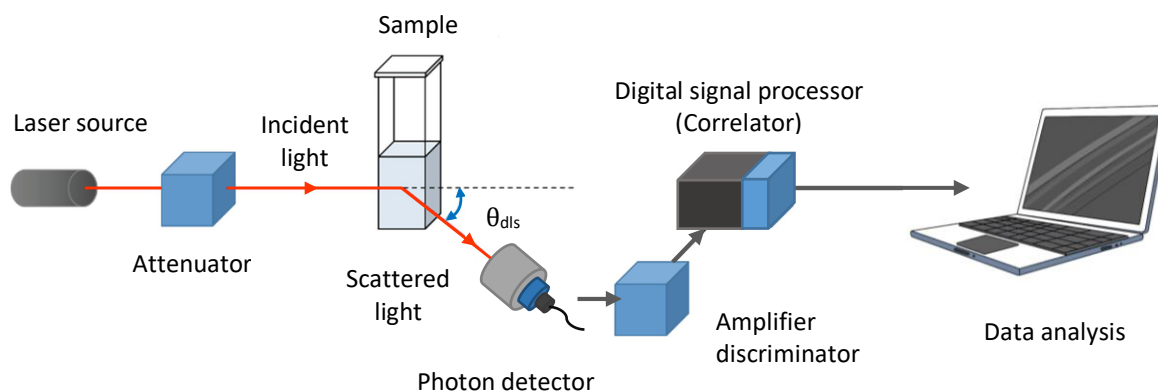


Figure 17: Optical configuration of a typical experimental setup for dynamic light scattering measurement [154].

All DLS measurements including average particle size and zeta potential were performed in a SZ-100 equipment from Horiba Scientific (Figure 18) with nanometric resolution (from 0.3 nm to 8 μm) and operated at a scattering angle of 173° . For all

measurements an electrode cell was used with 1 mL of sample. The concentration of the GbMNP@PF127 was set at 0.1 mg mL⁻¹ in Milli-Q water at room temperature. For each sample at least 3 measurements were performed.

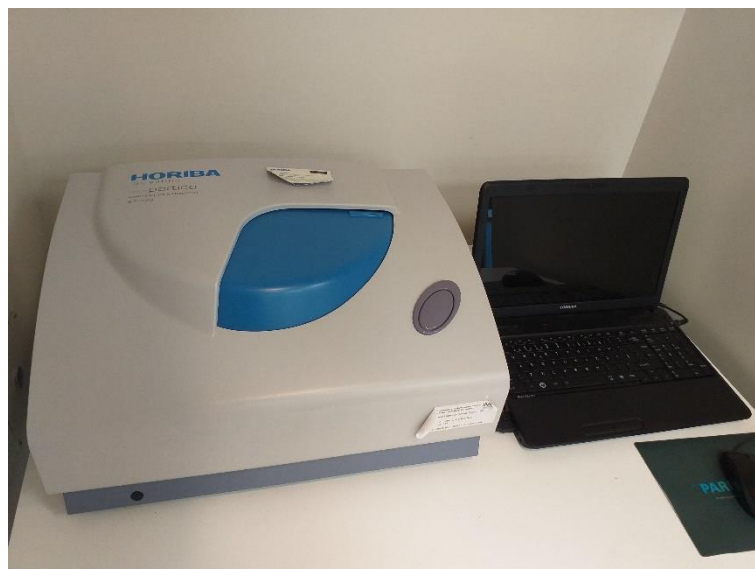


Figure 18: Picture of the Nano Particle Analyzer Z-100 equipment used to measure the hydrodynamic diameter and zeta potential of the samples.

3.3.2.1. Hydrodynamic diameter

Since MNPs are in constant random motion, known as Brownian motion, due to their kinetic energy, the detected scattered light has fluctuations. These variations of the intensity represent the time it takes a particle to move a significant fraction of the wavelength of light, where the speed of a particle depends on its size. The fluctuations contain information on that random motion (Brownian motion) and can be used to measure the diffusion coefficient of the particles from the correlation of the scattering intensity [153,155–157]. Therefore, the hydrodynamic diameter of the nanoparticle can be calculated from its diffusion coefficient D by the Stokes-Einstein equation [3,4]:

$$D = \frac{K_B T}{3\pi\eta d_H} \quad \text{Equation (6)}$$

Where, K_B is the universal Boltzmann constant, T is the absolute temperature, η is the dynamic viscosity of the surrounding media, and d_H is the hydrodynamic diameter of the nanoparticles [155,156]. Hydrodynamic diameter is the size of a sphere that has the same diffusion coefficient within the same viscous environment, and it is directly related to the diffusive motion of the particles [155,156].

3.3.2.2. Zeta potential

Zeta potential is an indirect method that provides valuable information regarding the dispersion and aggregation of nanoparticles, affecting the stability of their colloidal suspensions, through the measurement of their surface charge [157–160]. This behavior is attributed to the electrostatic repulsion between particles with the same electric charge [160,161]. The measurement of the zeta potential is taken by applying an electric charge through the sample in a cell that contains two gold electrodes. When a voltage is applied to the electrode, the particles will be attracted to the electrode with the opposite charge. The velocity will be proportional to the degree of Zeta potential and is measured by Doppler technique, which analyzes both speed and direction of particles as a function of voltage [162,163]. The electrostatic stabilization is achieved as a result of the formation of an electrical double layer arising from the charged ions absorbed on the surface of the particles. The electrical double layer can be divided into two regions: an inner region, where the surface of a charged particle attracts a layer of opposite charge and bonds strongly to it, resulting in a thin liquid layer termed Stern layer and an outer region, termed diffuse layer, where the ions are less strongly associated [159,163,164]. In the diffuse layer, there is a hypothetical limit, named slipping plane, within which ions and particles form a stable entity. Therefore, the value of the electrostatic potential on the imaginary slipping plane is the zeta potential (Figure 19) [165].

When an electrical field is applied across the samples the movement of the nanoparticles (electrophoretic mobility) is measured according to Henry's equation [165]:

$$U_e = \frac{2\varepsilon\zeta f(ka)}{3\eta} \quad \text{Equation (7)}$$

Where, U_e is the electrophoretic mobility ($m^2 s^{-1} V^{-1}$), ζ is the zeta-potential (V), ε is the solvent dielectric permittivity (or constant) ($kg m V^{-2} s^{-2}$), η is the viscosity ($kg m^{-1} s^{-1}$), and $f(ka)$ is Henry's function (dimensionless), and ka is a measurement according to the ratio of the particle size to the Debye length [165].

Zeta potential values $\zeta > |30|$ are usually considered colloidally stable due to charge stabilization, that is, the electrostatic repulsive forces are high enough to prevent aggregation. Thus, particles of similar charge will have a lower propensity to agglomerate as their absolute zeta potential increases [164,165].

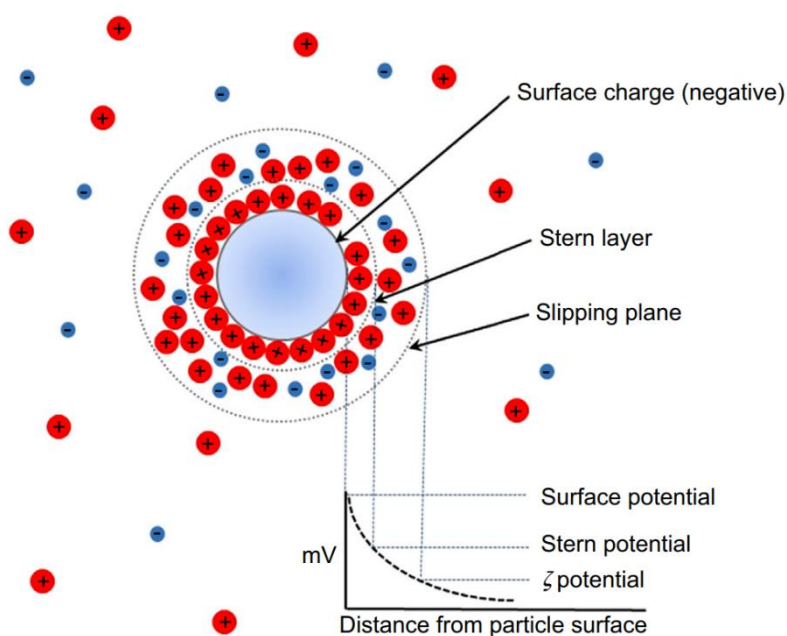


Figure 19: Scheme of the electrical double layer that surrounds a particle in an aqueous medium. The zeta potential is the electrical potential at the slipping plane [164].

3.3.3. Magnetic hyperthermia

The basic concepts of heat induction in MNPs magnetic nanoparticles under an AMF were discussed in chapter 2. In this section an overview of this technique will be addressed.

In the last years, the use of MNPs for MH and thermoablation has attracted growing attention for application in cancer therapy [19]. In this technique the heating is supplied by

the oscillations of the MNPs (nanoheaters) induced by an external AMF, with specific amplitude and frequency [16]. Besides these parameters, the effectiveness of this method depends on several other factors, rate of blood flow and vascular supply, and depends on magnetic, colloidal and structural properties of the nanoheaters. Combining with other therapeutic approaches, such as chemotherapy or radiotherapy, can improve the therapeutic index of MH [14].

Frequency and the amplitude of the external AMF can be directly selected in the MH equipment within available ranges. However, it is important to take into careful consideration for this selection the Berkovitz criterion, which specifies the upper limit for the product of the magnetic field strength and frequency that can be applied to the human body in order to avoid undesirable heating. This criterion can be represented by the following equation [17,166]:

$$H \times f < 4.85 \times 10^8 \text{ Am}^{-1} \text{ s}^{-1} \quad \text{Equation (8)}$$

Where H is the magnetic field amplitude and f is the frequency of the AMF. This criterion presumes that the product of amplitude of field and frequency used in the clinical setting should not exceed that value ($4.85 \times 10^8 \text{ Am}^{-1} \text{ s}^{-1}$) [17,88,166].

In most cases, the samples are placed in the mid-point inside a helical water-cooled induction coil, where the maximum amplitude of the AMF is achieved (Figure 20A). Then an alternating current flow through the induction coil and a function generator generates a square wave function at a selected frequency. Due to large currents running through the coils, they should be equipped with efficient water-cooling systems in order to prevent overheating the copper coils. Besides, the geometry of the coil strongly affects the distribution and the intensity of the magnetic field generated. This equipment is also composed of a temperature sensor (normally an optical fiber) that is connected to a computer and it is used to record the temperature increase as a function of time [19,167].

In this work, two different magnetic hyperthermia equipment were used to create an alternating magnetic field around the GbMNPs in order to prove heating. A commercial alternating current field applicator from nanoTherics, NAN201003 Magnetherm (Figure 20B) was used to evaluate the release profile of the encapsulated drug. Therefore, treatment

comparisons were performed with and without hyperthermia by using a series of samples and controls, as it will be explained later. The second equipment used was the NAN201007 Live Cell Exposure accessory from nanoTherics (Figure 20C), dedicated for *in vitro* studies thanks to a radiofrequency extensible accessory that allows to fit the cell culture plates inside the equipment, maintaining the appropriate culture conditions of the cells.

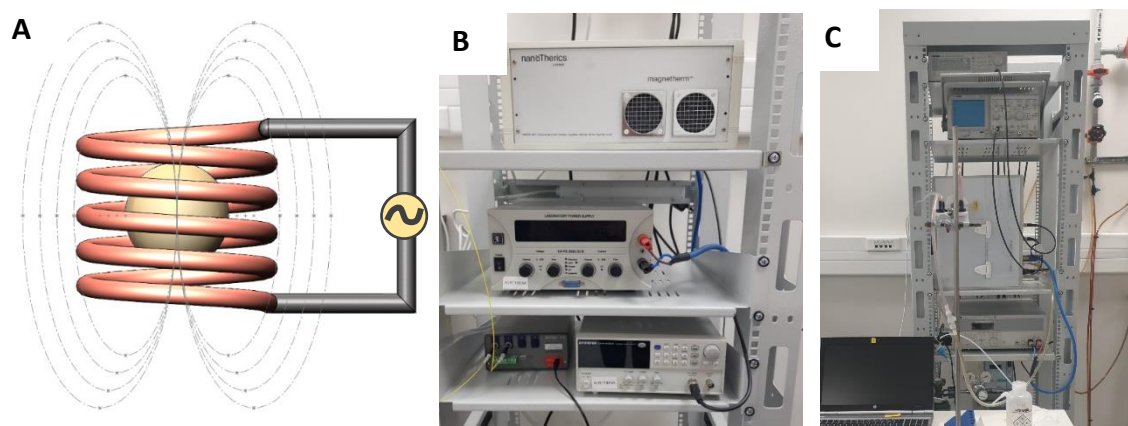


Figure 20: Schematic representation of a MH setup. (A) Inside the coil a magnetic nanoparticle is represented drawn in SolidWorks software; (B) commercial alternating current field applicator from nanoTherics, NAN201003 Magnetherm; and (C) NAN201007 Live Cell Exposure accessory from nanoTherics.

3.3.4. MRI

The basic principles of MRI were generally discussed in chapter 2. In this section a more detailed description of the equipment will be provided.

Hydrogen is the molecular mediator used for MRI clinical applications due to its abundance and distribution in the human body. Each hydrogen is composed of a proton that acts like small magnets with a magnetic spin. When an external magnetic field is not applied, all the hydrogen nuclei point in different directions, so there is no general orientation of total magnetization from the sum of all directions. In this case, there would be no signal to detect. On the other hand, when a strong magnetic field is applied, the magnetic moments of the nuclei tend to align themselves in the same direction (along the direction of the applied magnetic field). MRI experiments are performed in a MRI scanner such as that represented in Figure 21.

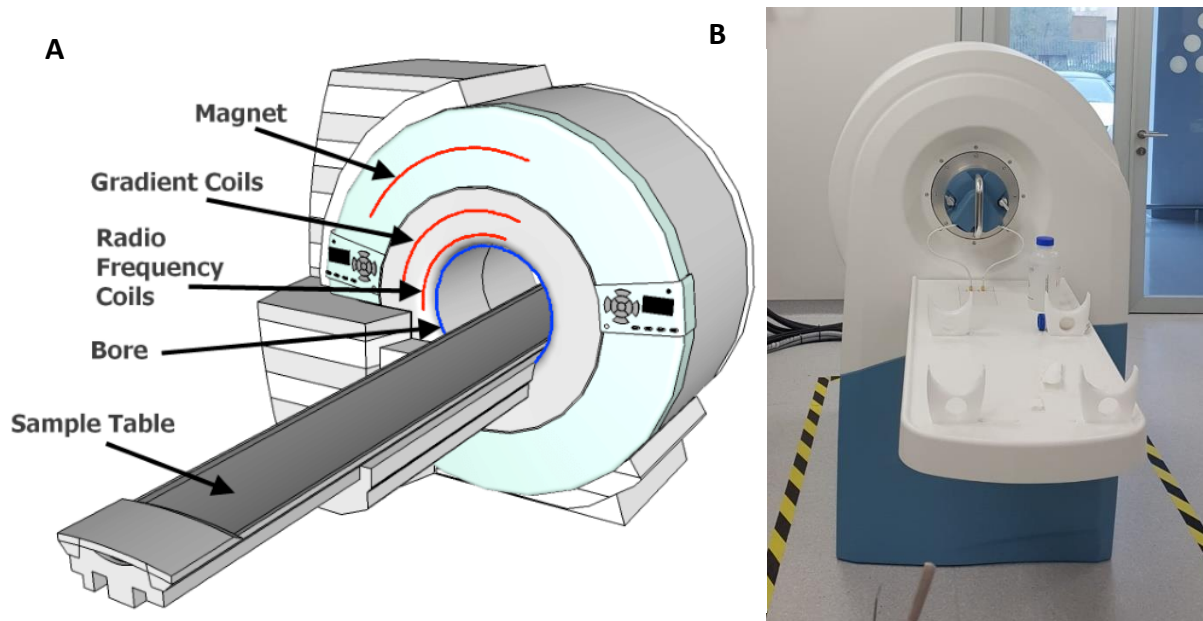


Figure 21: (A) Schematic representation of a MRI scanner (Adapted from [168]) and (B) a 3T-MRI Solutions Benchtop Scanner (Guildford, UK) used in this work.

Briefly, the sample is placed inside the scanner bore, where a superconducting magnet creates a stable, strong and high temporal stability uniform external magnetic field that causes the hydrogen molecules to align in the same direction as B_0 . Then, an electromagnetic field is switched on and off by a set of gradient coils, at an appropriate resonance frequency, causing each hydrogen atom to alter their alignment and quickly switch back to their original relaxed state every time the magnetic field is switched off. The set of gradient coils that change the field along the x, y and z directions allows the localization of image slices, as well as the encoding of the position information to create and MR image. A radiofrequency magnetic field is generated by a radio frequency coil mounted inside the gradient coil. The gradient coils disturb the main field, causing the resonance frequency of protons to vary in function of their position. The radio frequency coils excite the sample and detect the resulting signal coming from the excited atoms. This detected signal is then transformed by Fourier Transform, amplified and presented in a computer. In this equipment the images can be acquired with different sets of pulse sequences and gradients that will result in a different image appearance.

In particular in this work, MR images were acquired in a preclinical MR Solutions Benchtop Scanner (Guildford, UK) working at clinical field strength of 3T at room temperature

(Figure 21B). This equipment was used to evaluate the capability of GbMNP@PF17 to act as T_2 -contrast agents in MRI and study their cell internalization by HepG2 cells through MRI. For the measurements of the samples, 200 μL of GBMNP@PF127 at different concentrations in Milli-Q water were placed into a custom printed MRI holder. Then the holder was positioned in the center of the MRI scanner bore (sample table as shown in Figure 21A). Afterwards, T_2 weighted images and a ratiometric T_2 -map were acquired using a multi-echo-multi-slice (MEMS) sequence. Subsequently, the transverse relaxivity (r_2), a parameter that measures the efficiency of a certain compound to act as contrast agent and which represents the inverse of the amount of contrast agent needed to reduce water protons relaxation time by 1 s, was calculated. ImageJ software was used to reconstruct the maps using the “MRI analysis calculator” plugin, and to determinate the relaxation time for each sample concentration.

3.3.5. High performance liquid chromatography

High performance liquid chromatography (HPLC) is an advanced technique of column liquid chromatography widely used in analytical chemistry, to separate and analyze compounds in a mixture. In the HPLC, an injector is used to introduce the sample, then the sample mixture or analyte in a solvent (mobile phase) is pumped at high pressure (50 - 350 bar) through a column at various speeds with a controlled flux (Figure 22) [169]. The velocity of each component depends on the mobile phase composition, whereas that high pressure is essential for pushing the mobile phase through the column. This allows a faster and more efficient analysis [170,171]. The column is filled with very small particles (stationary phase) that gives a very large surface area for the sample molecules to interact. The analytes have different interactions with the mobile and stationary phase, resulting in a different retention time. The analytes that have stronger interactions with the stationary phase will move slower than the analytes that have weaker or no interactions. The analytes are detected using a specific detector that monitors the eluent as it comes off the column. After, a data recording system provides a chromatogram based on the analog data [169,172].

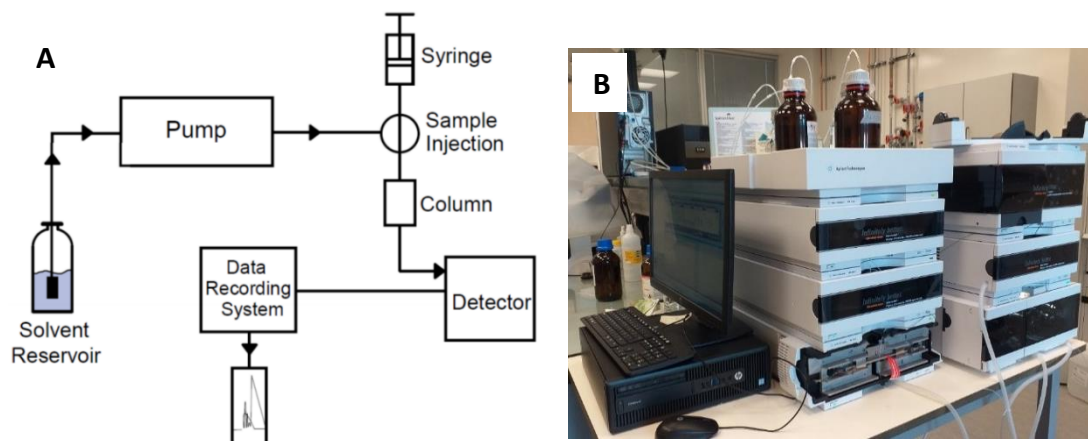


Figure 22: (A) HPLC system configuration [173]; (B) Picture of the UHPLC Agilent 1290 Infinity II LC System used in this work.

The HPLC equipment was used to analyze the DOX content of supernatants and collected samples during drug release experiments in order to study drug loading, drug capacity and the drug delivery profile, as described below.

3.3.6. Drug loading / capacity studies

In this study, DOX was encapsulated into the GbMNP@PF127 nanoparticles. Drug loading experiments were carried out by mixing DOX (dissolved in Mili-Q water) with GbMNP@PF127 at a ratio of 1:1 ($100 \mu\text{g mL}^{-1}$) in a phosphate buffer solution (PBS) with pH 7.4. The suspensions were kept in a thermomixer at $37 \text{ }^\circ\text{C}$ during 48 h in darkness. Afterwards the suspension was centrifuged at 1400 rpm for 30 m and the pellet, containing GbMNP@PF127 loaded with DOX (GbMNP@PF127@DOX), was subsequently used for the drug release and other experiments described below, and the supernatant, containing the free DOX, was used to determine the amount of drug that was encapsulated.

The drug loading efficiency (DLE) was calculated using the following equation:

$$DLE (\%) = \frac{W_{loaded}}{W_{initial}} \times 100 \quad \text{Equation (9)}$$

Where W_{loaded} represents the amount (in weight) of DOX loaded into the nanoparticles and $W_{initial}$ is the amount of DOX initially mixed with the nanoparticles for loading. W_{loaded} can be calculated using the Equation 10:

$$W_{loaded} = W_{initial} - W_{free\ dox} \quad \text{Equation (10)}$$

Where $W_{free\ dox}$ represents the free DOX obtained from the supernatant after centrifugation. The amount of free DOX in the supernatant was determined chromatographically using high performance liquid chromatography (HPLC - 1260 Infinity II LC System, Agilent).

The drug loading capacity (DLC) was calculated using the following equation:

$$DLC (\mu g\ mg^{-1}) = \frac{W_{loaded}}{W_{GbMNP_s}} \quad \text{Equation (11)}$$

Where W_{GbMNP_s} represents the amount of nanoparticles mixed in solution with DOX.

3.3.7. DOX release and kinetics analysis

The pH dependent drug release of DOX was evaluated on DOX-loaded GbMNP@PF127. For this purpose, 33 μg of GbMNP@PF127@DOX were resuspended in phosphate buffer solution (200 μL) at physiological (pH 7.4) and acidic (pH 5 and 6.5) pHs and placed in a customized setup composed by a cylinder with a dialysis membrane (MWCO: 3.5 kDa) at the base of the cylinder at room temperature, as shown in Figure 23. The cylinder was then placed under 10 mL of Mili-Q water and at selected time intervals, 500 μL of the dialysate were collected, whereas another 500 μL of fresh ultrapure water were added to maintain the total volume constant. In order to evaluate the effect of magnetic hyperthermia on the drug delivery profile, the same experiments were performed under an AMF. In these experiments, an external AMF of 20 mT and 285.4 kHz was performed for 4h in the NAN201003 Magnetherm equipment from Nanotherics. In all the cases, the DOX concentration in the collected samples was determined by HPLC and plotted against the time.

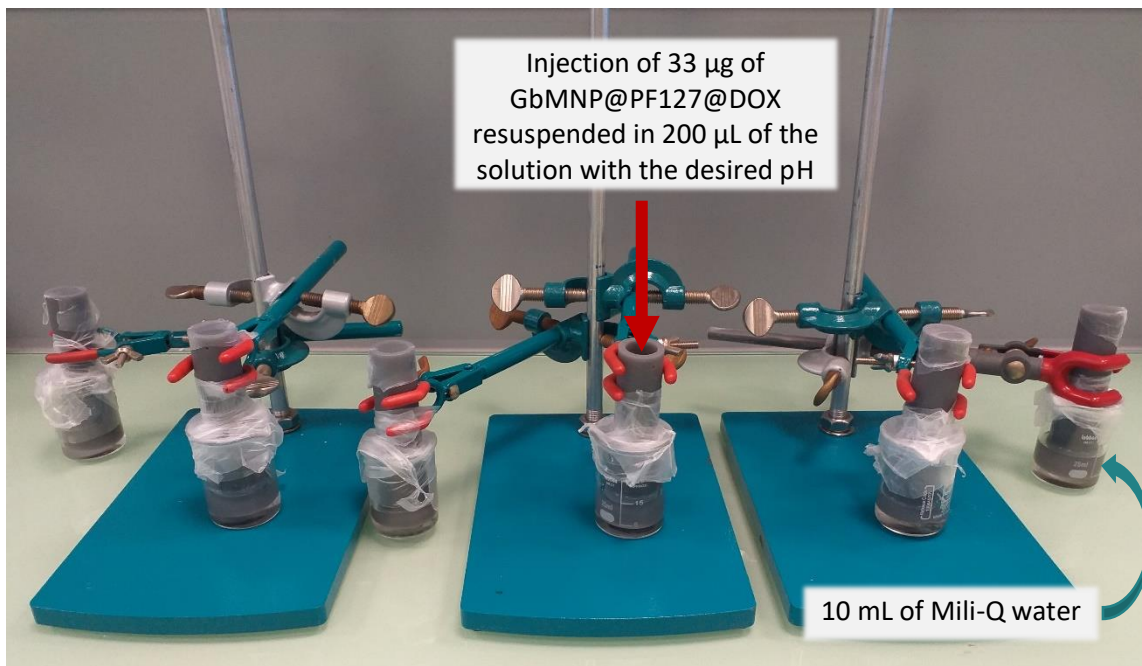


Figure 23: Picture of the drug release multi-point set up.

For the DOX release kinetics analysis, the obtained release profiles (cumulative DOX amount vs time) were analyzed with zero-order, first-order, Higuchi, Hixon-Crowell and Korsmeyer-Peppas models. Experimental data were analyzed by a linear regression based on the least-squares regression method, using the DDSolver Excel extension. Thereby, the kinetic model that best fitted the drug release data was selected by calculating and comparing the respective regression coefficients (R^2) of the different models and the respective Akaike Information Criterion (AIC) represented in Equation 12 [120,174]:

$$AIC = N (\ln SSR) + 2p \quad \text{Equation (12)}$$

Where, N is the number of experimental data points, SSR is the square residuals sum and the p is the number of parameters in the model [174].

Zero-order model consists in drug dissolution from dosage forms that do not disaggregate and release the drug at a constant rate for a certain period of time, and are desirable in order to minimize drug concentration variations, resulting in a very slow drug release with no changes in the equilibrium conditions. The dissolution of the drug can be described as [175,176]:

$$Q_t = Q_0 + K_0 t \quad \text{Equation (13)}$$

Where Q_t is the amount of drug dissolved in time t , Q_0 is the initial amount of drug in the solution, K_0 is the zero-order release constant expressed in units of concentration/time [176,177].

First order model has been used to describe absorption and/or elimination of a diversity of drugs. This model describes that a change in concentration during a period of time is dependent only on drug concentration and can be represented by the follow equation [175,176]:

$$\log Q_t = \log Q_0 + \frac{K_1 t}{2.303} \quad \text{Equation (14)}$$

Where, K_1 is the first-order rate constant expressed in time units [175].

Higuchi model describes the release of water soluble and low soluble drugs incorporated in semisolid or solid matrices. This model states that the release of a drug from a drug delivery system involves both dissolution and diffusion. Simplified Higuchi model describes the drug release as a square root of time dependent process based on release by diffusion. The model expression is given by the equation [177,178]:

$$Q_t = K_H \sqrt{t} \quad \text{Equation (15)}$$

Where, K_H is the Higuchi dissolution constant [177,178].

Another mathematical model, created by Hixon and Crowell, represents dissolution rate that is normalized for the decrease in solid surface area as a function of time. The model describes the release from systems where there is a change in the surface area and diameter of particles according to the equation [176,178]:

$$\sqrt[3]{Q_0} - \sqrt[3]{Q_t} = K_{HC} t \quad \text{Equation (16)}$$

Where, K_{HC} is the constant incorporating the surface-volume relation. This equation applies to pharmaceutical dosage form such as tablets, where the dissolution occurs in planes

that are parallel to the surface of the dosage form if the tablet dimensions decrease proportionally, in such a manner that the initial geometrical form keeps constant [175,176,178].

The last model, Korsmeyer-Peppas, is used to describe drug release over time from a polymeric system by using the n (release exponent) value. The equation can be represented as [178,179]:

$$Q_t = \frac{Q_t}{Q_\infty} = K_m t^n \quad \text{Equation (17)}$$

Where, $\frac{Q_t}{Q_\infty}$ is the fraction of drug released at time t ; K_m is the release rate constant incorporating structural and geometric characteristics of the delivery system and n is the release exponent that indicates the mechanism of transport of drug [176–178]. In this model, the n value characterizes the different mechanisms of drug release from their matrix, as described in Table 6.

Table 6: Interpretation of release mechanisms from cylinder polymeric matrices [120,175,178].

Drug transport mechanism	Release exponent (n)
Quasi-Fickian diffusion	$n > 0.45$
Fickian diffusion	0.45
Anomalous diffusion	$0.45 < n < 0.89$
Non-Fickian case II transport	0.89
Non-Fickian super case II transport	$n > 0.89$

In the Fickian diffusion the release occurs by the usual diffusion of the drug due to a chemical potential gradient. In the anomalous or non-Fickian diffusion the mechanism of drug release is regulated by diffusion and swelling. Regarding the non-Fickian case and super case II transport the drug release rate corresponds to zero-order release kinetics and the mechanism that promotes the release involves the swelling or relaxation of polymeric chains, where the non-Fickian super case II transport represents an extreme case of transport [175,178].

Table 7 presents a summary of mathematical models used to describe drug release kinetics.

Table 7: Summary of mathematical models used to describe drug release profiles.

Mathematical Models	Equations	Parameters	References
Zero-order	$Q_t = Q_0 + K_0t$	K_0	2, 5
First-order	$\log Q_t = \log Q_0 + \frac{K_1t}{2.303}$	K_1	1, 3
Higuchi	$Q_t = K_H\sqrt{t}$	K_H	3, 2
Hixon-Crowell	$\sqrt[3]{Q_0} - \sqrt[3]{Q_t} = K_{HC}t$	K_{HC}	1, 2
Korsmeyer-Peppas	$Q_t = \frac{Q_t}{Q_\infty} = K_m t^n$	K_m, n	4,5

3.4. PREPARATION OF 3D LIVER-TUMOR ORGANOIDS

3.4.1. Cell cultures

The adherent Human liver hepatocellular carcinoma HepG2 cell line (ATCC HB-8065 – American type culture collection, Virginia, USA) was selected for cell viability studies because of its well-established physiology, easy maintenance, and practical use for drug screening [139]. The HepG2 cell line was acquired from Centro de Investigação de Montanha (CIMO) (Figure 24) and maintained in T75 culture flasks at an initial density of 10^5 cells per cm^2 in Roswell Park Memorial Institute (RPMI) 1640 Medium with GlutaMAX™ supplemented with 10% fetal bovine serum (FBS), 1% Penicillin-Streptomycin and 1% of HyClone™ Non-Essential Amino Acids in a humidified incubator at 37 °C with 5% of CO_2 environment. Sub-culturing was done by trypsinization after every 80% confluence. To determine the number of viable cells, Trypan blue exclusion method and a Neubauer chamber were used. The cell suspension was diluted in Trypan blue in a 1:1 ratio.

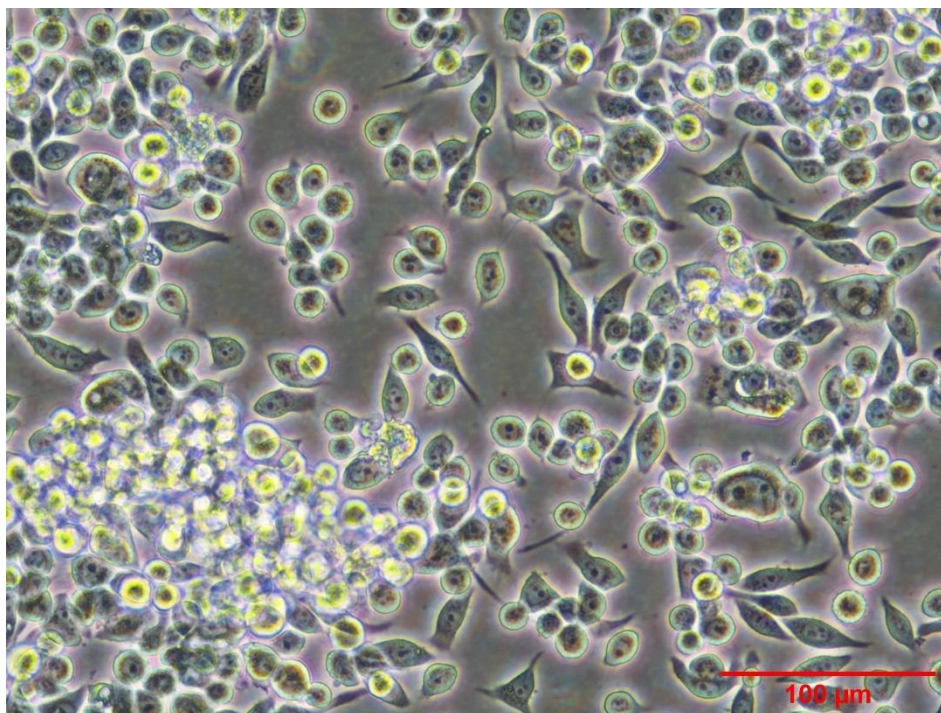


Figure 24: Optical microscope image of the HepG2 cells in culture.

3.4.2. Preparation of HepG2-derived organoids

Although 2D monolayer cell cultures have many advantages, they are unable to reproduce the real complex microenvironment and as a result, these cultures commonly do not reproduce the mechanisms of nanoparticle - cell/host interactions. To overcome this challenge 3D *in vitro* models have recently emerged, which can better reproduce the particularities of *in vivo* tumors and are highly similar to human organs and tissues [132–135].

The 3D models used in this work were HepG2-derived organoids. In order to produce the organoids, it was necessary to proceed with the formation of spheroids. **HepG2-derived spheroids** were obtained from HepG2 cells in culture. Once the culture flask reached 60-70% confluence, medium from the flask was aspirated, the cells washed twice with 1xPBS and dissociated using 2-3 mL of trypsin. After being incubated for five minutes, the trypsin was neutralized with 4 mL of RPMI-1640, and live cells were counted using Trypan Blue Solution. Cells were seeded under non-adherent conditions, using custom-made polydimethylsiloxane (PDMS) multi-microwells molds synthesized by the University of Minho at a concentration of 4×10^6 cells mL⁻¹ per PDMS mold (Figure 25).

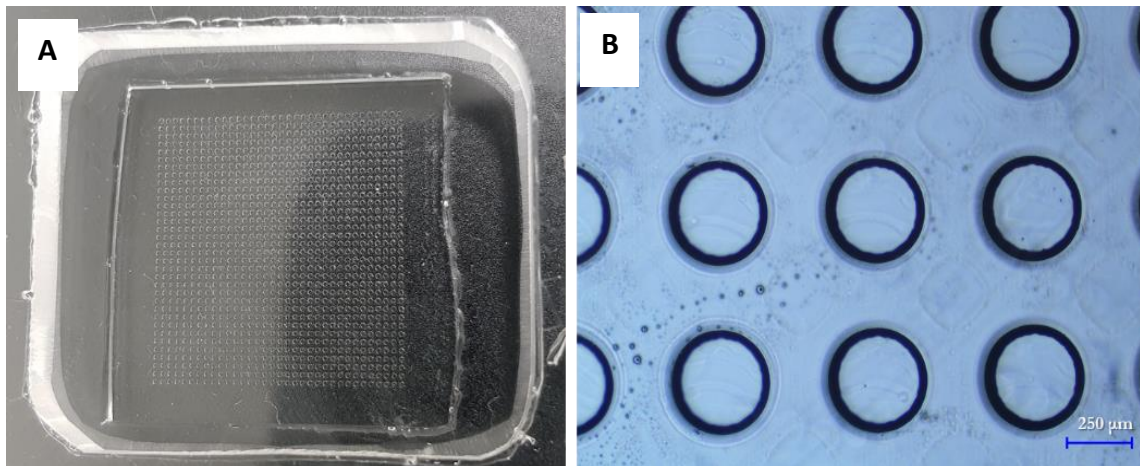


Figure 25: (A) Image of a polydimethylsiloxane (PDMS) multi-microwells mold (1,156 wells); (B) a magnification of the same mold where the well size is better appreciated (300 μm).

The mold was centrifuged at 1500 rpm for 5 min, in order to allow cells to settle by gravity into the microwells and then being incubated at 37 °C under 5% CO₂ environment. After 1 h, the medium was carefully aspirated to remove the cells outside the microwells and fresh medium was added to the mold. The medium was changed every two days and after 5 days of incubation the spheroids were formed, as seen in Figure 26.

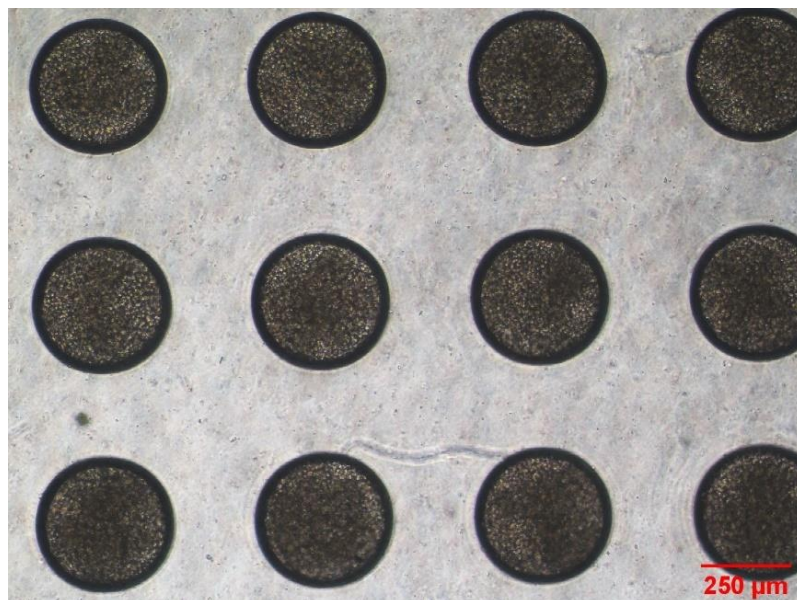


Figure 26: Optical image of growth spheroids in a PDMS mold.

In order to better recapitulate the complexity of a human liver cancer scenario, a second 3D advanced model was generated from the developed spheroids, a **liver-tumor**

organoid. In an organoid, cell–cell interactions predominate over cell–substrate interactions and their microenvironment is able to better mimic growth kinetics, gradients of nutrient distribution, oxygen concentration, and cell proliferation.

The previously formed spheroids were collected from PDMS mold and suspended in RPMI1640 medium mixed with 14% of gelatin methacryloyl (GelMA) and 2% of 2-Hydroxy-4'-(2-hydroxyethoxy)-2-methylpropiophenone. GelMA was used to support the architecture of the developed spheroids microstructure. Afterwards, the spheroids suspension was seeded in a 96 wells plate (150 μ L per well) and the plate was subsequently exposed to UV-light (365 nm) for two minutes, promoting the photo-polymerization of GelMA and thus forming the liver-tumor organoid (Figure 27).

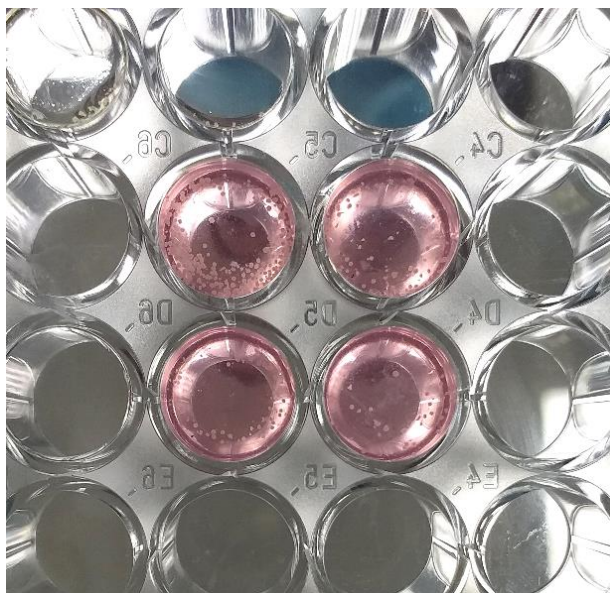


Figure 27: Image of the photo-polymerized GelMA containing the developed HepG2 spheroids in a multi-well plate.

3.5. BIOLOGICAL CHARACTERIZATION

Beyond the physicochemical characterization of the nanomaterials, it is essential to carry out biocompatibility and toxicological tests in *in vitro* cell models. In this subchapter, a description of the main biological assays, methodologies performed to preclinically assess the biocompatibility and theranostic performance of GbMNPs@PF127 and the relevant equipment used for biological characterization are presented. In this work, all the cell culture

work was carried out in a laminar flow chamber in the INL cell culture laboratory under appropriate aseptic conditions.

3.5.1. Confocal microscopy

The conventional optical microscopy, also named light microscopy, uses a beam of visible light that is directed uniformly to the sample over a relatively large area and light is collected with a lens system that forms a magnified image [180,181]. Although the highest light intensity is focused on one point, there is illumination in other parts of the sample, resulting in background “noise,” which affects the quality of the image [182]. In confocal microscopy, a beam of light (the excitation beam) is focused through the microscope objective on a small point inside the sample. This objective captures the reflected or fluorescent light coming back from the sample, and the light is projected and not seen directly. Confocal microscopy uses a small pinhole aperture to block out-of-focus light, allowing just the light emitting from the desired focal point [180,182]. Two-dimensional images are acquired plane to plane, at different depths, which allows fluorescence detection in thick samples. Three-dimensional structures can be reconstructed by scanning several planes, acquiring several two-dimensional images and stacking them, using a microscopy deconvolution software (z-stack). This equipment allows the visualization of different sections of a sample using dyes that fluoresce when stimulated by light (fluorophores) [183]. Fluorophores improve sensitivity and specificity, increasing the signal-to-noise ratio and a better and sharper detection of the sample. The excitation light is provided by a laser at a wavelength that will also excite a specific fluorophore. Thus, when the sample is illuminated through the excitation laser, high fluorescence intensities at a well-defined focal point are produced [182,183].

Figure 28 represents a simplified scheme of a confocal microscope. Firstly, when a laser light is used, the light is focused into a dichroic mirror, then the light is reflected into an objective that directs the light into a single point in the focal plane of the sample. The emitted fluorescent light from this point is focused at the spatial filter with pinhole and reaches the detector. The emitted light outside the focal point is eliminated by the pinhole and the final image is the light collected from a highly focused point.

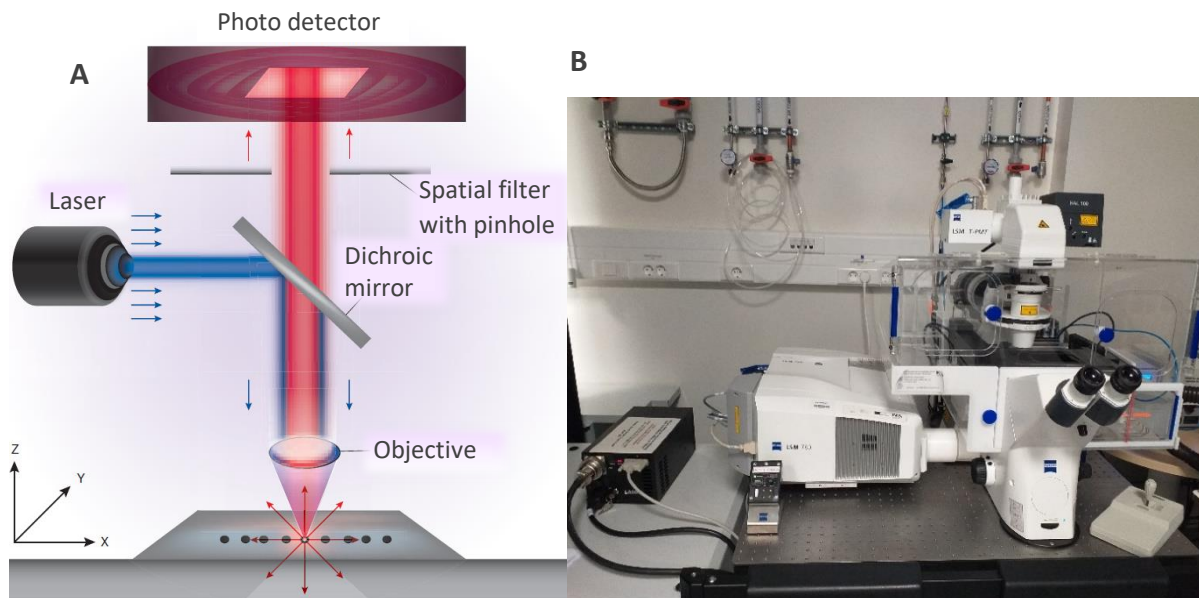


Figure 28: (A) Simplified scheme of a confocal microscope and (B) image of the confocal microscope LSM780 used in this work.

The confocal microscope LSM780 was used to study the viability of the developed HepG2 organoids, using a Live/Dead assay (Dojindo, Kumamoto, Japan) 24h and 72h after their formation in order to differentiate between live and dead cells.

3.5.2. Cellular function of liver-tumor organoids

The enzyme-linked immunosorbent assay (ELISA) is a method used for the quantitative or qualitative detection of analytes based on the specific link between an antigen and an antibody, being highly specific. In an ELISA assay, an antigen must be immobilized on a solid surface (usually a 96-well cell culture plate, with a high protein-binding surface) and then complexed with an antibody that is bound to a marker (usually an enzyme). Detection is performed by evaluating the activity of the conjugated enzyme, which is measurable using a substrate that changes color when modified by the enzyme.

Immobilization of the desired antigen can be achieved via two different methods: direct adsorption on the assay plate or indirectly by pre-coating the plate with a capture antibody. The antigen is then detected directly (labeled primary antibody) or indirectly (labeled secondary antibody). There is a third method of the ELISA assay known as the

sandwich ELISA assay, which is used because of its sensitivity and robustness. This type of assay is called a sandwich assay because the analyte to be measured is bound between two primary antibodies - the capture antibody and the detection antibody. Compared to the direct ELISA method, sandwich ELISA has greater specificity and is effective in cases where high precision is required [184,185].

To evaluate the cellular function of the HepG2 organoids, the sandwich ELISA assay was performed. The human albumin ELISA kit and human transferrin ELISA kit were used to recognize native human albumin and transferrin proteins in cell culture supernatant samples [186,187]. Albumin is the main protein of plasmas and has a good binding capacity for water, Ca^{2+} , Na^+ , K^+ , fatty acids, hormones, bilirubin and drugs. The main function of albumin is the regulation of the colloidal osmotic pressure of blood [186]. Transferrin is an iron binding transport protein that can bind two Fe^{3+} ions in association with the binding of an anion, usually bicarbonate. The main function of transferrin is the transport of iron from absorption and degradation sites to the storage and use sites. Serum transferrin may also have a further role in stimulating cell proliferation [187].

The used human albumin ELISA kit (ab179887) and human transferrin ELISA kit (ab187391) from Abcam provide all the necessary reagents (listed in Table 8 and 9 respectively) for quantitative measurement of albumin and transferrin in cell culture supernatants. All reagents from both albumin and transferrin kits were stored at temperature of 4 °C.

Table 8: Materials supplied from human albumin ELISA kit.

Item	Amount	Storage
Human albumin capture antibody 10X	600 µL	
Human albumin detector antibody 10X	600 µL	
Human albumin lyophilized native protein	2 vials	
Antibody diluent	6 mL	
Wash Buffer 10X	20 mL	Store at 4 °C
Development Solution	12 mL	
Stop Solution	12 mL	
Sample Diluent	2 x 50 mL	
Anti-tag coated microplate (12 x 8 well strips)	96 wells	
Plate Seal	1	

Table 9: Materials supplied from human transferrin ELISA kit.

Item	Amount	Storage
Human transferrin capture antibody 10X	600 μ L	
Human transferrin detector antibody 10X	600 μ L	
Human transferrin lyophilized recombinant protein	2 vials	
Antibody diluent	6 mL	
Wash Buffer 10X	20 mL	Store at
Development Solution	12 mL	4 °C
Stop Solution	12 mL	
Sample Diluent	2 x 50 mL	
SimpleStep Pre-coated 96-well microplate	96 wells	
Plate Seal	1	

To obtain the samples from 2D cell platform, HepG2 cells were seeded in three wells in a 96-well plate at a concentration of 2×10^5 cells mL^{-1} and maintained in culture for 3 days, and in each time-point (24, 48 and 72 h) the medium was collected and frozen at -80 °C until testing. On the other hand, to obtain the samples from 3D cell platform, three organoids (at a concentration of 3×10^5 cells mL^{-1}) were transferred to a 96-well plate and filled with 200 μ L of medium. After 24, 48 and 72 h of incubation the medium from each well was collected and store at -80 °C until further use. During the incubation time, the medium was replaced every 24, 48 and 72 h. To carry out this test, the samples were all previously thawed and the solutions were prepared following the manufacturer's instructions. First, 1x wash buffer was prepared by diluting wash buffer 10x with Mili-Q water. Then, the antibody cocktail was prepared by diluting the capture and detector antibodies in antibody diluent.

According to the provider's instructions, different serial diluted standards were prepared for each kit, where the stock standard solution is a mix of albumin/transferrin standard with 1000 μ L of sample diluent. The two stock solutions were kept at room temperature for 10 minutes. Next, 220 μ L of Sample Diluent was added to eppendorf number 1 and 150 μ L of Sample Diluent was added to eppendorf number 2-8 for albumin assay. In the case of transferrin assay, 390 μ L of Sample Diluent was added to eppendorf number 1 and 150 μ L of Sample Diluent was added to eppendorf number 2-8. Then, the stock standard was used to prepare the dilution series according to Figure 29. The Eppendorf number 8 is the blank control (contains no protein). Then, 50 μ L of each sample (collected medium from organoids and HepG2 cells for 24, 48 and 72 h) were added into the wells of the plate. And 50 μ L of the

antibody cocktail solution previously prepared was added to each well. The plate was incubated for 1 hour at room temperature on a plate shaker at 400 rpm. After incubation, each well was washed 3 x 350 μ L 1x wash buffer. 100 μ L of development solution was added to each well and incubated for 10 minutes in the dark on a late shaker set to 400 rpm. Then, 100 μ L of stop solution was added to each well and the plate was ready to read the absorbance at 450 nm.

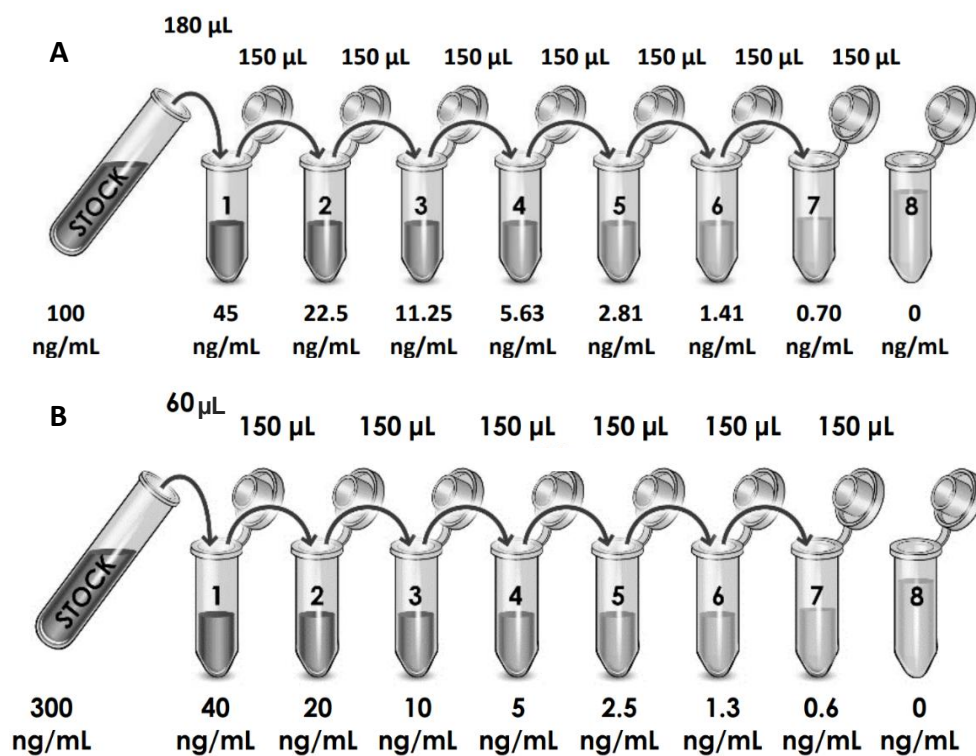


Figure 29: (A) dilution series for albumin assay; (B) dilution series for transferrin assay.

3.5.3. Cytotoxicity and anticancer effect assessment

To study cytotoxicity at different concentrations of GbMNP@PF127 in 2D cultured tumor cells and to evaluate their performance to act as anticancer therapeutic effect Aquabluer assay was used. On the other hand, the cytotoxicity of the developed HepG2 organoids was analyzed using two different methods, one based on the confocal microscope assessment using a Live/Dead assay 24 h and 72 h after the formation of the organoids, and

other using LDH cytotoxicity assay 14 days after their formation. The performance in 3D liver-tumor organoid to act as anticancer therapeutic effect was also tested with LDH assay.

3.5.3.1. AquaBluer

As mentioned above, the Aquabluer assay was used for two studies on 2D models: study cytotoxicity at different concentrations of GbMNP@PF127 in 2D models and to evaluate their performance to act as anticancer therapeutic effect.

AquaBluer is a redox indicator for cell viability assays, where viable cells turn AquaBluer from its oxidized form (nonfluorescent and blue) to the reduced form (fluorescent and red). The fluorescence intensity is proportional to the number of viable cells in the sample [188,189]. The assay was carried out according to the manufacturer's recommendations (MoBiTec, USA).

To determine the cytotoxic effect at different concentrations of GbMNP@PF127 against HepG2 cells using the redox AquaBluer fluorometric assay HepG2 cells were plated at a density of 5×10^4 cells mL^{-1} in a 96-well plate at 100 μL per well and incubated with supplemented RPMI-1640 medium overnight at 37 °C under 5% CO_2 environment. Next day, cell medium was removed and the cells were treated with new medium containing the GbMNP@PF127 at the following concentrations: 1, 5, 10, 20, 30, 50 and 100 $\mu\text{g mL}^{-1}$. Two control groups were used, a negative control where the cells were not treated with nanoparticles (no treatment, NT) and a positive control where cells were treated with Triton-X. After 24, 48 and 72h of incubation, the AquaBluer assay was performed.

The other study performed with Aquabluer assay that evaluates the performance of GbMNP@PF127 to act as anticancer therapeutic effect consisted of using the petri dishes with 4 compartments seeded with HepG2 cells and filled with different treatment conditions (as explained in the section 3.5.4.1.). After 48 h of incubation in those treatments (for control and petri dishes treated with an applied AMF – magnetic hyperthermia), the AquaBluer assay was performed.

AquaBluer assay performed to the well plate and petri dishes (both tests) consisted of adding 100 μL of AquaBluer solution (1:100 in supplemented RPMI-1640 medium) in each well/compartment of petri dish and incubated for 2 h at 37 °C in the CO_2 incubator. The

solution from each compartment was also transferred to a 96-well plate. Both 96-well plates were analyzed in a microplate reader (Biotek Synergy H1) at 540ex/590em wavelengths. Each test was repeated three times and standard deviation was calculated.

3.5.3.2. Live/Dead

The Confocal microscope LSM780 from Zeiss was used to analyze the viability of HepG2 organoids, using a Live/Dead assay (Dojindo, Kumamoto, Japan) 24 h and 72 h after organoid formation. To allow differentiation between live and dead cells, a cell-permeant dye solution was prepared by adding 3 μ L of calcein acetoxymethyl ester (calcein AM) and 3 μ L of Propidium Iodide (PI) solution to 1 mL of PBS. The nonfluorescent calcein AM in live cells is converted to a green-fluorescent calcein after acetoxymethyl ester hydrolysis by intracellular esterases. On the other hand, PI binds to double stranded DNA and it is excluded from cells with intact plasma membranes, being present only in DNA of cells where the plasma membrane has been compromised/ permeabilized and it is visible with red color [190,191]. The organoids were collected from the wells with a spatula and the embedded spheroids were stained by adding 100 μ L of the dye solution on top of the organoid. Subsequently, the organoids were incubated at 37 °C under 5% CO₂ environment. The stained cells were analyzed using a confocal laser scanning microscope (LSM780, Zeiss).

3.5.3.3. Lactate dehydrogenase (LDH)

The cell viability of HepG2 organoids at different time intervals was quantified using the colorimetric LDH assay. The Invitrogen CyQUANT LDH Cytotoxicity Assay Kit provides the required reagents that are needed in order to quantify cellular cytotoxicity, through a colorimetric method, as show in Table 10.

Table 10: Contents and storage from LDH cytotoxicity assay kit.

Item	Amount	Storage
Substrate Mix	1 vial	Store at -20 °C, Protect from light
Assay Buffer	1 x 600 µL	
Lysis Buffer	1 x 2.5 µL	
Stop Solution	1 x 12 µL	
LDH Positive control	1 x 6 µL	

The cytosolic enzyme, LDH, is present in many cell types. When damage to the plasma membrane occurs, LDH is released into the cell culture medium. The extracellular LDH released into the medium can be quantified by a coupled enzymatic reaction in which LDH catalyzes the conversion of lactate to pyruvate by NAD⁺ reduction to NADH. Oxidation of NADH by diaphorase causes the reduction of a tetrazolium salt (INT) to a red formazan dye that can be detected by UV-vis spectrophotometry at 490 nm wavelength (Figure 30). The amount of Formazan present is directly proportional to the amount of LDH released into the cell culture medium, which is indicative certain degree of cytotoxicity.

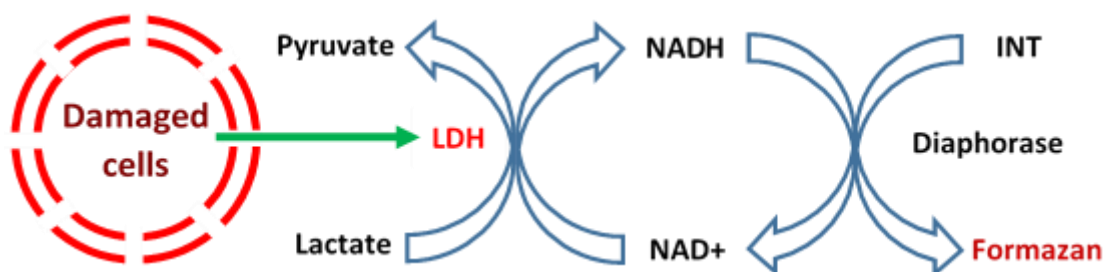


Figure 30: Schema of the CyQuant LDH cytotoxicity assay mechanism. Adapted from [192].

LDH assay was performed for two different studies. One of them was used to study the organoids viability: after the formation of organoids, four of them were transferred to a 96-well plate and filled with 200 µL of medium. Then the 96-well plate was incubated and at each time-point (1, 2, 3, 7, 10, 14 days) the medium from each well with organoids was collected and frozen at -80 °C until testing. The wells with organoids were always replaced with 200 µL of medium. After 1, 2, 3, 7, 10, 14 days of incubation the medium from each well was collected

and store at -80 °C until their further use. During the incubation time, the medium was replaced every time-point.

The other experiment using LDH assay was to evaluate the performance of GbMNP@PF127 against HepG2 cells in 3D liver-tumor organoids after 48 h of being subjected to an alternating magnetic field – magnetic hyperthermia.

When all the mediums were collected (for both assays), the cellular cytotoxicity was quantified using the reagents listed in Table 10 and following the instructions in the Invitrogen CyQUANT LDH Cytotoxicity Assay Kit: first, substrate stock solution was prepared mixing 11.4 mL of Mili-Q water with the entire content of the substrate mix. Then, the reaction mixture was prepared combining 600 µL of assay buffer stock solution with the substrate stock solution, then the resulting solution was mixed gently and protected from light. After, 1X LDH Positive Control was prepared diluting 1.5 µL of LDH Positive Control with 1 mL of 1% BSA in PBS. 10 µL of sterile water to the spontaneous LDH release containing cells was added. After, 10X lysis buffer to the maximum LDH release was added. Then the plate was incubated at 37 °C for 45 minutes. Then, 50 µL of each sample medium (spontaneous LDH activity Controls and maximum LDH activity controls) was transferred to a 96-well plate in duplicate wells. An LDH positive control was also performed, aliquoting 50 µL of 1x LDH Positive Control into duplicate wells. 50 µL of reaction mixture were transferred to each sample well and mixed by gentle tapping. The plate was incubated at room temperature and protected from light for 30 minutes. After, 50 µL of stop solution were added to each sample well and mixed. Then, the absorbance was measured at 490 and 680 nm. LDH activity was determined subtracting the 680 nm absorbance value (background signal from instrument) from the 490 nm absorbance value.

3.5.4. *In vitro* functional validation

To evaluate the theranostic performance of GbMNP@PF127 *in vitro*, HepG2 cells were incubated with the nanoparticles to afterwards test the theranostic functionality of the GbBMNP@PF127, namely their induced thermochemotherapeutic effect mediated by magnetic hyperthermia and their ability to act as MRI contrast agents.

3.5.4.1. Thermochemotherapy

To evaluate the induced thermochemotherapeutic effect of GbMNP@PF127 against HepG2 cells in 2D and 3D models, petri dishes for the control and petri dishes for the hyperthermia were used. For 2D model 10×10^3 cells mL^{-1} (100 μL per well) were seeded in each compartment of a dedicated petri dish (divided into 4 compartments) and incubated for 24h with supplemented RPMI-1640 medium overnight at 37°C under 5% CO_2 environment. After this period the medium was removed and 100 μL of different solutions (mentioned below) were added in each compartment. For 3D model one organoid was placed in each compartment. Thereafter, each compartment of the petri dish hosted different treatment conditions in order to unravel the different contributions to the total cytotoxicity induced by GbMNP@PF127@DOX to the HepG2 cells (Figure 31) and HepG2-derived organoids (Figure 32). Therefore, the treatment conditions in each well were the same ones used for 2D and 3D models:

- Organoids/cells only with RPMI-1640 medium (no treatment);
- Organoids/cells treated with medium containing GbMNP@PF127 ($50 \mu\text{g Fe mL}^{-1}$)
- Organoids/cells treated with medium containing GbMNP@PF127@DOX ($135 \mu\text{g DOX mL}^{-1}$);
- Organoids/cells treated with DOX ($135 \mu\text{g mL}^{-1}$).

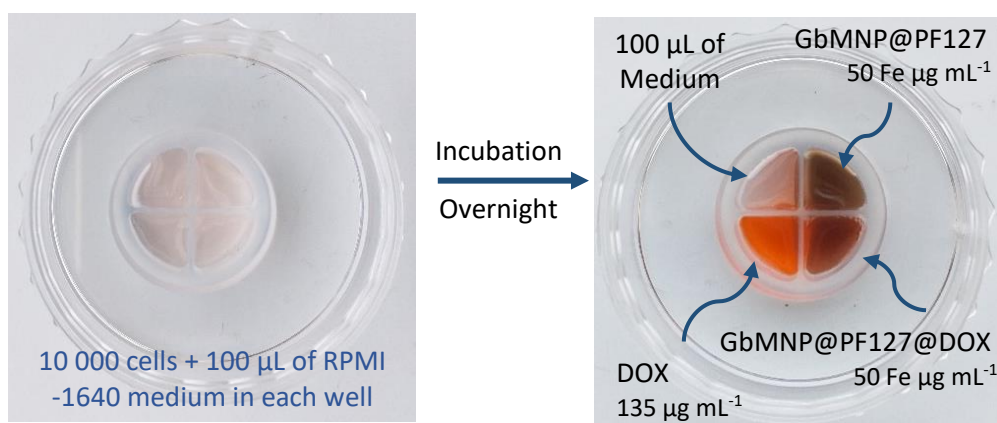


Figure 31: Schematic procedure of the *in vitro* experiment with HepG2 cells using petri dishes divided into four different groups.

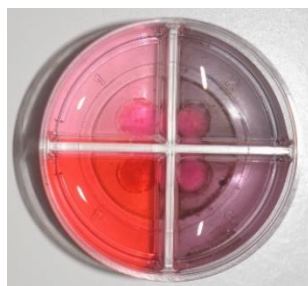


Figure 32: Picture of a petri dish containing one organoid in each compartment.

After adding the medium to each well with the cells and organoids, the plates were incubated 24 h. then, the petri dishes planned for magnetic hyperthermia treatment were subjected to an AMF for 1 h at a field and frequency of 20 mT and 285.4 kHz, respectively, in a NAN201007 Live Cell Exposure accessory from nanoTherics. After magnetic hyperthermia treatment, the petri dishes were incubated for 48 h. Afterwards, cell's viability of HepG2 cells was measured by the AquaBluer assay and the medium from HepG2 organoids was collect for analysis using LDH assay.

3.5.4.2. MRI

In order to validate the *in vitro* contrast enhancement capability of GbMNP@PF127 for MRI applications, it is important to measure changes in the relaxation time of the water protons *in vitro* when the nanoparticles interact with the cells. This assay allows to observe if the internalization of GbMNP@PF127 in HepG2 cells is able to induce a dark contrast effect (reduction of transversal relaxation time) in MRI, so confirming GbMNP@PF127 as suitable T₂-MRI CA for theranostic applications.

To perform this assay, T-75 flasks cultured with HepG2 cells were used. In each T-75 flask, 3,000,000 HepG2 cells were seeded and incubated until they reach 80% confluence. Then HepG2 cells were incubated with GbMNP@PF127 at different concentrations overnight. Next day, the medium from the flasks was aspirated, the cells washed twice with 1xPBS and detached using 2-3 mL of trypsin. After being incubated for five minutes, the trypsin was neutralized with 4 mL of RPMI-1640 and the cell suspension was centrifugated at 1200 rpm for 5 minutes. The supernatant was discarded, and the pellet was resuspended with 4 mL of medium and then live cells were counted using Trypan Blue Solution (dilution of 1:4). The

maximum cell value common to all culture flasks (4×10^6 cells) was transferred to a 15 mL falcon and each falcon was centrifuged at 2000 rpm for 10 minutes. Then, the cells were fixed with 2.5% glutaraldehyde and 2% of paraformaldehyde in 0.01M PBS. The cells were then washed with PBS and centrifugated again and the obtained pellet was subjected to MRI in a MR Solutions Benchtop scanner.

MR imaging was performed in a MR Solutions Benchtop scanner (Guildford, UK), under a magnetic field of 3.0 T horizontal bore, at room temperature. To image the samples, a 56 mm diameter quadrature birdcage coil was used in transmit/ receive mode. For the phantom measurements, 200 μ L of GbMNP@PF127 samples were placed on a custom-printed PLA sample holder. The spaces with no sample were filled with water. The holder was positioned in the center of the MRI scanner bore, and SCOUT acquisition was made to verify the correct position of the sample. For r_2 in water, a T_2 map was acquired with a multi-echo-multi-slice (MEMS) sequence with the parameters mentioned in Table 11. Post-processing was performed using ImageJ software (1.46r, NIH, USA) for the reconstruction of T_2 maps according to the standard equation $S_n = S_0 (1 - e^{-\frac{T_E n}{T_2}})$, where T_E is echo time, S_0 is signal intensity at 0 ms, and S_n is signal intensity at $T_E n$. r_2 was calculated from the slope of the curve obtained by fitting the T_2^{-1} values versus the total Fe concentration in mM [193]. MR imaging was performed in the same MRI system equipped with 48 G cm⁻¹ actively shielded gradients. For T_2 -weighted imaging, a fast spin echo (FSE) sequence with the following parameters was used: T_E (echo time) = 17 ms, T_R (repetition time) = 2150 ms, NA (number of averages) = 6 and AT (total acquisition time) = 49m 49s. All MR images of the phantoms were acquired with an image matrix 256×252 , field of view (FOV) 60×60 mm, 6 slices with a slice thickness of 1 mm and 0 mm slice gap.

Table 11: Parameter of acquisition of T_2 maps.

Matrix	256 x 252
Field of view (FOV)	60 x 60 mm
Slices	6
Slice thickness	1 mm
Slice gap	0 mm
T_E	17 ms
T_R	2150
Echoes	15

4. RESULTS AND DISCUSSION

4.1. PHYSICOCHEMICAL CHARACTERIZATION OF GbMNPs

4.1.1. Fe concentration

First, a dispersion of GbMNP@PF127 functionalized with Pluronic F127 was prepared in Mili-Q water from naked GbMNP, which were provided by our partners from the Polytechnic Institute of Bragança. Before and after a purification process at 4000 rpm for 45 minutes to remove the bigger and unstable nanoparticles, the Fe content in nanoparticles dispersion was quantified by ICP-OES (ICPE-9000 Multitype ICP Emission Spectrometer, Shimadzu) (Table 12).

Table 12: Fe concentration in GbMNP@PF127 dispersions determine by ICP-OES.

GbMNP@PF127	Fe ($\mu\text{g mL}^{-1}$)
Before purification	2000
After purification	144,7

According to the data of Table 12, a significant decrease in the Fe content around 93% was observed, meaning that most of the nanoparticles precipitate under the purification (centrifugation) conditions. Thus, the larger and more unstable nanoparticles deposited at the bottom of the Falcon after centrifugation forming a pellet that was later discarded. The GbMNP@PF127 dispersed in the supernatant at the concentration of $144,7 \mu\text{g Fe mL}^{-1}$ were kept for further development.

4.1.2. Hydrodynamic particle size

The average hydrodynamic diameter and surface charge of GbMNP@PF127 were determined by dynamic light scattering (DLS) and zeta potential measurements (Nano Particle Analyzer Z-100) at a concentration of 0.1 mg mL⁻¹ dispersed in Milli-Q water at room temperature (n = 3). The obtained results are showed in Figure 13.

Table 13: Colloidal and dimensional properties of GbMNP@PF127: hydrodynamic diameter, polydispersion and zeta potential.

Samples	Hydrodynamic diameter	Polydispersion	Zeta Potential
Before purification	322,6 ± 45,1 nm	1,343 ± 0,52	-59,4 ± 0,3 mV
After purification	171,6 ± 10,9 nm	0,36 ± 0,03	-56,3 ± 1,2 mV

Nanoparticle size, shape and surface charge dictate biodistribution among the different organs, including liver, when systemically administered in the organism. Large particles with diameters bigger than 2000 nm accumulate readily within the liver. Nanoparticles with size range of 100–200 nm have been shown to extravasate through vascular fenestrations of tumors (due to the enhanced permeability and retention effect), escape filtration by liver and be preferably accumulated into tumor rather than in healthy tissues [194]. Before centrifugation, the dimensions of the hydrodynamic diameters had very high values, around 320 nm, consequently they would be very likely retained within the liver. A final purification process was able to significantly reduce the hydrodynamic diameter of GbMNP@PF127 and separate a nanoparticles population of suitable particle size (around 170 nm), for intravenous administration with expected prolonged blood circulation.

4.1.3. Zeta potential

Nanoparticle surface charge can be tailored to prolong circulation lifetimes and selectively enhance accumulation at specific desired sites. Highly cationic nanoparticles are rapidly eliminated from circulation, to a greater extent than highly anionic nanoparticles. Thus, neutral and negatively charged nanoparticles present significantly prolonged circulating

lifetimes by avoiding opsonization phenomena and their elimination from blood by macrophage cells [194]. As observed in Table 13, GbMNP@PF127 have a negative surface charge, before and after purification, confirming the efficiency of the functionalization with PF127 and the incorporation of carboxylic acid groups on the GbMNP@PF127 surface.

4.1.4. DOX loading efficiency / capacity:

The incubation of GbMNP@PF127 with DOX in the weight ratio 1:1 for 48 h, demonstrated an exceptional drug loading efficiency of $96 \pm 2 \%$ and a drug loading capacity of 0.96 ± 0.02 mg (DOX per GbMNP). This high loading efficiency can be attributed to the interactions between DOX and the graphene layers of GbMNP. DOX binds to graphene mainly through π - π stacking interaction between the conjugated domains of graphene sheets and the aromatic quinone portion of DOX [195].

This chemical interaction between DOX and graphene sheets is pH dependent, thus affecting the drug loading capacity. The pH-dependent loading capacity is based on different hydrogen-bonding interaction between graphene and DOX under different pH conditions. Under neutral conditions, four types of hydrogen bonding can occur between different chemical groups, -COOH of graphene and the -OH of DOX, -COOH of graphene and the -NH₂ of DOX, -OH of graphene and the -OH of DOX, and -OH of graphene and the -NH₂ of DOX. Under acidic conditions, only two types of hydrogen bonding can occur between -COOH of graphene and the -OH of DOX, and -OH of graphene and the -OH of DOX. This could explain the stronger hydrogen-bonding interaction between graphene and DOX under neutral conditions, leading to a higher DOX loading. These characteristics allow not only a pH controlled drug loading, but also a pH tunable drug release [196,197].

In addition to DOX loading due to strong interactions between DOX and graphene surfaces, due to the unique structure of the GbMNP, we cannot discard that DOX is also loaded into the hollow cavity created by the yolk-shell architecture of these nanoparticles, contributing to a higher drug loading capacity.

4.1.5. DOX release

The release of DOX from GbMNP@PF127@DOX was monitored up to ca. 154 hours at different pH values (5, 6.5 and 7.4) at room temperature, with and without application of an AMF (magnetic hyperthermia). These pH values were chosen since blood and most tissues have a neutral pH of 7.4 in healthy conditions, while pH = 5 and 6.5 were chosen in an attempt to mimic the pH conditions of the TME and the intracellular endosome/lysosome microenvironments, respectively. The DOX release profiles are represented in Figure 33.

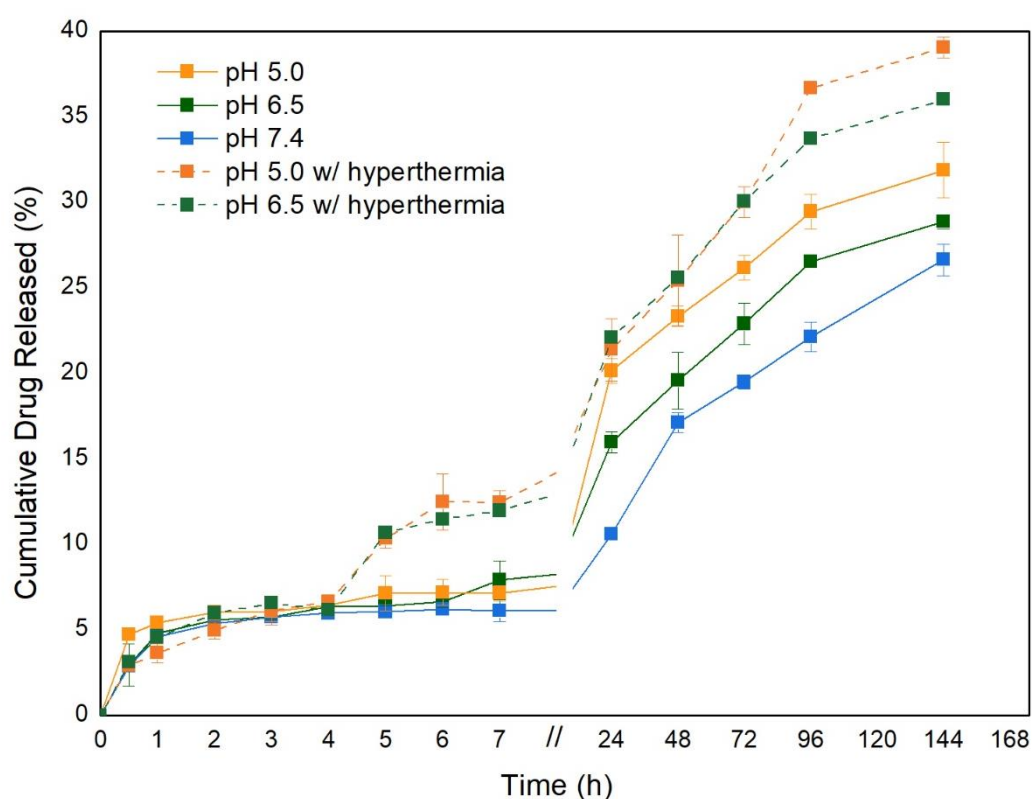


Figure 33: DOX release at different pHs (5, 6.5, 7.4) with and without magnetic hyperthermia. An AMF of 20 mT and 285.4 KHz was applied for 4 h. Values represent mean \pm SEM.

Focusing only on DOX release behaviors without the application of hyperthermia, it is perceptible that in the first 8 hours there are no significant differences in drug release between the 3 different pH conditions tested. Over time, differences among the release profiles at different pHs become noticeable and a higher release rate is clearly observed when pH decreases. A DOX release of 27, 29 and 32 % of the total amount of DOX loaded were observed after 154 hours for pHs 7.4, 6.5 and 5, respectively; the lower the pH, the higher the drug release.

The release profile of DOX under magnetic hyperthermia (application of an AMF) were also studied at two selected pH, 5 and 6.5, at which the release of DOX was higher under passive release conditions. Interestingly, the application of an AMF of 20 mT and 285.4 KHz at time $t = 4$ h for 4h induced a remarkable increase of the DOX amount released. The AMF application window was selected to allow a first passive burst of DOX that could be adsorbed on the nanoparticles surface, where it would be difficult to observe the effect of magnetic hyperthermia in the drug delivery profile. Thus, a clear increase of the amount of DOX released was observed precisely at $t = 4$ h for both pH = 5 and pH = 7.4 compared to the DOX release under passive conditions at the same pHs, coinciding with the application of the AMF and which extended over the whole time range of the experiment, up to 154 h. However, the effect of magnetic hyperthermia was independent of the pH and only significant differences in the release profiles at pH = 5 and pH = 7.4 were found after 72h. The total amount of DOX released at both pH = 5 and pH = 6.5 at the end of the experiments ($t = 154$ h) was 39% and 36%, respectively, regarding the total amount of DOX loaded, meaning 8% higher compared with the release under passive conditions at the same time point. As discussed above, the hydrogen-bonding interaction between DOX and graphene is stronger at neutral pH condition, resulting in a more efficient release at lower pHs [197]. Contrarily, under acidic conditions, the total amount of DOX release is much higher. Such results may be due to the partial dissociation of hydrogen-bonding interaction under acid conditions.

The results of the kinetic studies, listed in the Table 14, were obtained using the drug release data obtained at different pHs.

Table 14: Drug release kinetic analysis of GbMNP@PF127@DOX at different pHs. The * symbol refers to the samples that were subjected to an AMF.

pH	Zero Order			First Order			Higuchi			Hixon-Crowell			Korsmeyer-Peppas			
	K_0	AIC	R^2	K_1	AIC	R^2	K_H	AIC	R^2	K_{HC}	AIC	R^2	K_m	n	AIC	R^2
5	0.26	102.2	0.48	0.003	98.38	0.60	2.93	71.67	0.93	0.001	99.70	0.56	4.39	0.41	65.75	0.96
6.5	0.24	96.87	0.54	0.003	93.37	0.63	2.64	57.84	0.97	0.001	94.56	0.60	3.84	0.41	42.76	0.99
7.4	0.20	90.76	0.57	0.002	87.90	0.64	2.24	52.15	0.97	0.001	88.86	0.62	3.18	0.42	40.93	0.99
5*	0.32	109.0	0.44	0.005	105.1	0.60	3.67	79.13	0.93	0.001	106.76	0.55	5.79	0.39	69.82	0.96
6.5*	0.30	107.7	0.40	0.004	103.5	0.55	3.37	76.51	0.93	0.001	105.0	0.50	5.58	0.38	62.50	0.97

In this study, five kinetic models, namely zero-order, first-order, Higuchi, Hixon-Crowell and Korsmeyer-Peppas, were fitted to the drug release data obtained for each pH tested condition. The model with the higher R^2 values (for each condition) and the lower AIC was considered as the best model.

Thus, the zero-order, first-order and Hixon-Crowell models have very low R^2 values. These results suggest that the drug release, under the tested conditions, is not mainly caused by systems that release the drug at a constant rate over a period of time, concentration-dependent and dissolution by decreasing the solid surface area as a function of time. The kinetic models that better fit (higher R^2) are the Higuchi and Korsmeyer-Peppas models. Between them, the Korsmeyer-Peppas model was considered the best one to describe the system since it has a higher R^2 value and a lower AIC value. The n values calculated from the Korsmeyer-Peppas model equation were found to be lower than 0.45, suggesting that the drug release is controlled by simple quasi-Fickian diffusion mechanism.

4.2. IN VITRO PRECLINICAL VALIDATION

4.2.1. 2D models: HepG2 cells

4.2.1.1. Biocompatibility studies

An ideal nanocarrier should ensure low or negligible toxicity, therefore its biocompatibility is crucial for the final application in biological tissues. In order to analyze the cytotoxicity of the graphene-based nanoparticles *in vitro*, the metabolic activity was studied as indicator of the cell viability. Metabolic viability was studied after incubation of GbMNP@PF127 with HepG2 cells at different time points (24, 48 and 72h) and different Fe concentrations (0, 1, 5, 10, 20, 30, 50 and 100 $\mu\text{g Fe mL}^{-1}$) by using the AquaBluer reagent. The results obtained are presented in Figure 34, which shows the percentage of viable cells regarding the cell viability of the non-treated control (NT).

The AquaBluer fluorometric assay demonstrated that the GbMNP@PF127 presented a good biocompatibility below $100 \mu\text{g Fe mL}^{-1}$. Results show high biocompatibility within the whole range of Fe concentration tested. Only a limited cytotoxic effect observed was at the highest Fe concentration tested, $100 \mu\text{g Fe mL}^{-1}$, where it is possible to observe a meaningful reduction in cell viability after 48h and 72h of incubation. According to the literature, these results are consistent with the other reported results, revealing only cytotoxicity effects at high Fe concentrations [1,198,199]. Due to the observed reduction in cell viability above $50 \mu\text{g Fe mL}^{-1}$, this was the highest Fe concentration used in further *in vitro* experiments.

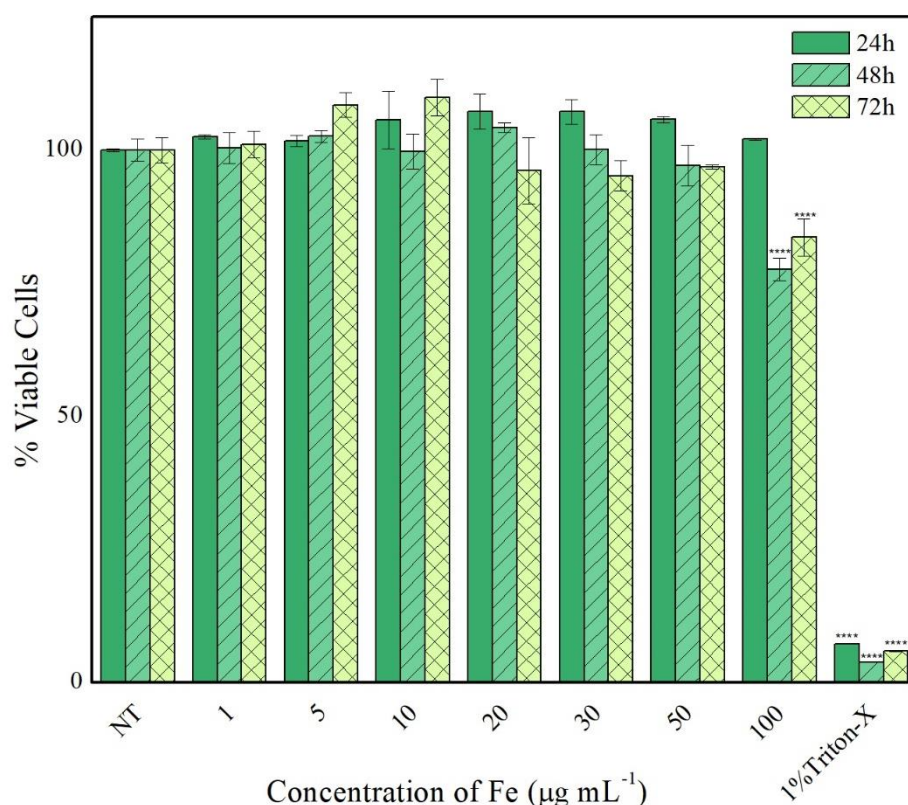


Figure 34: Metabolic viability of HepG2 cells when incubated with GbMNP@PF127 at different time points (24, 48 and 72h) and different iron concentrations ($0, 1, 5, 10, 20, 30, 50$ and $100 \mu\text{g Fe mL}^{-1}$). Values represent mean \pm SEM. Statistically significant differences were determined using Two-way ANOVA with Bonferroni test. Significant difference is relation to NT. **** $P \leq 0.0001$.

4.2.1.2. Cytotoxicity and anticancer effect

The effect of magnetic hyperthermia on cell viability was assessed by using different controls and samples. Figure 35 shows the cell viability after incubation of different

nanoparticles samples with HepG2 cells, with and without application of an AMF. The cytotoxicity assay performed was the AquaBluer fluorometric assay.

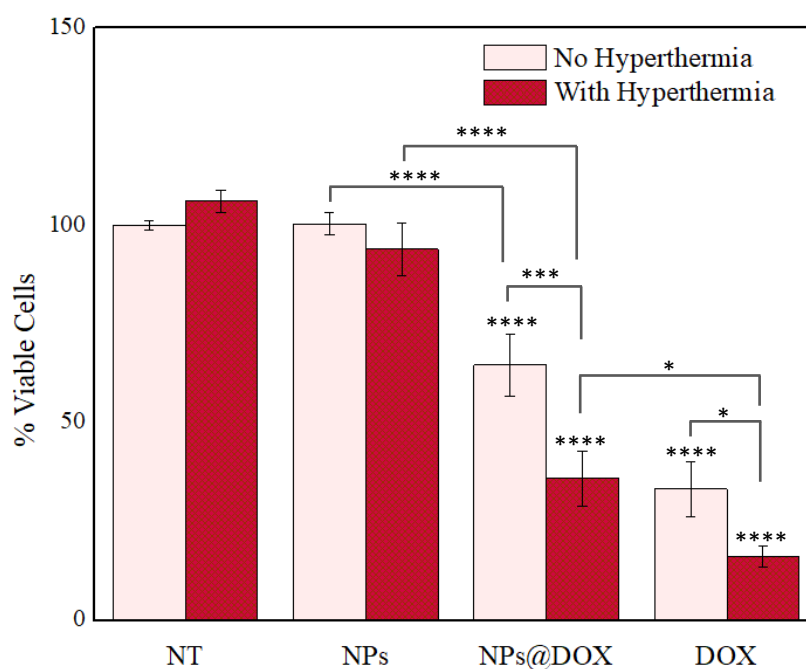


Figure 35: Percentage of viable HepG2 cells at 48h for different groups (NT- no treatment, NPs – GbMNP@PF127 nanoparticles, NPs@DOX – GbMNP@PF127 nanoparticles with encapsulated DOX and DOX- free doxorubicin) with and without hyperthermia induction. NT represents 100% of cell viability under no magnetic hyperthermia treatment. Values represent mean \pm SEM. Statistically significant differences were determined using Two-way ANOVA with Bonferroni test. Significant difference is relation to NT without hyperthermia. * $P \leq 0.05$; *** $P \leq 0.001$; **** $P \leq 0.0001$.

Cells which have not been subjected to any treatment (only in RPMI-1640 culture medium) are represented by NT and constitute the control group. The NPs group involves cells that were incubated with GbMNP@PF127 ($50 \mu\text{g Fe mL}^{-1}$), whereas NPs@DOX represents cells incubated with DOX-loaded GbMNP@PF127 at the same Fe concentration ($50 \mu\text{g Fe mL}^{-1}$). DOX group consists of cells incubated with equivalent amount of DOX as that contained in the total amount of NPs@DOX used in the previous sample group ($135 \mu\text{g mL}^{-1}$).

As observed in Figure 35, magnetic hyperthermia does not exert toxicity to cells treated with nanoparticles in the absence of DOX, since there are no significant differences in cell viability with and without magnetic hyperthermia. However, interesting results are obtained when HepG2 cells are treated with DOX-loading nanoparticles. The presence of DOX induces a significant reduction of 35% in the cell viability, which reaches a value as high as 64% when an AMF is externally supplied. This evidences the additional cytotoxic effect of magnetic

hyperthermia when in combination with the chemotherapeutic effect coming from the DOX. A potential explanation to these results relies in a dual role of magnetic hyperthermia in combination with DOX. On the one hand, the heat induced to the HepG2 cancer cells by magnetic stimulation, even if it is not enough to induce direct thermoablation, as seen with the treatment to the NT group, can sufficiently sensitize them and increase the therapeutic index of the DOX. On the other hand, in parallel the temperature increase induced in the magnetic cores of GbMNP@PF127@DOX increases the drug release of DOX and the available DOX concentration to the cells, leading to an enhanced therapeutic effect. Comparing the effect of the encapsulated and free drug on cell viability, a higher cytotoxicity effect is observed for the free DOX regarding that of the encapsulated one (NPs@DOX), inducing a 67% of cell death. Although based only in the therapeutic effect the use of GbMNP@PF127@DOX would not be justified, the potential harmful secondary effects of free DOX in an *in vivo* scenario are presumably much higher than in the case of using drug delivery systems that are able to release the drug in a more controllable and targeted manner. In addition, giving the pharmacokinetics and biodistribution of DOX, free DOX administration would involve a higher amount of drug, whereas targeted treatments using drug delivery systems would need less amount of drug to create the same drug concentration availability to the cells. Unexpectedly, the effect of magnetic hyperthermia on the viability of cells treated with free DOX also induced an extra cytotoxic effect. Further experiments will be needed to properly evaluate and confirm these results.

4.2.1.3. MRI studies

The efficiency of GbMNP@PF127 was evaluated in terms of MRI performance as T₂ contrast agent. Using relaxivity, which represents the inverse of the amount of CA needed to reduce water protons relaxation time by 1s, is possible to study the efficacy of a CA in MRI applications. In general, superparamagnetic iron oxide nanoparticles are composed of nanosized particles of magnetite with predominantly T₂ relaxation effects, which generates negative dark contrast. A T₂ behavior involves a long-range magnetic interaction with water molecules that it is caused by the magnetic field that a superparamagnetic core is able to induce under an applied magnetic field. [117,193,200]. As the magnetic cores of the GbMNPs

are composed of superparamagnetic magnetite nanoparticles around 17 nm size (annex 1(A1)) (typically T_2 -MRI effectors), a dominant T_2 -MRI behavior is expected. Accordingly, the proton relaxivity was calculated to study the feasibility of GbMNP@PF127 as T_2 -MRI contrast agents by measuring the transverse relaxation time of water protons at different concentrations of CA. Figure 36A represents the relaxation rates for GbMNP@PF127 and shows the T_2 relaxation rate ($1/T_2$) as a function of Fe concentration, which was found to be linearly dependent. The transverse relaxivity r_2 was then calculated as the slope of the linear fitting as shown in Figure 36A. The r_2 obtained for GbMNP@PF127 was as high as $208.6 \text{ mM}^{-1}\text{s}^{-1}$, which is higher than that of commercial iron oxide contrast agents at the same field strength, such as Feridex[®] ($r_2 = 93 \text{ mM}^{-1}\text{s}^{-1}$, at 3T, 37 °C) [201,202] and Resovist[®] ($r_2 = 143 \text{ mM}^{-1}\text{s}^{-1}$, at 3T, 37 °C) [201,202], both consisting of superparamagnetic iron oxide NPs approved by FDA as negative CAs.

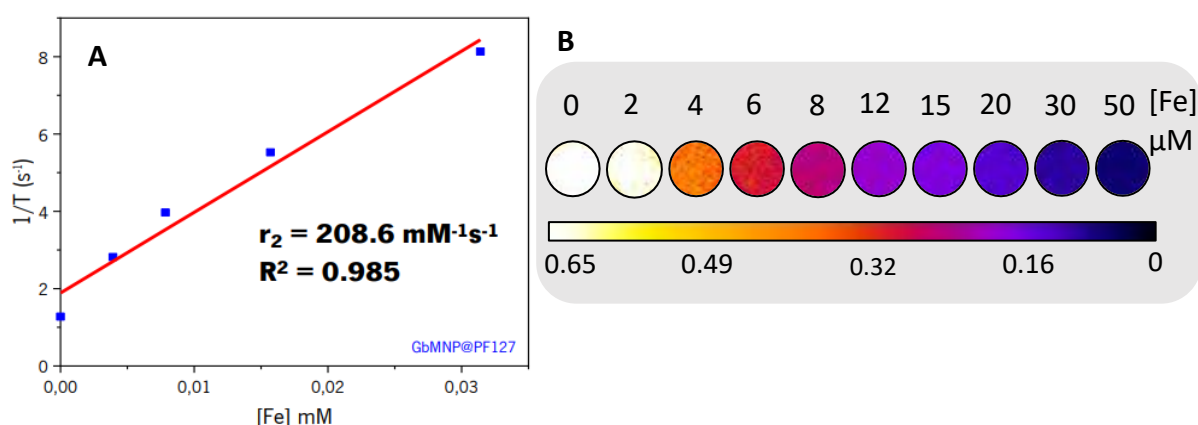


Figure 36: (A) Linear fitting of the relaxation rates at 3T for GbMNP@PF127. The slope indicates the transverse relaxivity r_2 and (B) T_2 -MRI map for GbMNP@PF127 dispersions at different Fe concentrations at a magnetic field of 3T.

A T_2 -map of phantom containing nanoparticles in solution at different concentrations (between 0 to $50 \mu\text{M}$ Fe) was acquired at 37 °C in a 3T-MRI scanner. Results of GbMNP@PF127 aqueous dispersions are shown in Figures 36B, where water was included as a control. The evolution from yellow to blue represents a concentration-dependent T_2 -MRI contrast enhancement, as denoted by the decrease in relaxation time as Fe concentration increases. The relaxation time decreases significantly with the increase of Fe concentration, which render GbMNP@PF127 suitable T_2 CAs to induce a darker contrast effect under the T_2 -imaging

acquisition sequences. Moreover, the high values of r_2 observed for GbMNP@PF127 aqueous dispersions justify the small Fe concentration (μM) required to produce a T_2 (negative) contrast enhancement effect.

In order to validate the MRI performance of GbMNP@PF127 *in vitro*, HepG2 cells were incubated overnight with different concentrations of GbMNP@PF127 (between 0 to 25 μM Fe). Figure 37A represents the relaxation rates for GbMNP@PF127 with cells, where the Fe concentration measured corresponds to the nanoparticles concentration used in the incubation with the cells (expressed in Fe concentration). This plot provides information regarding the MRI contrast enhancement capability. The results indicate that the nanoparticles internalization by cells is proportional to the amount of nanoparticles (Fe concentration) used in the incubation, since after incubation the cells were properly washed to remove all the non-internalized particles. A T_2 -map for GbMNP@PF127-labeled HepG2 cells were also acquired at 37 °C in a 3T-MRI scanner (Figure 37B), where water was included as a control. When tested *in vitro*, the GbMNP@PF127 nanoparticles uptake by cells increasingly shortened the relaxation time of water protons with the increase of the Fe concentration of the magnetic dispersions used for incubation, which indicates a linear correlation with the amount of Fe uptake by the cells. Cells incubated with a higher Fe concentration showed lower T_2 values and enhanced dark signal intensity, indicating GbMNP@PF127 as suitable T_2 -MRI (negative) contrast enhancers.

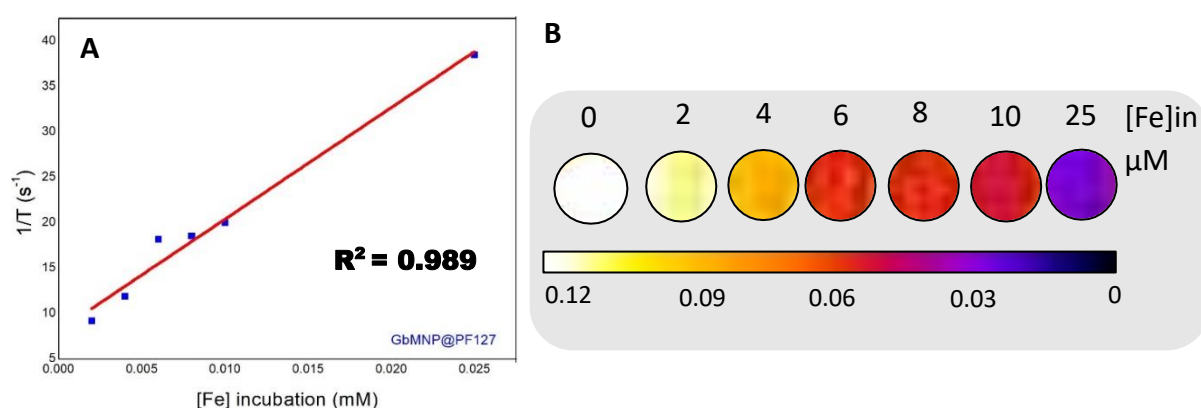


Figure 37: (A) Relaxation rates at 3T as a function of the Fe concentration of the GbMNP@PF127 dispersions used in the incubation with cells and (B) T_2 -MRI map of GbMNP@PF127-labeled HepG2 cells. $[\text{Fe}]_{\text{in}} = [\text{Fe}]$ incubation.

4.2.2. 3D models: liver-tumor organoids

4.2.2.1. Preparation of HepG2-derived organoids

Figure 38 shows an optical image of the HepG2 organoids developed from HepG2 spheroids after 5 days of culture, which were posteriorly, embedded in GelMA matrix and exposed to UV-light (365 nm) for two minutes, leading to the HepG2 organoids, as seen in Figure 38A. As noted, the organoid presents a cylindrical shape and a gelatinous texture. The visible white points represent the spheroids incorporated in the HepG2 organoid and each organoid was composed of approximately 50 spheroids. As observed in optical images (Figure 38B and 38C), the HepG2 spheroids present a well-defined round shape and a size close to 400 μm .



Figure 38: (A) image of the organoid-like gel structure removed from the wells; (B),(C) Light-microscopic images of HepG2 organoids embedded in the GelMA hydrogel.

4.2.2.2. Cell viability

Once the organoids were formed by incorporating previously prepared HepG2 spheroids into GelMA (see section 3.4.2.), their cell viability was evaluated. Two different methods were used, one based on the confocal microscopy assessment using a live/dead viability kit, and other using the LDH cytotoxicity assay.

Figure 39 shows images obtained via confocal laser scanning microscopy of embedded HepG2 spheroids in GelMA matrix, where live cells are stained in green and dead cells in red. In order to verify the longitudinal viability of the cells in the 3D culture, viability studies were performed after 24h and 72h. at both time points, there is no evidence of cell death. As denoted by the absence of red in the image. Therefore, we can conclude that HepG2 organoids are viable at least until 72h after formation. Considering that organoids are formed 5 days after spheroid formation, this means that spheroids are viable for at least 8 days after their formation.

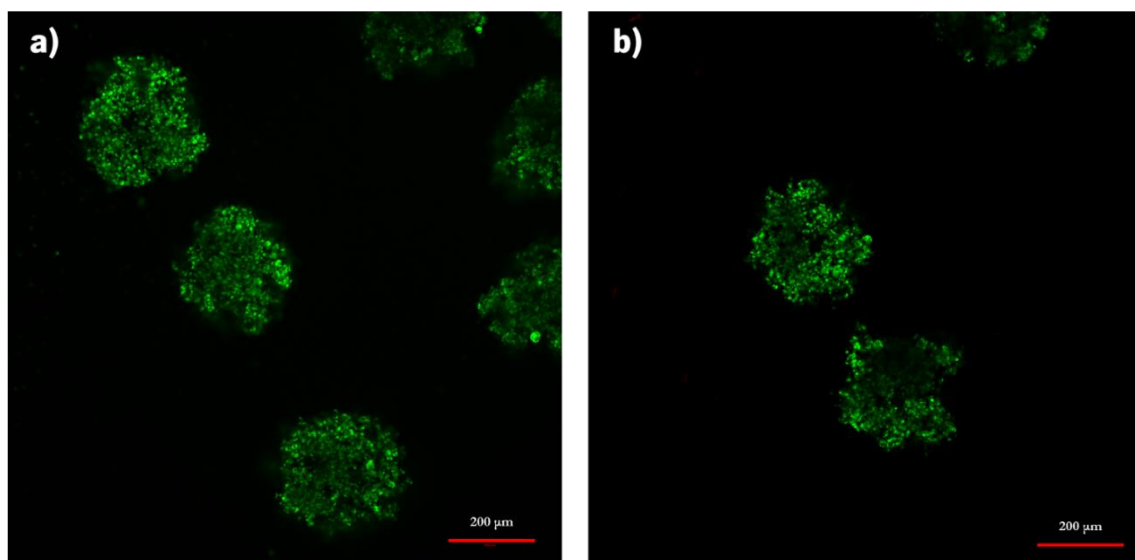


Figure 39: Confocal microscopy images of an HepG2 Organoid after a) 24h and b) 72h of his formation. The live cells were stained with green fluorescent dye (live cells) and red fluorescent dye (dead cells).

A second cytotoxicity assay was used to confirm these results. LDH was the selected method of choice to study the organoids viability up to 14 days after their formation, as shown in Figure 40.

Interestingly, organoids still show a viability of 84% after 14 days since their formation. This indicates a prolonged durability and functionality compared to conventional 2D HepG2 cell cultures and allows long-term studies with repeated dosing to assess chronic hepatotoxic effects [203].

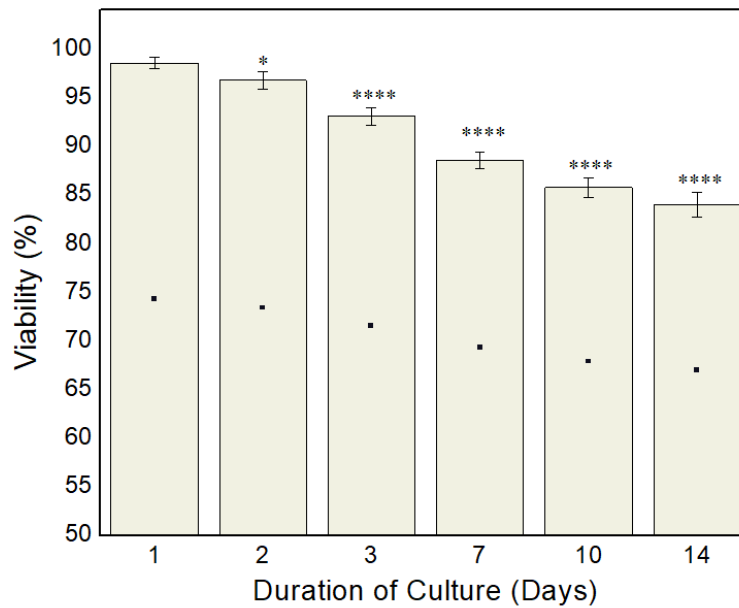


Figure 40: Cell viability in HepG2 organoids after 1, 2, 3, 7, 10, and 14 days by LDH assay. Values represent mean \pm SEM. Statistically significant differences were determined using One-way ANOVA with Bonferroni test. Significant difference is relation to 1 day of culture. * $P \leq 0.05$; **** $P \leq 0.0001$.

4.2.2.3. Cellular function

Transferrin production and albumin secretion were investigated to determine differences in hepatic function between 2D and 3D cultures. Overall, transferrin and albumin production increased in both cultures (HepG2 cells and organoids) over the culture period (Figure 41).

The production of both transferrin and albumin increased throughout the 3 days for both 2D and 3D models. However, there is a large difference regarding the production of these proteins between the 2D and 3D models: the secretion of transferrin was two-fold higher in HepG2 organoids than in HepG2 cells, and the production of albumin was five-fold higher in HepG2 organoids. In absolute numbers, HepG2 cells produced 0.87 ± 0.05 pg/cell of transferrin and 0.16 ± 0.01 pg/cell of albumin, whereas at the same time point the HepG2 organoids secreted 1.62 ± 0.02 pg/cell of transferrin and 0.74 ± 0.02 pg/cell of albumin. The fact that HepG2 organoids induce a remarkable increase of transferrin and albumin production compared to the cultured HepG2 cells suggest that the ECM can influence

hepatocyte function. Besides, it is possible to conclude that functionality of liver organoids is preserved over 72h, as indicated by persistent albumin and transferrin secretion.

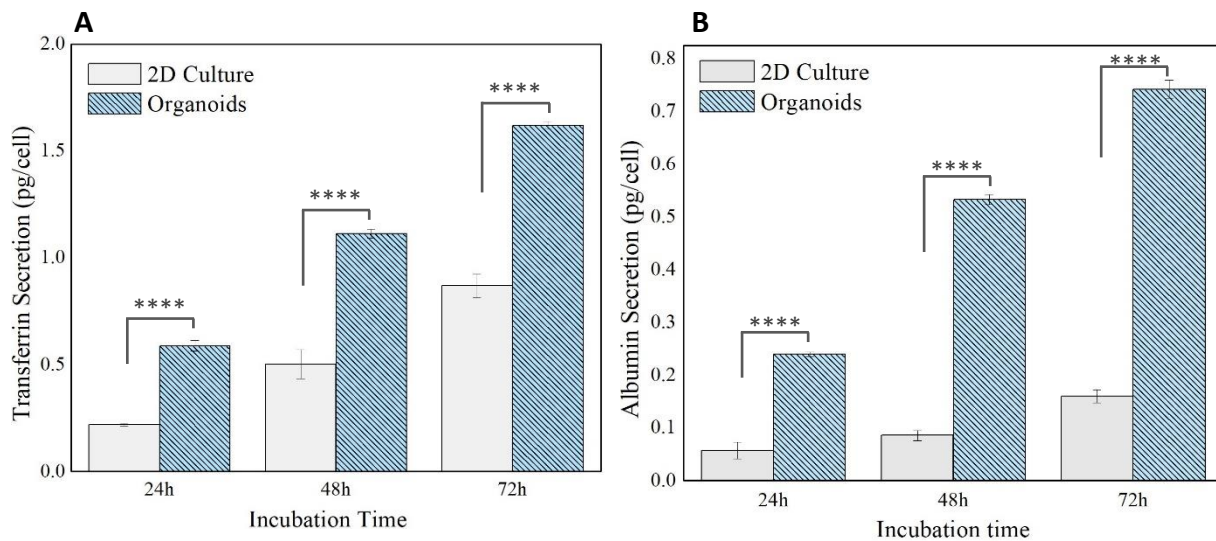


Figure 41: Quantification of secreted transferrin (A) and albumin (B) for 2D culture and organoids by ELISA at 24, 48 and 72h of incubation. Values represent mean \pm SEM. Statistically significant differences were determined using Two-way ANOVA with Bonferroni test. ****P \leq 0.0001.

4.2.2.4. Cytotoxicity and anticancer effect

According to the results presented in section 4.2.1.2. it was possible to conclude that the combination of DOX and magnetic hyperthermia through the drug loaded GbMNP@PF127@DOX nanoparticles induced a combined cytotoxic effect on HepG2 cells, as the cell viability is significantly reduced under the application of an AMF. A similar experiment was now designed to evaluate the effect of the therapy combination on the cell viability of HepG2 organoids. Thus, two different conditions, with and without hyperthermia were also performed, as shown in Figure 42.

HepG2 organoids which have not been subjected to any treatment (only in RPMI-1640 culture medium) are represented by NT and constitute the control group. The NPs group involves HepG2 organoids that were incubated with GbMNP@PF127 ($50 \mu\text{g Fe mL}^{-1}$), whereas NPs@DOX represents HepG2 organoids incubated with DOX-loaded GbMNP@PF127 at the same Fe concentration ($50 \mu\text{g Fe mL}^{-1}$). DOX group consists of HepG2 cells incubated with

equivalent amount of DOX as that contained in the total amount of NPs@DOX used in the previous sample group ($135 \mu\text{g mL}^{-1}$).

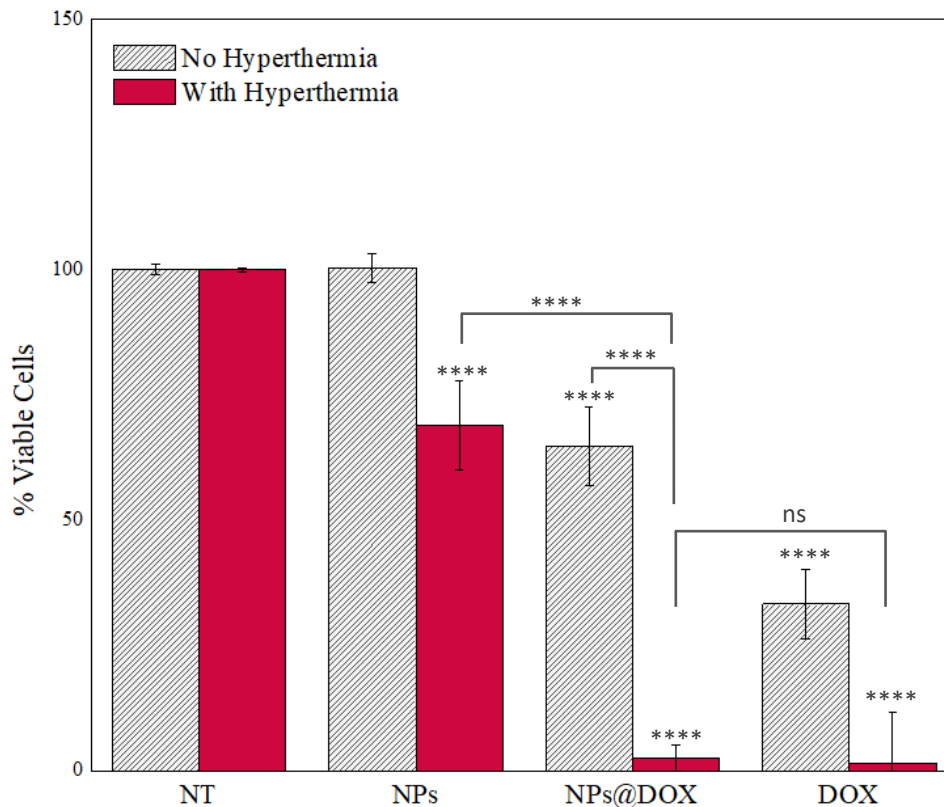


Figure 42: Percentage of viable HepG2 organoids at 48h for different groups (NT- no treatment, NPs – GbMNP@PF127 nanoparticles, NPs@DOX – GbMNP@PF127 nanoparticles with encapsulated DOX and DOX- free doxorubicin) with and without hyperthermia induction. NT represents 100% of cell viability under no magnetic hyperthermia treatment. Values represent mean \pm SEM. Statistically significant differences were determined using Two-way ANOVA with Bonferroni test. Significant difference is relation to NT without hyperthermia.; ns: not significant; ****P \leq 0.0001.

Similarly to the results observed with HepG2 cultured cells, the application of an AMF was critical to induce in HepG2-derived organoids a remarkable cell death when using the DOX-loading GbMNP@PF127@DOX nanoparticles. Thus, magnetic hyperthermia in combination with DOX induces a significant reduction of 98% in the cell viability, a 34% higher than that observed in HepG2 cells. Unlike in the experiment with HepG2 cells, GbMNP@PF127 (without DOX) acted as suitable magnetic effectors to induce cell death *per se* in HepG2 organoids, as only the effect of magnetic hyperthermia was able to reduce the cell viability to 69%, whereas no effect was observed in the case of HepG2 cells when applied alone. This is ascribed to the effect of magnetic heating and the temperature increase induced locally,

which is enough to provoke relevant cell death in the more temperature-sensitive tumor cells contained in the organoid. The better recapitulated TME may enable this cytotoxicity mechanism more efficiently than in the case of cultured HepG2 cells. In the same way, the cytotoxic effect of the AMF was more pronounced in HepG2 organoids than in HepG2 cells when both were incubated with free DOX, reaching cell viability values as low as 2%. This highlights the relevance of using advanced 3D models able to recapitulate the complexity of the human disease when testing therapeutic effects of developed drugs and formulations, since both DOX and AMF showed a higher cytotoxicity effect in HepG2 organoids than in HepG2 cells. This allows a more accurate assessment of the real therapeutic index of the drugs and therapies tested. Similarly to the experiment with HepG2 cells, the effect of magnetic hyperthermia in the free DOX group is not well understood and further research would be needed.

These results confirm GbMNP@PF127 as suitable magnetic carriers to deliver a dual therapy (thermochemotherapy) against liver cancer, in addition to behave as T₂-MRI contrast enhancers and enable MRI monitoring.

5. CONCLUSION AND FUTURE WORK

In this work, graphene-based magnetic nanoparticles functionalized with copolymer PF127 (GbMNP@PF127) were preclinically studied *in vitro* to verify their potential as multifunctional nanocarriers for liver tumor theranostics. ICP-OES analysis showed a decrease around 93% in the iron concentration in the GbMNP@PF127 dispersions after purification by centrifugation at 4000 rpm for 45 minutes. In this separation step, the larger nanoparticles and nanoparticles aggregates were removed from the dispersion, resulting in a final dispersion with smaller and more uniform nanoparticles. Furthermore, the hydrodynamic diameter of nanoparticles in aqueous solution after purification was around 170nm, which is an ideal size to escape liver filtration and for prolonged blood circulation. The surface charge of GbMNP@PF127 analyzed by zeta potential shown values around -55 mV. This electronegative value favors repulsive electrostatic interaction between nanoparticles, preventing the formation of nanoparticles clusters and aggregates and increasing their colloidal stability and biocompatibility.

Drug loading and drug release studies were performed to evaluate the potential of the developed nanoparticles as a pH-responsive drug delivery system. Due to the hollow cavity of the yolk-shell architecture of the GbMNP@PF127 nanoparticles, DOX (the drug of choice based on chemical structural and affinity for graphene layers) was successfully loaded in the GbMNP@PF127 with a drug loading efficiency of 96 % and a drug loading capacity of 0.96 mg (DOX per GbMNP). GbMNP@PF127@DOX were able to deliver the loaded drug as a function of pH in the range 5-7. Results showed that the lower the pH, the higher the amount of drug released. Moreover, an externally supplied AMF (magnetic hyperthermia) was found to modify the DOX delivery profile and enhance the drug release, which achieved a maximum value of 40% under the most acidic release conditions tested, pH = 5. These results point to GbMNP@PF127 as suitable carriers for an acidic pH-triggered drug delivery since in neutral conditions the drug release is inefficient, therefore protecting healthy tissues from side effects. This opens the possibility of a targeted drug delivery in tumor regions, enabled by the acidic pH found both in the ECM and intracellular vesicles. Overall, these results suggest that

GbMNP@PF127@DOX combined with magnetic hyperthermia have the potential to achieve outstanding results in cancer treatments.

Cell viability studies in HepG2 cultured cells were performed to study the biocompatibility of GbMNP@PF127. Results showed that the highest Fe concentration without cytotoxic effects in HepG2 cells was 50 $\mu\text{g Fe mL}^{-1}$. Accordingly, 50 $\mu\text{g Fe mL}^{-1}$ was the Fe concentration of the GbMNP@PF127 dispersions used in further experiments, ensuring negligible toxicity. In order to evaluate the therapeutic efficacy of drug release in combination with magnetic hyperthermia *in vitro*, cell viability was studied after incubation of HepG2 cells with different controls and samples, with and without magnetic hyperthermia. Results showed cell viability values around $\sim 65\%$ when HepG2 cells were incubated with GbMNP@PF127@DOX for 48h. This indicates that the GbMNP@PF127 nanocarrier is playing its role effectively, transporting the drug, releasing it and inducing cell death. Interestingly, cell viability was further reduced to values as low as $\sim 36\%$ with the application of magnetic hyperthermia. This evidences a combined thermal and chemotherapeutic effect induced by magnetic hyperthermia and the DOX release, respectively, in cultured HepG2 cells.

In order to study the effectiveness of GbMNP@PF127 as T_2 -MRI contrast agents, the transverse relaxivity r_2 was calculated, obtaining a value of $\sim 208.6 \text{ mM}^{-1}\text{s}^{-1}$, which outweighs the commercial iron oxide contrast agents Feridex[®] ($r_2 = 93 \text{ mM}^{-1}\text{s}^{-1}$, at 3T, 37°C) [201,202] and Resovist[®] ($r_2 = 143 \text{ mM}^{-1}\text{s}^{-1}$, at 3T, 37 °C) [201,202]. T_2 parametric maps of GbMNP@PF127 in solution and in GbMNP@PF127-loaded HepG2 cells showed a remarkable reduction of the relaxation time and confirmed GbMNP@PF127 as suitable T_2 -MRI contrast agents able to provide a dark contrast enhancement.

The hepatic function of the developed liver-tumor organoid was assessed by quantification of the transferrin and albumin protein production and compared to that in 2D cultured cells. Results indicated a big difference in protein secretion between 2D and 3D cellular models, where organoids showed increase in transferrin and albumin production of 46% and 86%, respectively, compared to 2D cultures. These results suggest that the presence of the ECM in the liver-tumor organoids can influence hepatocyte function and is the reason of the higher level of protein expression observed. Moreover, as the secretion of albumin and transferrin was observed during a time window of 72h, it is possible to conclude that the cell functionality of liver-tumor organoids is preserved during this period.

A 3D organoid model of liver tumor consisting of HepG2 spheroids embedded in a GelMA matrix was fabricated in order to preclinically evaluate the combined effect of magnetic hyperthermia and chemotherapy provided by GbMNP@PF127 in an advanced and more representative model of disease. Confocal microscopy and LDH cytotoxicity assays revealed that the developed organoids were viable beyond the 2 weeks mark. After different treatment conditions, a dual role of magnetic hyperthermia was found, on the one hand affecting the drug delivery profile of the DOX release and, on the other, providing cellular thermoablation. Altogether resulted in a combined thermochemotherapeutic effect and a subsequent increase of the therapeutic index that reached the 98% of dead cells when an AMF was applied, compared to a 35% in its absence.

Overall, the physicochemical and biological properties, as well as the *in vitro* preclinical functional validation of the developed GbMNP@PF127 in both HepG2 cells and organoids provide this multifunctional drug nanocarrier with great potential for theranostic applications, since in addition to the combined pH-responsive thermochemotherapeutic effect induced by the DOX release and magnetic hyperthermia, it has the potential to act as a T₂-MRI CA and offer a dark contrast enhancement in the MR images.

Future work in the context of this study involves the fabrication of a microfluidic device where the developed liver-tumor organoid will be incorporated to form a dynamic organ-on-a-chip preclinical model. This platform is able to mimic complex human organ functions at the microscale level with the ability to reduce the discrepancies between the preclinical and clinical trials. This platform also presents advantages over the *in vivo* animal models, such as lower costs and less time-consuming, end of animal ethical concerns, and higher accuracy to predict human responses [121]. In the next steps of this project this liver-tumor-on-a-chip will be used to preclinically validate the responsive drug delivery and therapeutic functionality of the developed GbMNP@PF127@DOX nanosystem under dynamic conditions. In addition to the 3D tumor cell model developed, 3D tumor-organoids consisting of embedded co-cultures of both tumoral and healthy cells-derived spheroids are needed to better recapitulate the physiology of a human solid tumor and its surroundings. Their integration in microfluidic systems would lead to an even more representative model of the disease. It is also important to highlight that the preclinical results obtained using organ-on-a-chip *in vitro* models must be still benchmarked *in vivo* in animal models.

6. BIBLIOGRAPHY

- [1] Y.-F. Yang, F.-Y. Meng, X.-H. Li, N.-N. Wu, Y.-H. Deng, L.-Y. Wei, X.-P. Zeng, Magnetic Graphene Oxide-Fe₃O₄-PANI Nanoparticle Adsorbed Platinum Drugs as Drug Delivery Systems for Cancer Therapy, *J. Nanosci. Nanotechnol.* 19 (2019) 7517–7525. <https://doi.org/10.1166/jnn.2019.16768>.
- [2] World Health Organization, International Agency for Research on Cancer, *Int. Agency Res. Cancer.* (2020). https://gco.iarc.fr/today/online-analysis-multi-bars?v=2018&mode=cancer&mode_population=countries&population=900&populations=900&key=asr&sex=0&cancer=39&type=0&statistic=5&prevalence=0&population_group=0&ages_group%5B%5D=0&ages_group%5B%5D=17&nb_items=10& (accessed August 25, 2020).
- [3] A.E.A. Laaroussi, M. El Hia, M. Rachik, R. Ghazzali, Analysis of a Multiple Delays Model for Treatment of Cancer with Oncolytic Virotherapy, *Hindawi.* 19 (2019) 12. <https://doi.org/10.1158/1078-0432.CCR-13-1471>.
- [4] Deaths due to some causes of death in% of total deaths, *PORDATA.* (2020).
- [5] World Health Organization, *Cancer, Management, World Heal. Organ.* (2020). https://www.who.int/health-topics/cancer#tab=tab_3 (accessed September 15, 2020).
- [6] M.T. Birgani, V. Carloni, Tumor microenvironment, a paradigm in hepatocellular carcinoma progression and therapy, *Int. J. Mol. Sci.* 18 (2017) 7–10. <https://doi.org/10.3390/ijms18020405>.
- [7] T. Eggert, T.F. Greten, Tumor regulation of the tissue environment in the liver, *Pharmacol. Ther.* 173 (2017) 47–57. <https://doi.org/10.1016/j.pharmthera.2017.02.005>.
- [8] J.P. Fernández, K.A. Luddy, C. Harmon, C. O’Farrelly, Hepatic tumor microenvironments and effects on NK cell phenotype and function, *Int. J. Mol. Sci.* 20 (2019). <https://doi.org/10.3390/ijms20174131>.
- [9] A.M. Chambers, K.B. Lupo, S. Matosevic, Tumor microenvironment-induced immunometabolic reprogramming of natural killer cells, *Front. Immunol.* 9 (2018) 1–10. <https://doi.org/10.3389/fimmu.2018.02517>.
- [10] J. Delahousse, C. Skarbek, A. Paci, Prodrugs as drug delivery system in oncology, *Cancer Chemother. Pharmacol.* 84 (2019) 937–958. <https://doi.org/10.1007/s00280-019-03906-2>.
- [11] H. R. Seo, Roles of Tumor Microenvironment in Hepatocellular Carcinoma, *Curr. Cancer Ther. Rev.* 11 (2015) 82–93. <https://doi.org/10.2174/1573394711666151022203313>.
- [12] C. Xia, H. Zeng, Y. Zheng, Low-intensity ultrasound enhances the antitumor effects of doxorubicin on hepatocellular carcinoma cells through the ROS-miR-21-PTEN axis, *Mol. Med. Rep.* 21 (2019) 989–998. <https://doi.org/10.3892/mmr.2020.10936>.
- [13] K.B. Hartman, L.J. Wilson, M.G. Rosenblum, Detecting and treating cancer with nanotechnology, *Mol. Diagnosis Ther.* 12 (2008) 1–14. <https://doi.org/10.1007/BF03256264>.
- [14] R.L. Johnston, J.P. Wilcoxon, *FRONTIERS OF NANOSCIENCE Series Editor : Richard E . Palmer The Nanoscale Physics Research Laboratory , The School of Physics and Astronomy , The University of Birmingham , UK Vol . 1 Nanostructured Materials edited by Gerhard Wilde Vol . 2 Atomic and Mol, n.d.*
- [15] W. Chen, X. Wen, G. Zhen, X. Zheng, Assembly of Fe₃O₄ nanoparticles on PEG-functionalized graphene oxide for efficient magnetic imaging and drug delivery, *RSC Adv.* 5 (2015) 69307–69311. <https://doi.org/10.1039/c5ra09901c>.
- [16] G. Kandasamy, Recent advancements in manganite perovskites and spinel ferrite-based magnetic nanoparticles for biomedical theranostic applications, *Nanotechnology.* 30 (2019) 502001.

<https://doi.org/10.1088/1361-6528/ab3f17>.

- [17] D. Chang, M. Lim, J.A.C.M. Goos, R. Qiao, Y.Y. Ng, F.M. Mansfeld, M. Jackson, T.P. Davis, M. Kavallaris, Biologically targeted magnetic hyperthermia: Potential and limitations, *Front. Pharmacol.* 9 (2018). <https://doi.org/10.3389/fphar.2018.00831>.
- [18] A.K. Goyal, G. Rath, C. Faujdar, B. Malik, Application and Perspective of pH-Responsive Nano Drug Delivery Systems, Elsevier Inc., 2019. <https://doi.org/10.1016/b978-0-12-814029-1.00002-8>.
- [19] E. Kita, T. Oda, T. Kayano, S. Sato, M. Minagawa, H. Yanagihara, M. Kishimoto, C. Mitsumata, S. Hashimoto, K. Yamada, N. Ohkohchi, Ferromagnetic nanoparticles for magnetic hyperthermia and thermoablation therapy, *J. Phys. D. Appl. Phys.* 43 (2010). <https://doi.org/10.1088/0022-3727/43/47/474011>.
- [20] A. Sharma, R. Houshyar, P. Bhosale, J. Il Choi, R. Gulati, C. Lall, Chemotherapy induced liver abnormalities: an imaging perspective, *Clin. Mol. Hepatol.* 20 (2014) 317–326. <https://doi.org/10.3350/cmh.2014.20.3.317>.
- [21] E.J. Lee, H.W. Chung, J.H. Jo, Y. So, Radioembolization for the Treatment of Primary and Metastatic Liver Cancers, *Nucl. Med. Mol. Imaging* (2010). 53 (2019) 367–373. <https://doi.org/10.1007/s13139-019-00615-9>.
- [22] H. Li, L. Zhang, Liver regeneration microenvironment of hepatocellular carcinoma for prevention and therapy, *Oncotarget.* 8 (2017) 1805–1813. <https://doi.org/10.18632/oncotarget.12101>.
- [23] L. Yuan, Z. Bing, J. Han, X. An, X. Liu, R. Li, C. Wang, X. Sun, L. Yang, K. Yang, Study on the anti-tumor mechanism related to immune microenvironment of *Bombyx Batryticatus* on viral and non-viral infections of hepatocellular carcinoma, *Biomed. Pharmacother.* 124 (2020) 109838. <https://doi.org/10.1016/j.biopha.2020.109838>.
- [24] C. Hu, Z. Wu, L. Li, Pre-treatments enhance the therapeutic effects of mesenchymal stem cells in liver diseases, *J. Cell. Mol. Med.* 24 (2020) 40–49. <https://doi.org/10.1111/jcmm.14788>.
- [25] M.A. Hayat, *Methods of Cancer Diagnosis, Therapy, and Prognosis*, 2011. <https://doi.org/10.1007/978-90-481-8665-5>.
- [26] G.C. Kanel, *Pathology of liver diseases*, 2017. <https://doi.org/10.1017/CBO9781107415324.004>.
- [27] A. Albin, A. Bruno, D.M. Noonan, L. Mortara, Contribution to tumor angiogenesis from innate immune cells within the tumor microenvironment: Implications for immunotherapy, *Front. Immunol.* 9 (2018). <https://doi.org/10.3389/fimmu.2018.00527>.
- [28] J.S. Nurkovic, Mesenchymal stem cells : possibilities and limitations in the application, (2016). <https://doi.org/10.13140/RG.2.1.3129.8167>.
- [29] T.T. Chang, M. Hughes-Fulford, Monolayer and spheroid culture of human liver hepatocellular carcinoma cell line cells demonstrate distinct global gene expression patterns and functional phenotypes, *Tissue Eng. - Part A.* 15 (2009) 559–567. <https://doi.org/10.1089/ten.tea.2007.0434>.
- [30] D. Kaushik, G. Bansal, Four new degradation products of doxorubicin: An application of forced degradation study and hyphenated chromatographic techniques, *J. Pharm. Anal.* 5 (2015) 285–295. <https://doi.org/10.1016/j.jpha.2015.05.003>.
- [31] K. Nawara, P. Kryszynski, G.J. Blanchard, Photoinduced reactivity of doxorubicin: Catalysis and degradation, *J. Phys. Chem. A.* 116 (2019) 4330–4337. <https://doi.org/10.1021/jp303218r>.
- [32] K.Y. Huang, H.X. He, S. Bin He, X.P. Zhang, H.P. Peng, Z. Lin, H.H. Deng, X.H. Xia, W. Chen, Gold nanocluster-based fluorescence turn-off probe for sensing of doxorubicin by photoinduced electron transfer, *Sensors Actuators, B Chem.* 296 (2019) 126656. <https://doi.org/10.1016/j.snb.2019.126656>.
- [33] E. Tasca, J. Alba, L. Galantini, M. D’Abramo, A.M. Giuliani, A. Amadei, G. Palazzo, M. Giustini, The self-association equilibria of doxorubicin at high concentration and ionic strength characterized by fluorescence spectroscopy and molecular dynamics simulations, *Colloids Surfaces A Physicochem. Eng.*

- Asp. 577 (2019) 517–522. <https://doi.org/10.1016/j.colsurfa.2019.06.005>.
- [34] M. Mobaraki, A. Faraji, M. Zare, P. Dolati, M. Ataei, H.R. Dehghan Manshadi, Molecular mechanisms of cardiotoxicity: A review on the major side-effects of doxorubicin, *Indian J. Pharm. Sci.* 79 (2017) 335–344. <https://doi.org/10.4172/pharmaceutical-sciences.1000235>.
- [35] R. Thirumaran, G.C. Prendergast, P.B. Gilman, *Cytotoxic Chemotherapy in Clinical Treatment of Cancer*, Elsevier Inc., 2007. <https://doi.org/10.1016/B978-012372551-6/50071-7>.
- [36] S. Shah, A. Chandra, A. Kaur, N. Sabnis, A. Lacko, Z. Gryczynski, R. Fudala, I. Gryczynski, Fluorescence properties of doxorubicin in PBS buffer and PVA films, *J. Photochem. Photobiol. B Biol.* 170 (2017) 65–69. <https://doi.org/10.1016/j.jphotobiol.2017.03.024>.
- [37] C. Liu, Q. Luo, Y. Tu, G. Wang, Y. Liu, Y. Xie, Drug-carrier interaction analysis in the cell penetrating peptide-modified liposomes for doxorubicin loading, *J. Microencapsul.* 32 (2015) 745–754. <https://doi.org/10.3109/02652048.2015.1073390>.
- [38] F. dos S. Scaramel, Avaliação da inativação de cisplatina, doxorubicina e paclitaxel utilizando soluções de aseptó 75 0,5%, hipoclorito de sódio 10% e tiosulfato de sódio 10%, 2009.
- [39] S.N. Hilmer, V.C. Cogger, M. Muller, D.G. Le Couteur, The hepatic Pharmacokinetics of doxorubicin and liposomal doxorubicin, 32 (2004) 794–799.
- [40] M.W. Akram, F. Raziq, M. Fakhar-e-Alam, M.H. Aziz, K.S. Alimgeer, M. Atif, M. Amir, A. Hanif, W. Aslam Farooq, Tailoring of Au-TiO₂ nanoparticles conjugated with doxorubicin for their synergistic response and photodynamic therapy applications, *J. Photochem. Photobiol. A Chem.* 384 (2019) 112040. <https://doi.org/10.1016/j.jphotochem.2019.112040>.
- [41] Y.T. Qin, H. Peng, X.W. He, W.Y. Li, Y.K. Zhang, PH-Responsive Polymer-Stabilized ZIF-8 Nanocomposites for Fluorescence and Magnetic Resonance Dual-Modal Imaging-Guided Chemo-/Photodynamic Combinational Cancer Therapy, *ACS Appl. Mater. Interfaces.* 11 (2019) 34268–34281. <https://doi.org/10.1021/acsami.9b12641>.
- [42] G. Cavaletti, *Toxic and drug-induced neuropathies*, Elsevier Inc., 2007. <https://doi.org/10.1016/B978-012088592-3/50082-7>.
- [43] D. Agudelo, P. Bourassa, G. Bérubé, H.A. Tajmir-Riahi, Intercalation of antitumor drug doxorubicin and its analogue by DNA duplex: Structural features and biological implications, *Int. J. Biol. Macromol.* 66 (2014) 144–150. <https://doi.org/10.1016/j.ijbiomac.2014.02.028>.
- [44] L. Zhao, B. Zhang, Doxorubicin induces cardiotoxicity through upregulation of death receptors mediated apoptosis in cardiomyocytes, *Sci. Rep.* 7 (2017) 1–11. <https://doi.org/10.1038/srep44735>.
- [45] Y.W. Zhang, J. Shi, Y.J. Li, L. Wei, Cardiomyocyte death in doxorubicin-induced cardiotoxicity, *Arch. Immunol. Ther. Exp. (Warsz)*. 57 (2009) 435–445. <https://doi.org/10.1007/s00005-009-0051-8>.
- [46] H. Taymaz-Nikerel, M.E. Karabekmez, S. Eraslan, B. Kırdar, Doxorubicin induces an extensive transcriptional and metabolic rewiring in yeast cells, *Sci. Rep.* 8 (2018) 1–14. <https://doi.org/10.1038/s41598-018-31939-9>.
- [47] G.N. Hortobagyi, Anthracyclines in the treatment of cancer. An overview, *Drugs.* 54 (1997) 1–7. <https://doi.org/10.2165/00003495-199700544-00003>.
- [48] F. Yang, S.S. Teves, C.J. Kemp, T. Henikoff, Doxorubicin, DNA torsion, and chromatin dynamics, *Natl. Institutes Heal.* (2013) 84–89. <https://doi.org/10.1038/jid.2014.371>.
- [49] B. Jawad, L. Poudel, R. Podgornik, N.F. Steinmetz, W.Y. Ching, Molecular mechanism and binding free energy of doxorubicin intercalation in DNA, *Phys. Chem. Chem. Phys.* 21 (2019) 3877–3893. <https://doi.org/10.1039/c8cp06776g>.
- [50] H. Lei, X. Wang, C. Wu, Early stage intercalation of doxorubicin to DNA fragments observed in molecular dynamics binding simulations, *J. Mol. Graph. Model.* 38 (2012) 279–289. <https://doi.org/10.1016/j.jmglm.2012.05.006>.

- [51] H. Simpkins, L.F. Pearlman, L.M. Thompson, Effects of Adriamycin on Supercoiled DNA and Calf Thymus Nucleosomes Studied with Fluorescent Probes, *Cancer Res.* 44 (1984) 613–618.
- [52] N. Koleini, B.E. Nickel, A.L. Edel, R.R. Fandrich, A. Ravandi, E. Kardami, Oxidized phospholipids in Doxorubicin-induced cardiotoxicity, *Chem. Biol. Interact.* 303 (2019) 35–39. <https://doi.org/10.1016/j.cbi.2019.01.032>.
- [53] U. Kanwal, N. Irfan Bukhari, M. Ovais, N. Abass, K. Hussain, A. Raza, Advances in nano-delivery systems for doxorubicin: an updated insight, *J. Drug Target.* 26 (2018) 296–310. <https://doi.org/10.1080/1061186X.2017.1380655>.
- [54] Q. Models, H.W. Hw, A.R. Reserved, Rational Design of Iron Oxide Nanoparticles as Targeted Nanomedicines for Cancer Therapy, 2 (2011) 1–8.
- [55] Comparison nanoparticle size at nanometer scale, VMCHLab. (n.d.). <https://www.wichlab.com/nanometer-scale-comparison-nanoparticle-size-comparison-nanotechnology-chart-ruler-2/> (accessed October 10, 2020).
- [56] S. Mondal, G. Hoang, P. Manivasagan, H. Kim, J. Oh, Nanostructured hollow hydroxyapatite fabrication by carbon templating for enhanced drug delivery and biomedical applications, *Ceram. Int.* 45 (2019) 17081–17093. <https://doi.org/10.1016/j.ceramint.2019.05.260>.
- [57] S. Pieper, H. Onafuye, D. Mulac, J. Cinatl, M.N. Wass, M. Michaelis, K. Langer, Incorporation of doxorubicin in different polymer nanoparticles and their anticancer activity, *Beilstein J. Nanotechnol.* 10 (2019). <https://doi.org/10.3762/bjnano.10.201>.
- [58] M. Hashemi, J. Mohammadi, M. Omid, H.D.C. Smyth, B. Muralidharan, T.E. Milner, A. Yadegari, D. Ahmadvand, M. Shalhaf, L. Tayebi, Self-assembling of graphene oxide on carbon quantum dot loaded liposomes, *Mater. Sci. Eng. C.* 103 (2019) 109860. <https://doi.org/10.1016/j.msec.2019.109860>.
- [59] S.A. Abouelmagd, N.H.A. Ellah, B.N.A. El Hamid, Temperature and pH dual-stimuli responsive polymeric carriers for drug delivery, Elsevier Ltd., 2018. <https://doi.org/10.1016/B978-0-08-101995-5.00003-9>.
- [60] Y. Zhang, L. Han, L.L. Hu, Y.Q. Chang, R.H. He, M.L. Chen, Y. Shu, J.H. Wang, Mesoporous carbon nanoparticles capped with polyacrylic acid as drug carrier for bi-trigger continuous drug release, *J. Mater. Chem. B.* 4 (2016) 5178–5184. <https://doi.org/10.1039/c6tb00987e>.
- [61] U. Ruman, S. Fakurazi, M.J. Masarudin, M.Z. Hussein, Nanocarrier-based therapeutics and theranostics drug delivery systems for next generation of liver cancer nanodrug modalities, *Int. J. Nanomedicine.* 15 (2020) 1437–1456. <https://doi.org/10.2147/IJN.S236927>.
- [62] N.T. Thanh, *Clinical applications of magnetic nanoparticles*, 2018.
- [63] S.P. Gubin, *Magnetic nanoparticles*, 2009.
- [64] E. Jimenez-Cervantes, J. López-Barroso, A.L. Martínez-Hernández, C. Velasco-Santos, Graphene-Based Materials Functionalization with Natural Polymeric Biomolecules, *Recent Adv. Graphene Res.* (2016). <https://doi.org/10.5772/64001>.
- [65] D. Baowan, B.J. Cox, T.A. Hilder, J.M. Hill, N. Thamwattana, Modelling and mechanics of carbon-based nanostructured materials, 2017. <https://doi.org/10.1016/C2016-0-02653-0>.
- [66] Q.L. Yan, M. Gozin, F.Q. Zhao, A. Cohen, S.P. Pang, Highly energetic compositions based on functionalized carbon nanomaterials, *Nanoscale.* 8 (2016) 4799–4851. <https://doi.org/10.1039/c5nr07855e>.
- [67] Y. Zhai, Z. Zhu, S. Dong, ChemInform Abstract: Carbon-Based Nanostructures for Advanced Catalysis, *ChemInform.* 46 (2015) no-no. <https://doi.org/10.1002/chin.201544277>.
- [68] K. Rajavel, C. R. Minitha, K. S. Ranjith, R. T. Rajendra Kumar, Recent Progress on the Synthesis and Applications of Carbon Based Nanostructures, *Recent Pat. Nanotechnol.* 6 (2012) 99–104. <https://doi.org/10.2174/187221012800270199>.

- [69] R. Mmaduka Obodo, I. Ahmad, F. Ifeanyichukwu Ezema, Introductory Chapter: Graphene and Its Applications, *Graphene Its Deriv. - Synth. Appl. [Working Title]*. (2019). <https://doi.org/10.5772/intechopen.86023>.
- [70] C.J. Bullock, C. Bussy, Biocompatibility Considerations in the Design of Graphene Biomedical Materials, *Adv. Mater. Interfaces*. 6 (2019). <https://doi.org/10.1002/admi.201900229>.
- [71] S. Goenka, V. Sant, S. Sant, Graphene-based nanomaterials for drug delivery and tissue engineering, *J. Control. Release*. 173 (2014) 75–88. <https://doi.org/10.1016/j.jconrel.2013.10.017>.
- [72] J.E. Morris, K. Iniewski, Graphene, Carbon Nanotubes, and Nanostructures, *Graphene, Carbon Nanotub. Nanostructures*. (2017). <https://doi.org/10.1201/b13905>.
- [73] S. Raval, Ultrafast Pump-Probe spectroscopy of Graphene Oxide (GO) and Reduced Graphene Oxide (RGO) Shivam Raval under the guidance of Prof . Prasanta Kumar Datta, (2018). <https://doi.org/10.13140/RG.2.2.13862.57923>.
- [74] P.K. Nayak, Recent Advances in Graphene Research, 2016. <https://doi.org/10.5772/61909>.
- [75] N. Alegret, A. Criado, M. Prato, Recent advances of graphene-based hybrids with magnetic nanoparticles for biomedical applications, *Curr. Med. Chem.* (2017) 529–536. <https://doi.org/10.2174/09298673236661612161>.
- [76] W.J. Hinze, R.R.B. von Frese, A. Saad, Gravity and magnetic exploration: principles, practices and exploration, 2013.
- [77] B. Sels, M. Van De Voorde, Further Volumes of the Series “ Nanotechnology Innovation & Applications ,” 2017.
- [78] A.L. Valença, Modelo molecular para o magnetismo em ferrita de cobalto, (2016).
- [79] M. Getzlaff, Fundamentals of Magnetism, 2007. <https://doi.org/10.1017/CBO9781107415324.004>.
- [80] N. Pamme, Magnetism and microfluidics, *Lab Chip*. 6 (2006) 24–38. <https://doi.org/10.1039/b513005k>.
- [81] S. Zhang, D. Zhao, Advances in Magnetic Materials: processing, properties, and performance, 2017. <https://doi.org/10.4324/9781315371573>.
- [82] R.C. Pawar, C.S. Lee, Heterogeneous Nanocomposite-Photocatalysis for Water Purification, 2015. <https://doi.org/10.1016/C2014-0-02650-0>.
- [83] K. Chokprasombat, Synthesis of Patterned Media by Self-Assembly of FePt Nanoparticles, *Walailaki J.* 8 (2011) 87–96. <https://doi.org/10.2004/wjst.v8i2.19>.
- [84] S. Bedanta, O. Petravic, W. Kleemann, Supermagnetism, Elsevier, 2015. <https://doi.org/10.1016/B978-0-444-63528-0.00001-2>.
- [85] F.C. Fonseca, G.F. Goya, R.F. Jardim, R. Muccillo, N.L.V. Carreño, E. Longo, E.R. Leite, Superparamagnetism and magnetic properties of Ni nanoparticles embedded in SiO₂, *Phys. Rev. B - Condens. Matter Mater. Phys.* 66 (2002) 1044061–1044065. <https://doi.org/10.1103/PhysRevB.66.104406>.
- [86] P.K. Dey, Application of ferrite medium in microwave devices, ResearchGate. (2016).
- [87] U.T. Lam, R. Mammucari, N.R. Foster, Processing of iron oxide nanoparticles by supercritical fluids, *Ind. Eng. Chem. Res.* 47 (2008) 599–614. <https://doi.org/10.1021/ie070494+>.
- [88] Suriyanto, E.Y.K. Ng, S.D. Kumar, Physical mechanism and modeling of heat generation and transfer in magnetic fluid hyperthermia through Néelian and Brownian relaxation: a review, *Biomed. Eng. Online*. 16 (2017) 36. <https://doi.org/10.1186/s12938-017-0327-x>.
- [89] M. Suto, Y. Hirota, H. Mamiya, A. Fujita, R. Kasuya, K. Tohji, B. Jeyadevan, Heat dissipation mechanism of magnetite nanoparticles in magnetic fluid hyperthermia, *J. Magn. Magn. Mater.* 321 (2009) 1493–1496. <https://doi.org/10.1016/j.jmmm.2009.02.070>.

- [90] G. Cotin, F. Pertont, C. Blanco-Andujar, B. Pichon, D. Mertz, S. Bégin-Colin, Design of Anisotropic Iron-Oxide-Based Nanoparticles for Magnetic Hyperthermia, *Nanomater. Magn. Opt. Hyperth. Appl.* (2018) 41–60. <https://doi.org/10.1016/B978-0-12-813928-8.00002-8>.
- [91] A.J. GIUSTINI, A.A. PETRYK, S.M. CASSIM, J.A. TATE, I. BAKER, P.J. HOOPEs, Magnetic Nanoparticle Hyperthermia in Cancer Treatment, *Nano Life*. 01 (2010) 17–32. <https://doi.org/10.1142/s1793984410000067>.
- [92] K. Wu, D. Su, J. Liu, R. Saha, J.P. Wang, Magnetic nanoparticles in nanomedicine: A review of recent advances, *Nanotechnology*. 30 (2019) 502003. <https://doi.org/10.1088/1361-6528/ab4241>.
- [93] M.M.M. Ahmed, T. Imae, Effect of external magnetic field on cyclic voltammetry of exfoliated graphene-based magnetic composites with conductive polymer and carbon dots, *J. Magn. Magn. Mater.* 491 (2019) 165604. <https://doi.org/10.1016/j.jmmm.2019.165604>.
- [94] N.T. Thanh, *Magnetic Nanoparticles From Fabrication to Clinical Applications*, 2012. <https://doi.org/10.1002/ddr>.
- [95] M. Coduri, P. Masala, L. Del Bianco, F. Spizzo, D. Ceresoli, C. Castellano, S. Cappelli, C. Oliva, S. Checchia, M. Allieta, D.V. Szabo, S. Schlabach, M. Hagelstein, C. Ferrero, M. Scavini, Local structure and magnetism of Fe₂O₃ maghemite nanocrystals: The role of crystal dimension, *Nanomaterials*. 10 (2020). <https://doi.org/10.3390/nano10050867>.
- [96] W. Wu, Z. Wu, T. Yu, C. Jiang, W.S. Kim, Recent progress on magnetic iron oxide nanoparticles: Synthesis, surface functional strategies and biomedical applications, *Sci. Technol. Adv. Mater.* 16 (2015) 23501. <https://doi.org/10.1088/1468-6996/16/2/023501>.
- [97] X. Zhang, Y. Niu, X. Meng, Y. Li, J. Zhao, Structural evolution and characteristics of the phase transformations between α -Fe₂O₃, Fe₃O₄ and γ -Fe₂O₃ nanoparticles under reducing and oxidizing atmospheres, *CrystEngComm*. 15 (2013) 8166–8172. <https://doi.org/10.1039/c3ce41269e>.
- [98] S. Tiquia-Arashiro, D.F. Rodrigues, *Nanoparticles Synthesized by Microorganisms*, 2016. <https://doi.org/10.1007/978-3-319-45215-9>.
- [99] M.I. Dar, S.A. Shivashankar, Single crystalline magnetite, maghemite, and hematite nanoparticles with rich coercivity, *RSC Adv.* 4 (2014) 4105–4113. <https://doi.org/10.1039/c3ra45457f>.
- [100] W. Wu, Q. He, C. Jiang, Magnetic iron oxide nanoparticles: Synthesis and surface functionalization strategies, *Nanoscale Res. Lett.* 3 (2008) 397–415. <https://doi.org/10.1007/s11671-008-9174-9>.
- [101] C. Hui, C. Shen, T. Yang, L. Bao, J. Tian, H. Ding, C. Li, H.J. Gao, Large-scale Fe₃O₄ nanoparticles soluble in water synthesized by a facile method, *J. Phys. Chem. C*. 112 (2008) 11336–11339. <https://doi.org/10.1021/jp801632p>.
- [102] S. Islam, A. Khan, G.M.S. Rahman, H. Aftab, A comparative study on heat dissipation, morphological and magnetic properties of hyperthermia suitable ... Simple Hydrothermal Synthesis and Morphological Study of Magnetic Nanoparticles, 35 (2016) 1047–1053. <https://doi.org/10.1007/s12034-012-0414-3>.
- [103] A. Szpak, S. Fiejdasz, W. Prendota, T. Strączek, C. Kapusta, J. Szmyd, M. Nowakowska, S. Zapotoczny, T1–T2 Dual-modal MRI contrast agents based on superparamagnetic iron oxide nanoparticles with surface attached gadolinium complexes, *J. Nanoparticle Res.* 16 (2014) 1–11. <https://doi.org/10.1007/s11051-014-2678-6>.
- [104] A. Szpak, G. Kania, T. Skórka, W. Tokarz, S. Zapotoczny, M. Nowakowska, Stable aqueous dispersion of superparamagnetic iron oxide nanoparticles protected by charged chitosan derivatives, *J. Nanoparticle Res.* 15 (2013). <https://doi.org/10.1007/s11051-012-1372-9>.
- [105] W. Chen, P. Yi, Y. Zhang, L. Zhang, Z. Deng, Z. Zhang, Composites of aminodextran-coated Fe₃O₄ nanoparticles and graphene oxide for cellular magnetic resonance imaging, *ACS Appl. Mater. Interfaces*. 3 (2011) 4085–4091. <https://doi.org/10.1021/am2009647>.
- [106] M.M. Stylianakis, G. Viskadourous, C. Polyzoidis, G. Veisakis, G. Kenanakis, N. Kornilios, K. Petridis, E.

- Kymakis, Updating the role of reduced graphene oxide ink on field emission devices in synergy with charge transfer materials, *Nanomaterials*. 9 (2019) 1–15. <https://doi.org/10.3390/nano9020137>.
- [107] Y. Yang, A.M. Asiri, Z. Tang, D. Du, Y. Lin, Graphene based materials for biomedical applications, *Mater. Today*. 16 (2013) 365–373. <https://doi.org/10.1016/j.mattod.2013.09.004>.
- [108] C. Donga, S.B. Mishra, A.S. Abd-El-Aziz, A.K. Mishra, Advances in Graphene-Based Magnetic and Graphene-Based/TiO₂ Nanoparticles in the Removal of Heavy Metals and Organic Pollutants from Industrial Wastewater, *J. Inorg. Organomet. Polym. Mater.* (2020) 14–16. <https://doi.org/10.1007/s10904-020-01679-3>.
- [109] A.K. Gupta, R.R. Naregalkar, V.D. Vaidya, M. Gupta, Recent advances on surface engineering of magnetic iron oxide nanoparticles and their biomedical applications, *Nanomedicine*. 2 (2007) 23–39. <https://doi.org/10.2217/17435889.2.1.23>.
- [110] L. Li, W. Jiang, K. Luo, H. Song, F. Lan, Y. Wu, Z. Gu, Superparamagnetic iron oxide nanoparticles as MRI contrast agents for non-invasive stem cell labeling and tracking, *Theranostics*. 3 (2013) 595–615. <https://doi.org/10.7150/thno.5366>.
- [111] N. Lee, T. Hyeon, Designed synthesis of uniformly sized iron oxide nanoparticles for efficient magnetic resonance imaging contrast agents, *Chem. Soc. Rev.* 41 (2012) 2575–2589. <https://doi.org/10.1039/c1cs15248c>.
- [112] G.P. Yan, L. Robinson, P. Hogg, Magnetic resonance imaging contrast agents: Overview and perspectives, *Radiography*. 13 (2007). <https://doi.org/10.1016/j.radi.2006.07.005>.
- [113] X. Zhao, H. Zhao, Z. Chen, M. Lan, Ultrasmall superparamagnetic iron oxide nanoparticles for magnetic resonance imaging contrast agent, *J. Nanosci. Nanotechnol.* 14 (2014) 210–220. <https://doi.org/10.1166/jnn.2014.9192>.
- [114] M.F. Casula, P. Floris, C. Innocenti, A. Lascialfari, M. Marinone, M. Corti, R.A. Sperling, W.J. Parak, C. Sangregorio, Magnetic resonance imaging contrast agents based on iron oxide superparamagnetic ferrofluids, *Chem. Mater.* 22 (2010) 1739–1748. <https://doi.org/10.1021/cm9031557>.
- [115] A. Merbach, L. Helm, É. Tóth, *The Chemistry of Contrast Agents in Medical Magnetic Resonance Imaging: Second Edition*, 2013. <https://doi.org/10.1002/9781118503652>.
- [116] C.F.G.C. Geraldes, S. Laurent, Classification and basic properties of contrast agents for magnetic resonance imaging, *Contrast Media Mol. Imaging*. 4 (2009) 1–23. <https://doi.org/10.1002/cmml.265>.
- [117] X. Ma, A. Gong, B. Chen, J. Zheng, T. Chen, Z. Shen, A. Wu, Exploring a new SPION-based MRI contrast agent with excellent water-dispersibility, high specificity to cancer cells and strong MR imaging efficacy, *Colloids Surfaces B Biointerfaces*. 126 (2015) 44–49. <https://doi.org/10.1016/j.colsurfb.2014.11.045>.
- [118] Z.R. Stephen, F.M. Kievit, M. Zhang, Magnetite nanoparticles for medical MR imaging, *Mater. Today*. 14 (2011) 330–338. [https://doi.org/10.1016/S1369-7021\(11\)70163-8](https://doi.org/10.1016/S1369-7021(11)70163-8).
- [119] Y.-X.J. Wang, Current status of superparamagnetic iron oxide contrast agents for liver magnetic resonance imaging, *World J. Gastroenterol.* (2015). <https://doi.org/10.1007/bf02678498>.
- [120] R.O. Rodrigues, G. Baldi, S. Doumett, L. Garcia-Hervia, J. Gallo, M. Bañobre-López, G. Dražić, R.C. Calhelha, I.C.F.R. Ferreira, R. Lima, H.T. Gomes, A. Silva, Multifunctional graphene-based magnetuc nanocarriers for combined hyperthermia and dual stimuli-responsive drug delivery, *Mater. Sci. Eng. C*. (2018) 1–2.
- [121] R.O. Rodrigues, R. Lima, H.T. Gomes, A.M.T. Silva, Magnetic Carbon Nanostructures and Study of Their Transport in Microfluidic Devices for Hyperthermia, in: *XV Mediterr. Conf. Med. Biol. Eng. Comput. – MEDICON 2019*, 2019. https://doi.org/10.1007/978-3-030-31635-8_232.
- [122] Z. Behrouzki, Z. Joveini, B. Keshavarzi, N. Eyvazzadeh, R.Z. Aghdam, Hyperthermia: How can it be used?, *Oman Med. J.* 31 (2016) 89–97. <https://doi.org/10.5001/omj.2016.19>.
- [123] M. Bañobre-López, A. Teijeiro, J. Rivas, Magnetic nanoparticle-based hyperthermia for cancer

- treatment, *Reports Pract. Oncol. Radiother.* 18 (2013) 397–400.
<https://doi.org/10.1016/j.rpor.2013.09.011>.
- [124] G. Hegyi, G.P. Szigeti, A. Szász, Hyperthermia versus oncothermia: Cellular effects in complementary cancer therapy, *Evidence-Based Complement. Altern. Med.* 2013 (2013).
<https://doi.org/10.1155/2013/672873>.
- [125] A. Chicheł, J. Skowronek, M. Kubaszewska, M. Kanikowski, Hyperthermia - Description of a method and a review of clinical applications, *Reports Pract. Oncol. Radiother.* 12 (2007) 267–275.
[https://doi.org/10.1016/S1507-1367\(10\)60065-X](https://doi.org/10.1016/S1507-1367(10)60065-X).
- [126] V. Carina, V. Costa, M. Sartori, D. Bellavia, A. De Luca, L. Raimondi, M. Fini, G. Giavaresi, Adjuvant biophysical therapies in osteosarcoma, *Cancers (Basel)*. 11 (2019).
<https://doi.org/10.3390/cancers11030348>.
- [127] Magforce , The Nanomedicine Company, (n.d.). <https://www.magforce.com/home/> (accessed January 10, 2021).
- [128] A. Akbarzadeh, M. Samiei, S.W. Joo, M. Anzaby, Synthesis, characterization and in vitro studies of doxorubicin-loaded magnetic nanoparticles grafted to smart copolymers on A549 lung cancer cell line, *J. Nanobiotechnology*. (2012). <https://doi.org/10.1007/s10725-013-9801-z>.
- [129] L. Zhu, J. Ma, N. Jia, Y. Zhao, H. Shen, Chitosan-coated magnetic nanoparticles as carriers of 5-Fluorouracil: Preparation, characterization and cytotoxicity studies, *Colloids Surfaces B Biointerfaces*. 68 (2009) 1–6. <https://doi.org/10.1016/j.colsurfb.2008.07.020>.
- [130] Y. Inaoka, T. Keii, A. Mimura, K. Murase, A Novel Therapeutic Strategy Combining Use of Intracellular Magnetic Nanoparticles under an Alternating Magnetic Field and Bleomycin, *Open J. Appl. Sci.* 09 (2019) 87–103. <https://doi.org/10.4236/ojapps.2019.93008>.
- [131] M. Babincova, V. Altanero, C. Altaner, C. Bergemann, P. Babinec, In vitro analysis of cisplatin functionalized magnetic nanoparticles in combined cancer chemotherapy and electromagnetic hyperthermia, *IEEE Trans. Nanobioscience*. 7 (2008) 15–19.
<https://doi.org/10.1109/TNB.2008.2000145>.
- [132] E.C. Costa, A.F. Moreira, D. de Melo-Diogo, V.M. Gaspar, M.P. Carvalho, I.J. Correia, 3D tumor spheroids: an overview on the tools and techniques used for their analysis, *Biotechnol. Adv.* 34 (2016) 1427–1441. <https://doi.org/10.1016/j.biotechadv.2016.11.002>.
- [133] K. Duval, H. Grover, L.H. Han, Y. Mou, A.F. Pegoraro, J. Fredberg, Z. Chen, Modeling physiological events in 2D vs. 3D cell culture, *Physiology*. 32 (2017) 266–277. <https://doi.org/10.1152/physiol.00036.2016>.
- [134] A.S. Nunes, A.S. Barros, E.C. Costa, A.F. Moreira, I.J. Correia, 3D tumor spheroids as in vitro models to mimic in vivo human solid tumors resistance to therapeutic drugs, *Biotechnol. Bioeng.* 116 (2019) 206–226. <https://doi.org/10.1002/bit.26845>.
- [135] F. Sambale, A. Lavrentieva, F. Stahl, C. Blume, M. Stiesch, C. Kasper, D. Bahnemann, T. Scheper, Three dimensional spheroid cell culture for nanoparticle safety testing, *J. Biotechnol.* 205 (2015) 120–129.
<https://doi.org/10.1016/j.jbiotec.2015.01.001>.
- [136] T. Yoshida, N.A. Sopko, M. Kates, X. Liu, G. Joice, D.J. McConkey, T.J. Bivalacqua, Impact of spheroid culture on molecular and functional characteristics of bladder cancer cell lines, *Oncol. Lett.* 18 (2019) 4923–4929. <https://doi.org/10.3892/ol.2019.10786>.
- [137] M. Zanoni, M. Cortesi, A. Zamagni, C. Arienti, S. Pignatta, A. Tesei, Modeling neoplastic disease with spheroids and organoids, *J. Hematol. Oncol.* 13 (2020) 1–15. <https://doi.org/10.1186/s13045-020-00931-0>.
- [138] N.S. Bhise, V. Manoharan, S. Massa, A. Tamayol, M. Ghaderi, M. Miscuglio, Q. Lang, Y.S. Zhang, S.R. Shin, G. Calzone, N. Annabi, T.D. Shupe, C.E. Bishop, A. Atala, M.R. Dokmeci, A. Khademhosseini, A liver-on-a-chip platform with bioprinted hepatic spheroids, *Biofabrication*. 8 (2016) 14101.
<https://doi.org/10.1088/1758-5090/8/1/014101>.

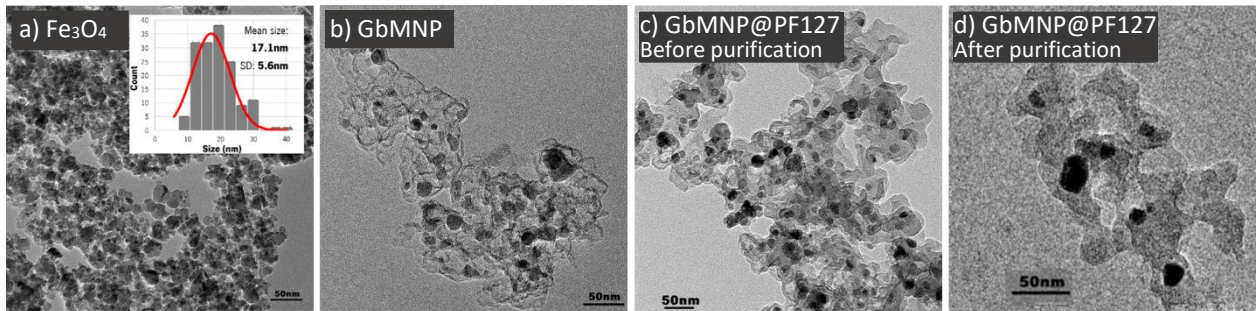
- [139] J. Lee, M.J. Cuddihy, G.M. Cater, N.A. Kotov, Engineering liver tissue spheroids with inverted colloidal crystal scaffolds, *Biomaterials*. 30 (2009) 4687–4694. <https://doi.org/10.1016/j.biomaterials.2009.05.024>.
- [140] H.R. Jung, H.M. Kang, J.W. Ryu, D.S. Kim, K.H. Noh, E.S. Kim, H.J. Lee, K.S. Chung, H.S. Cho, N.S. Kim, D.S. Im, J.H. Lim, C.R. Jung, Cell Spheroids with Enhanced Aggressiveness to Mimic Human Liver Cancer in Vitro and in Vivo, *Sci. Rep.* 7 (2017) 1–14. <https://doi.org/10.1038/s41598-017-10828-7>.
- [141] E. Elje, M. Hesler, E. Rundén-Pran, P. Mann, E. Mariussen, S. Wagner, M. Dusinska, Y. Kohl, The comet assay applied to HepG2 liver spheroids, *Mutat. Res. - Genet. Toxicol. Environ. Mutagen.* 845 (2019) 403033. <https://doi.org/10.1016/j.mrgentox.2019.03.006>.
- [142] M.P. Carvalho, E.C. Costa, S.P. Miguel, I.J. Correia, Tumor spheroid assembly on hyaluronic acid-based structures: A review, *Carbohydr. Polym.* 150 (2016) 139–148. <https://doi.org/10.1016/j.carbpol.2016.05.005>.
- [143] M.A. Lancaster, J.A. Knoblich, Organogenesis in a dish: Modeling development and disease using organoid technologies, *Science* (80-.). 345 (2014). <https://doi.org/10.1126/science.1247125>.
- [144] C. Xinaris, V. Brizi, G. Remuzzi, Organoid Models and Applications in Biomedical Research, *Nephron*. 130 (2015) 191–199. <https://doi.org/10.1159/000433566>.
- [145] G. Colella, F. Fazioli, M. Gallo, A. De Chiara, G. Apice, C. Ruosi, A. Cimmino, F. De Nigris, Sarcoma spheroids and organoids— Promising tools in the era of personalized medicine, *Int. J. Mol. Sci.* 19 (2018). <https://doi.org/10.3390/ijms19020615>.
- [146] Labiotech, How are organoids revolutionizing cancer drug development?, (n.d.). <https://www.labiotech.eu/cancer/organoids-cancer-drug-development/> (accessed November 20, 2020).
- [147] R. Rodrigues, G. Baldi, S. Doumett, J. Gallo, M. Bañobre-López, G. Dražić, R. Calhelha, I. Ferreira, R. Lima, A. Silva, H. Gomes, A Tailor-Made Protocol to Synthesize Yolk-Shell Graphene-Based Magnetic Nanoparticles for Nanomedicine, *C.* 4 (2018) 55. <https://doi.org/10.3390/c4040055>.
- [148] S.F. Khattak, S.R. Bhatia, S.C. Roberts, Pluronic F127 as a cell encapsulation material: Utilization of membrane-stabilizing agents, *Tissue Eng.* 11 (2005) 974–983. <https://doi.org/10.1089/ten.2005.11.974>.
- [149] X. Hou, R.S. Amais, B.T. Jones, G.L. Donati, Inductively coupled plasma optical emission spectrometry, *Anal. Instrum. Handbook, Third Ed.* (2016) 57–74. <https://doi.org/10.1201/9781315118024-3>.
- [150] F. Caruso, S. Mantellato, M. Palacios, R.J. Flatt, ICP-OES method for the characterization of cement pore solutions and their modification by polycarboxylate-based superplasticizers, *Cem. Concr. Res.* 91 (2017) 52–60. <https://doi.org/10.1016/j.cemconres.2016.10.007>.
- [151] S. Alavi, T. Khayamian, J. Mostaghimi, Conical Torch: The Next-Generation Inductively Coupled Plasma Source for Spectrochemical Analysis, *Anal. Chem.* 90 (2018) 3036–3044. <https://doi.org/10.1021/acs.analchem.7b04356>.
- [152] J. Stetefeld, S.A. McKenna, T.R. Patel, Dynamic light scattering: a practical guide and applications in biomedical sciences, *Biophys. Rev.* 8 (2016) 409–427. <https://doi.org/10.1007/s12551-016-0218-6>.
- [153] R. Pecora, Dynamic light scattering measurement of nanometer particles in liquids, *J. Nanoparticle Res.* 2 (2000) 123–131. <https://doi.org/10.1023/A:1010067107182>.
- [154] S.S. Leong, W.M. Ng, J.K. Lim, S.P. Yeap, Dynamic light scattering: Effective sizing technique for characterization of magnetic nanoparticles, 2018. https://doi.org/10.1007/978-3-319-92955-2_3.
- [155] U. Nobbmann, M. Connah, B. Fish, P. Varley, C. Gee, S. Mulet, J. Chen, L. Zhou, Y. Lu, F. Sheng, J. Yi, S.E. Harding, Dynamic light scattering as a relative tool for assessing the molecular integrity and stability of monoclonal antibodies, *Biotechnol. Genet. Eng. Rev.* 24 (2007) 117–128. <https://doi.org/10.1080/02648725.2007.10648095>.
- [156] L. Jitkang, Y.S. Pin, C.H. Xin, L.S. Chun, Characterization of magnetic nanoparticle by dynamic light

- scattering, *Nanoscale Res. Lett.* 8 (2013) 308–381.
- [157] B. Sitharaman, *Nanobiomaterials handbook*, 2011.
- [158] R. Xu, Light scattering: A review of particle characterization applications, *Particuology*. 18 (2015) 11–21. <https://doi.org/10.1016/j.partic.2014.05.002>.
- [159] A.J. Shnoudeh, I. Hamad, R.W. Abdo, L. Qadumii, A.Y. Jaber, H.S. Surchi, S.Z. Alkelany, *Synthesis, Characterization, and Applications of Metal Nanoparticles*, Elsevier Inc., 2019. <https://doi.org/10.1016/B978-0-12-814427-5.00015-9>.
- [160] M.R. Shah, M. Imran, S. Ullah, *Nanostructured lipid carriers*, 2017. <https://doi.org/10.1016/b978-0-323-52729-3.00002-0>.
- [161] V.L. Gaikwad, P.B. Choudhari, N.M. Bhatia, M.S. Bhatia, *Characterization of pharmaceutical nanocarriers: In vitro and in vivo studies*, Elsevier Inc., 2019. <https://doi.org/10.1016/B978-0-12-816505-8.00016-3>.
- [162] R.J. Watters, M. Kester, M.A. Tran, T.P. Loughran, X. Liu, *Development and use of ceramide nanoliposomes in cancer*, 1st ed., Elsevier Inc., 2012. <https://doi.org/10.1016/B978-0-12-391860-4.00005-7>.
- [163] V. Selvamani, *Stability Studies on Nanomaterials Used in Drugs*, Elsevier Inc., 2019. <https://doi.org/10.1016/B978-0-12-814031-4.00015-5>.
- [164] K. Pate, P. Safier, *Chemical metrology methods for CMP quality*, *Adv. Chem. Mech. Planarization*. (2016) 1–325. <https://doi.org/10.1016/B978-0-08-100165-3.00012-7>.
- [165] G. V. Lowry, R.J. Hill, S. Harper, A.F. Rawle, C.O. Hendren, F. Klaessig, U. Nobbmann, P. Sayre, J. Rumble, *Guidance to improve the scientific value of zeta-potential measurements in nanoEHS*, *Environ. Sci. Nano*. 3 (2016) 953–965. <https://doi.org/10.1039/c6en00136j>.
- [166] A.E. Deatsch, B.A. Evans, *Heating efficiency in magnetic nanoparticle hyperthermia*, *J. Magn. Magn. Mater.* 354 (2014) 163–172. <https://doi.org/10.1016/j.jmmm.2013.11.006>.
- [167] M.M. Cruz, L.P. Ferreira, A.F. Alves, S.G. Mendo, P. Ferreira, M. Godinho, M.D. Carvalho, *Nanoparticles for Magnetic Hyperthermia Chapter Outline*, Elsevier Inc., 2017. <https://doi.org/10.1016/B978-0-323-46144-3/00019-2>.
- [168] H. Haynes, W.M. Holmes, *The emerging use of Magnetic Resonance Imaging (MRI) for 3D analysis of sediment structures and internal flow processes*, *Geomorphol. Tech.* (2013) 1–10.
- [169] M. Thammana, *A review on high performance liquid chromatography*, *Int. J. Pharm. Res.* 5 (2016) 1–6. <https://doi.org/10.22214/ijraset.2018.2098>.
- [170] W.R. LaCourse, *Column liquid chromatography: Equipment and instrumentation*, *Anal. Chem.* 74 (2002) 2813–2831. <https://doi.org/10.1021/ac020220q>.
- [171] V.R. Meyer, *Practical high-performance liquid chromatography: Fourth edition*, 2004. <https://doi.org/10.1002/0470032677>.
- [172] O. Scherf-clavel, *Impurity Profiling of Challenging Active Pharmaceutical Ingredients without Impurity Profiling of Challenging Active Pharmaceutical Ingredients without Chromophore zur Erlangung des der Julius-Maximilians-Universität Würzburg Oliver Wahl*, (2016) 194.
- [173] W. Zhang, J. Wang, Z. Mi, J. Su, X. You, G. Keceli, Y. Wang, R. Cao, H.C. Lai, *Extraction and Analysis of Tetrahydrocannabinol, A Cannabis Compound in Oral Fluid*, *Int. J. Biol.* 9 (2016) 30. <https://doi.org/10.5539/ijb.v9n1p30>.
- [174] L. Serra, J. Doménech, N.A. Peppas, *Drug transport mechanisms and release kinetics from molecularly designed poly(acrylic acid-g-ethylene glycol) hydrogels*, *Biomaterials*. 27 (2006) 5440–5451. <https://doi.org/10.1016/j.biomaterials.2006.06.011>.

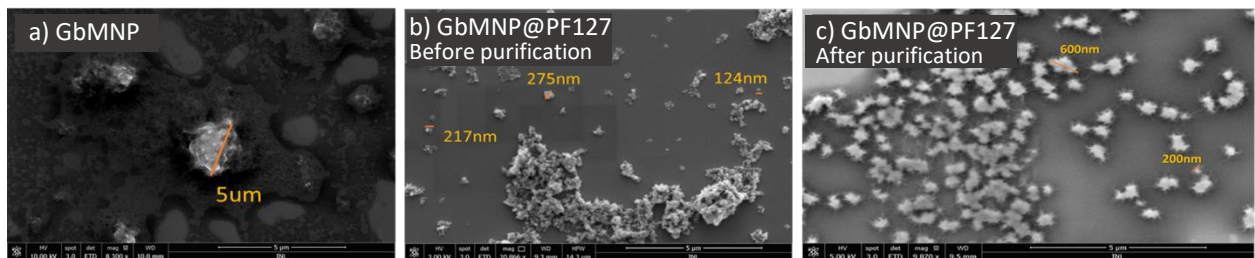
- [175] Mathematical models of drug release, *Strateg. to Modify Drug Release from Pharm. Syst.* (2015) 63–86. <https://doi.org/10.1016/b978-0-08-100092-2.00005-9>.
- [176] S. Dash, P.N. Murthy, L. Nath, P. Chowdhury, Kinetic modeling on drug release from controlled drug delivery systems, *Acta Pol. Pharm. - Drug Res.* 67 (2010) 217–223.
- [177] A.Fi. Machado, *Desenvolvimento de sistemas de liberação de fármacos baseados em nanoestruturas para o tratamento do cancro .*, 2013.
- [178] M.P. Paarakh, P.A.N.I. Jose, C.M. Setty, G. V Peter, Release Kinetics – Concepts and Applications, *Int. J. Pharm. Res. Technol.* 8 (2019) 12–20. <https://doi.org/10.31838/ijprt/08.01.02>.
- [179] I. Permanadewi, A.C. Kumoro, D.H. Wardhani, N. Aryanti, Modelling of controlled drug release in gastrointestinal tract simulation, *J. Phys. Conf. Ser.* 1295 (2019). <https://doi.org/10.1088/1742-6596/1295/1/012063>.
- [180] H. Wang, P.K. Chu, *Surface Characterization of Biomaterials*, Elsevier, 2013. <https://doi.org/10.1016/B978-0-12-415800-9.00004-8>.
- [181] D.T. Grubb, *Optical Microscopy*, Elsevier B.V., 2012. <https://doi.org/10.1016/B978-0-444-53349-4.00035-2>.
- [182] A. Nwaneshiudu, C. Kuschal, F.H. Sakamoto, R. Rox Anderson, K. Schwarzenberger, R.C. Young, Introduction to confocal microscopy, *J. Invest. Dermatol.* 132 (2012) 1–5. <https://doi.org/10.1038/jid.2012.429>.
- [183] J.B. Pawley, *Handbook of Biological Confocal Microscopy*, 2010.
- [184] ThermoFisher, Overview of ELISA, (n.d.). <https://www.thermofisher.com/pt/en/home/life-science/protein-biology/protein-biology-learning-center/protein-biology-resource-library/pierce-protein-methods/overview-elisa.html> (accessed December 10, 2020).
- [185] K.M. Slagle, S.J. Ghosn, *Tools for Sensitive , Specific , and Accurate Test Results*, 27 (2018).
- [186] abcam, Human Albumin ELISA Kit (ab179887), (n.d.). <https://www.abcam.com/human-albumin-elisa-kit-ab179887.html> (accessed December 10, 2020).
- [187] Abcam, Human Transferrin ELISA Kit (ab187391), (n.d.). <https://www.abcam.com/human-transferrin-elisa-kit-ab187391.html> (accessed December 10, 2020).
- [188] AquaBluer, MultiTarget. (n.d.). <https://multitargetpharm.com/i/aquabluer> (accessed November 25, 2020).
- [189] MoBiTec, AquaBluer Kit AquaBluer Kit Product Information Sheet, (2015) 1–3.
- [190] ThermoFisher, Calcein, AM, cell-permeant dye, (n.d.).
- [191] abcam, Propidium Iodide, (n.d.). https://www.abcam.com/propidium-iodide-ab14083.html?gclid=aw.ds%7Caw.ds&gclid=Cj0KCQiA0fr_BRDaARIsAABw4EtD48-8s8Wz8TDXqjxeKtHgTN7WbPmUDyhmN-kxrDF4cz4mlhxvwt8aAh8xEALw_wcB (accessed January 12, 2021).
- [192] invitrogen, CyQUANT LDH Cytotoxicity Assay Kit, (n.d.). https://assets.thermofisher.com/TFS-Assets/LSG/manuals/MAN0018500_CyQUANT-LDH-Cytotoxicity-Assay-Kit_PI.pdf (accessed December 5, 2020).
- [193] M. Bañobre-López, C. Bran, C. Rodríguez-Abreu, J. Gallo, M. Vázquez, J. Rivas, A colloidal stable water dispersion of Ni nanowires as an efficient: T 2-MRI contrast agent, *J. Mater. Chem. B.* 5 (2017) 3338–3347. <https://doi.org/10.1039/c7tb00574a>.
- [194] E. Blanco, H. Shen, M. Ferrari, Principles of nanoparticle design for overcoming biological barriers to drug delivery, *Nat. Biotechnol.* 33 (2015) 941–951. <https://doi.org/10.1038/nbt.3330>.
- [195] Z. Liu, J. Liu, T. Wang, Q. Li, P.S. Francis, C.J. Barrow, W. Duan, W. Yang, Switching off the interactions

- between graphene oxide and doxorubicin using Vitamin C: Combining simplicity and efficiency in drug delivery, *J. Mater. Chem. B.* 6 (2018) 1251–1259. <https://doi.org/10.1039/c7tb03063k>.
- [196] H. Vovusha, D. Banerjee, M.K. Yadav, F. Perrozzi, L. Ottaviano, S. Sanyal, B. Sanyal, Binding Characteristics of Anticancer Drug Doxorubicin with Two-Dimensional Graphene and Graphene Oxide: Insights from Density Functional Theory Calculations and Fluorescence Spectroscopy, *J. Phys. Chem. C.* 122 (2018) 21031–21038. <https://doi.org/10.1021/acs.jpcc.8b04496>.
- [197] X. Yang, X. Zhang, Z. Liu, Y. Ma, Y. Huang, Y. Chen, High-efficiency loading and controlled release of doxorubicin hydrochloride on graphene oxide, *J. Phys. Chem. C.* 112 (2008) 17554–17558. <https://doi.org/10.1021/jp806751k>.
- [198] G. Lalwani, J.L. Sundararaj, K. Schaefer, T. Button, B. Sitharaman, Synthesis, characterization, in vitro phantom imaging, and cytotoxicity of a novel graphene-based multimodal magnetic resonance imaging-X-ray computed tomography contrast agent, *J. Mater. Chem. B.* 2 (2014) 3519–3530. <https://doi.org/10.1039/c4tb00326h>.
- [199] N. Nasirzadeh, M.R. Azari, Y. Rasoulzadeh, Y. Mohammadian, An assessment of the cytotoxic effects of graphene nanoparticles on the epithelial cells of the human lung, *Toxicol. Ind. Health.* 35 (2019) 79–87. <https://doi.org/10.1177/0748233718817180>.
- [200] H. Bin Na, I.C. Song, T. Hyeon, Inorganic nanoparticles for MRI contrast agents, *Adv. Mater.* 21 (2009) 2133–2148. <https://doi.org/10.1002/adma.200802366>.
- [201] G.K. Das, N.J.J. Johnson, J. Cramen, B. Blasiak, P. Latta, B. Tomanek, F.C.J.M. Van Veggel, NaDyF 4 nanoparticles as T 2 contrast agents for ultrahigh field magnetic resonance imaging, *J. Phys. Chem. Lett.* 3 (2012) 524–529. <https://doi.org/10.1021/jz201664h>.
- [202] D.J. Korchinski, M. Taha, R. Yang, N. Nathoo, J.F. Dunn, Iron Oxide as an Mri Contrast Agent for Cell Tracking: Supplementary Issue, *Magn. Reson. Insights.* 8s1 (2015) MRI.S23557. <https://doi.org/10.4137/mri.s23557>.
- [203] S. Messner, I. Agarkova, W. Moritz, J.M. Kelm, Multi-cell type human liver microtissues for hepatotoxicity testing, *Arch. Toxicol.* 87 (2013) 209–213. <https://doi.org/10.1007/s00204-012-0968-2>.

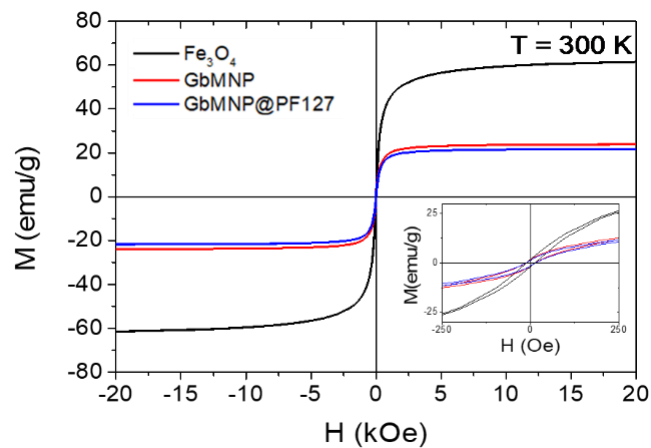
ANNEX 1 - PHYSICO-CHEMICAL CHARACTERIZATION OF GbMNPs



A1: TEM image of (a) Fe₃O₄ and associated particle size histogram with the normal distribution curve, (b) GbMNP, (c) GbMNP@PF127 before purification and (d) after purification.



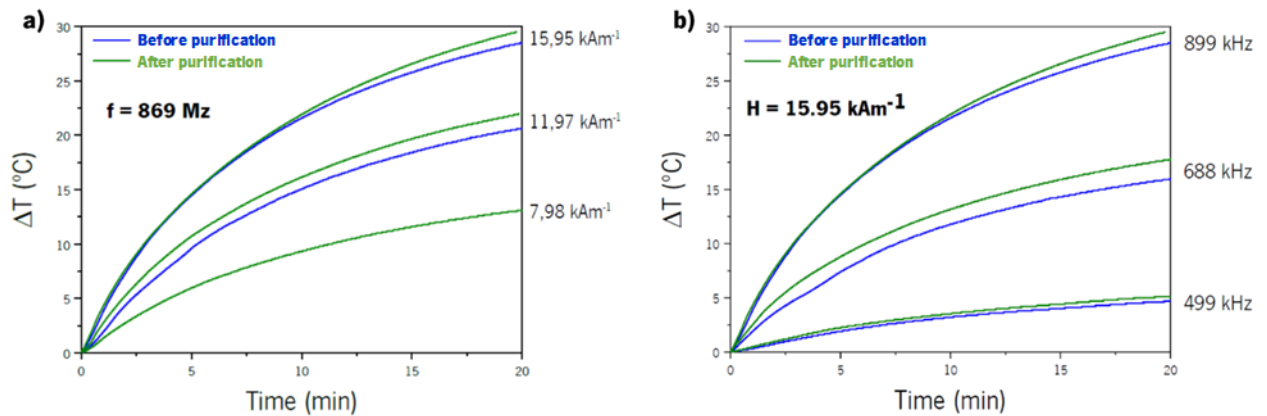
A2: SEM image of (a) GbMNP, (b) GbMNP@PF127 before purification and (c) after purification.



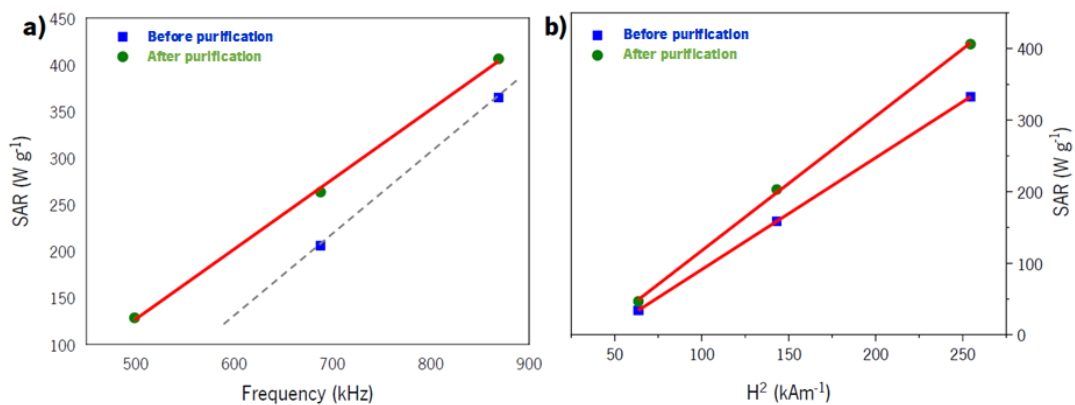
A3: Hysteresis loops with an inset of the low magnetic field area. Inset shows a magnification of the low field region.

	Fe_3O_4	GbMNP	GbMNP@PF127 <i>before purification</i>	GbMNP@PF127 <i>after purification</i>
Saturation magnetization (emu/g)	61.5	23.8	21.7	21.3
Coercivity (Oe)	12.6	13.2	12.97	12.8
Remanence (emu/g)	1.8	1.4	1.3	1.3

A4: Magnetic properties of Fe_3O_4 , GbMNP, GbMNP@PF127 before and after centrifugation;



A5: Magnetic heating (T vs. t) for water colloidal dispersions of GbMNP@PF127 before and after purification: (a) under alternating magnetic field of $f = 869 \text{ kHz}$ and increasing values of field intensity; (b) under an alternating magnetic field of 15.95 kAm^{-1} intensity and increasing values of field frequency



A6: SAR values obtained for the GbMNP@PF127 before and after purification as a function of (a) the frequency (at fixed $H = 15.95 \text{ kAm}^{-1}$) and (b) H^2 (at fixed $f = 866 \text{ kHz}$).